A CFD Investigation of Synthetic Jets

Iain MacPherson

Thesis Submitted to the Faculty of Engineering,
University of Glasgow, for the Degree of Doctor of Philosophy

University of Glasgow
Department of Aerospace Engineering

January 2003

Abstract

On current helicopter designs, the rotor blades are commonly articulated at their root. This system is employed to ensure that the resultant force of the rotor disc acts through its hub, preventing a rolling moment from being produced in forward flight. The movement which the blades are allowed however, restricts control of the blade angle of attack and allows potential lifting capability to be lost. To address this problem, on-blade flow control using synthetic jets is suggested.

Miniature synthetic jets show promise for the alleviation of a number of flow control problems. These may be especially suitable for helicopter application since proposed actuator designs are remotely activated and do not require a secondary jet fluid. These features mean that actuators may be located at large spanwise distances from the rotor hub.

An investigation of the operation of synthetic jets and their ability to effect flow control is begun with a CFD study of a single synthetic jet actuator issuing into an otherwise still atmosphere. A jet flow is developed from a rapidly deforming cavity. Velocity profiles are compared with previously published data.

Simulations are next extended to crossflow conditions. An alternative synthetic jet model is developed to improve computational efficiency. For this, the deforming cavity is removed and the flow to and from the actuator is simulated by means of an imposed sinusoidally varying velocity. Both approaches for the production of a synthetic jet flow are compared and the same essential features are found. Depending on conditions, different flow behaviours are observed. The actuator produces vortices on its blowing schedule which are either convected with the freestream, or become part of a recirculating system which becomes permanently established a short distance downstream of the actuator exit. When varying freestream and jet

operating conditions, optimal mean reduction of surface pressures is found to coincide with the first occurence of the latter flow behaviour. Using the simpler actuator model, a parameter study is performed to determine optimum jet operation across a range of conditions.

The operation of a single synthetic jet on an aerofoil section is finally considered. The same flow behaviours are once again produced. On the aerofoil, the large velocity variation means that achieving the maximum pressure reduction requires operation at high values of reduced frequency. A single actuator makes only a small difference to the overall lift, but the improvement is encouraging and suggests that a number of actuators may make a more significant difference.

Notation

b	jet half width,
c	aerofoil chord length,
f	frequency,
h	actuator exit width,
k	reduced frequency (e.g. $k_h = \omega h/2U_\infty$),
$\dot{m}$	mass flow rate,
$p^\star$	non-dimensional freestream pressure ($\frac{1}{\gamma M_\infty^2}$),
q, r, s	cavity dimensions (defined in figure 2.2),
t, Δt	time, time step,
u, v	(x,y) velocity components,
x, y	cartesian coordinates,
$\acute{x}$, $\acute{y}$	coordinates on a transformed axes system,
y_d	cavity floor position,
A	peak cavity floor deflection,
C_l, C_d, C_m	lift drag and pitching moment coefficients,
C_p	pressure coefficient,
C_μ	jet momentum coefficient,
I, I_0	sound intensity, $I_0 = 10^{-12}\ W/m^2$),
L_0	*slug* length,
M_∞	Mach Number,
R	blade length,
Re	Reynolds Number (e.g. $Re_h = \rho U_\infty h/\mu$),
SPL	Sound Pressure Level,
T, Δt	cyclic period, interval of the cyclic period

U_0	velocity at the exit plane,
U_∞,Uinf	freestream velocity,
V_0	peak blowing velocity,
V cl	centreline velocity,
Vmean	time averaged velocity,
$\mathcal{V}$	volume,

α	angle of attack,
β	inclination of the exit plane to the freestream,
γ	ratio of specific heats,
δ	boundary layer thickness,
ξ, η	streamwise and crosstream directions,
θ	phase angle,
μ	viscosity,
ρ	density,
ψ	azimuthal angle,
Ω, ω	angular frequency,
$\triangle_{IJ}$	spacing between grid points
*	superscript, denotes non-dimensional value

subscripts

exit	at the actuator exit plane,
crit	critical defining value,
jet	jet flow value,
foil	relating to an aerofoil,
∞	freestream value,
max	maximum value,
mean	average value,
0	peak magnitude,

Acknowledgements

I am extremely grateful for the support and encouragement of my supervisor Dr. Ken Badcock. Thanks also to Dr. Eric Gillies for his close supervision, to Dr. George Barakos for many useful suggestions, and to Professor Roddy Galbraith and Dr. Frank Coton for their help in the initial stages.

The contributions of Westland Helicopters and the Engineering and Physical Sciences Research Council, and the help and friendship of a great many others at the University of Glasgow are also sincerely appreciated.

Most importantly, I thank my family and my girlfriend, Amy, who are always there for me.

Contents

List of Figures

Chapter 1

Introduction

1.1 Introduction

In terms of popularity, the single-rotor with tail rotor design attributed to Sikorsky[1] is the most successful helicopter. Despite leaps in technology, essential elements of this have endured. The yaw reaction of the fuselage against the torque applied to rotate the blades is countered by a tail rotor. Neutral roll moment is achieved by another simple yet ingenious mechanism, the articulation of the rotor blades at the rotor hub. The lift which each rotor blade section contributes, depends on its angle of attack and the local flow velocity. For a helicopter in forward flight, the relative flow velocity at any section on the retreating blade decreases (figure 1.1) with any increase in forward speed. To compensate for the reduced velocity, a flapping hinge allows the effective angle of attack, and therefore the sectional lift, to self-adjust throughout the rotation. This crucially ensures that the resultant of lift acts through the rotor hub. On some recent 'hingeless' designs, the stiffness properties of the blade give the flexibility otherwise provided by a mechanical hinge, however despite the complexity of the modern rotor hub, hingeless or not, the system still operates in essentially the same way as was originally conceived by autogyro pioneer Juan de la Cierva.

Whilst the requirement for blade flapping is firmly established, the freedom of movement which the blades are thereby allowed, limits the control which the pilot can exert. The conventional cyclic pitch mechanism allows blade pitch variation between

a maximum and minimum separated by 180 degrees, only once-per-revolution. Since the thrust developed depends on all of the blades and their collective performance throughout the entire rotation, the inability to optimise performance between these extremes means that full potential is not realised. Suggested approaches which may improve the rotor disc performance are,

1. individually controlling each blade's angle of attack, hence its lifting capability. This might be done on a continuous basis or at some higher harmonic of the blade rotation.

2. adjusting blade lift independent of the angle of attack.

This work focusses on the latter approach. It aims to demonstrate improvement in the lift of a NACA-0012 aerofoil, which is a 2 dimensional (2-D) representation of a helicopter rotor blade.

1.2 Dynamic Stall and its Control

For a helicopter in forward flight, the relative flow velocity at any section on the retreating blade decreases with any increase in forward speed (figure 1.1) . In order to compensate for the associated loss of lift and so maintain a neutral roll moment, the retreating blade must consequently operate to an increased angle of attack. Sectional lift reaches a limit at stall, and the ability to continue increasing lift on the retreating side of the rotor disc is limited as significant parts of each blade become stalled. The inherent coupling of lift and thrust provision for a helicopter forces a compromise between carrying capacity and maximum attainable speed. Blade stalling places a limit on both.

At pitch rates experienced on helicopter rotors, the dynamic condition allows pitching blades to remain unstalled considerably beyond the static stall angle. However, once this angle is exceeded, eventual *dynamic stall* of lift and/or moment cannot be avoided. McCroskey[2] describes two dynamic stall regimes referred to as light stall and deep stall (figure 1.2) . Hysteresis of flow separation and reattachment is common to both, but the stalling mechanism is in each case different. For light stall,

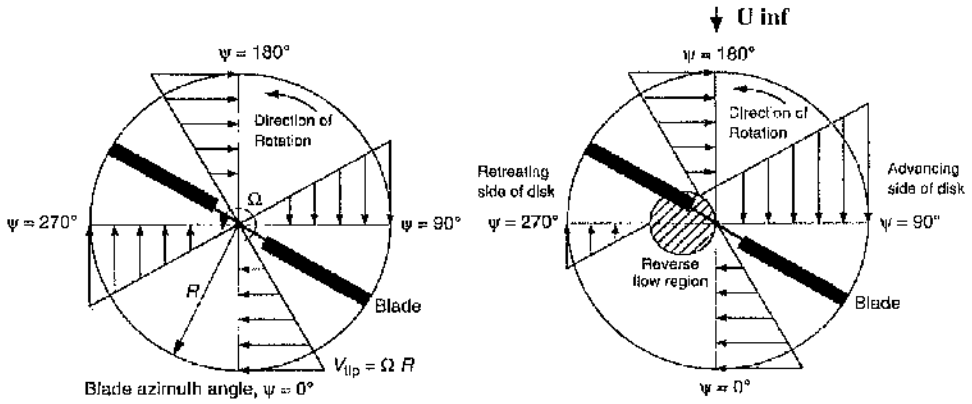

Figure 1.1: **Azimuthal Dependence of Relative Velocity**, left: Rotor Disc in Hovering Flight, The flow velocity is constant relative to the rotating blades **right:** Rotor Disc in Forward Flight. With increases in forward speed, Uinf, the relative velocity is increased on the advancing side of the blade and decreased on the retreating side. On the retreating side, this may cause a region of reversed flow.

a separation bubble forms on the blade upper surface, which on bursting causes moment stall, i.e. an abrupt change in the moment coefficient C_M. There is no stalling in terms of lift or drag however, and throughout the pitching cycle both C_L and C_D increase with angle of attack. Deep dynamic stall occurs when the pitch up motion causes the formation of a strong vortex at the blade leading edge. The presence of this *dynamic stall vortex* greatly influences the surface pressure distribution, producing a region of localised suction. Its subsequent motion across the upper surface causes considerable variation of pitching moment, C_M. Magnitudes of C_L and C_D are also much larger but only for as long as the dynamic stall vortex remains above the blade. When this passes from the trailing edge, the loss of lift is abrupt and severe.

Since the blade is only ever intermittently stalled, the condition produces a vibration which increases as a larger part of the blade is affected through a greater portion of its rotation. Large vibratory loads ultimately will make the aircraft difficult to control and may considerably reduce the fatigue life of blade and hub components. There is a large amount of literature on dynamic stall. Experiments have attempted to understand the process by which the dynamic stall vortex forms and the param-

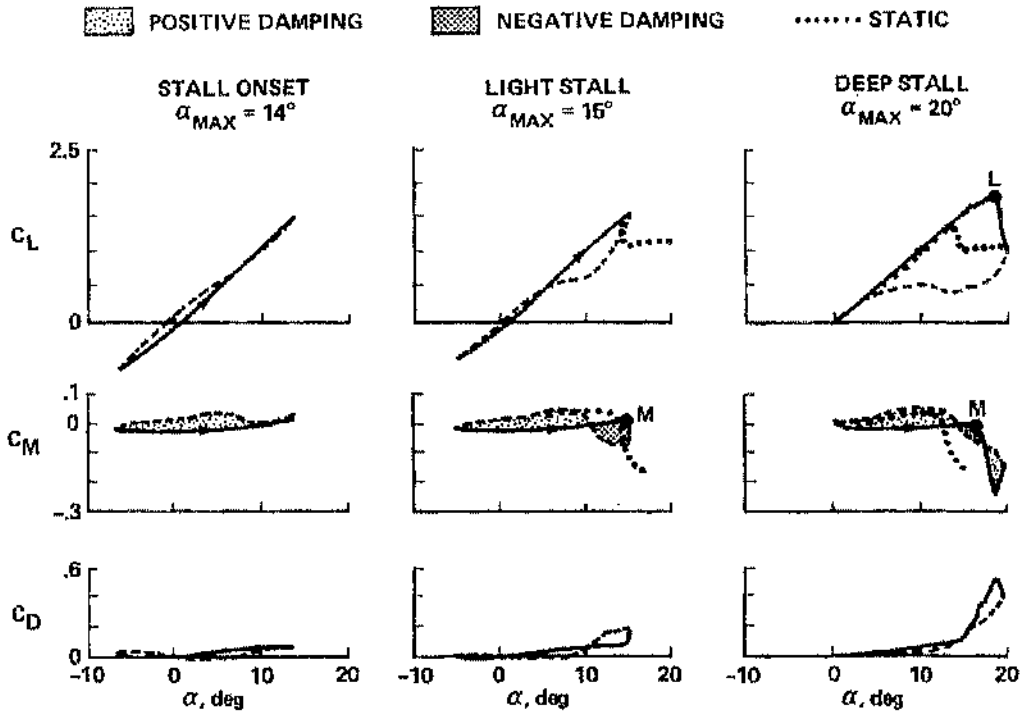

Figure 1.2: **Dynamic Stall Regimes**, from McCroskey[2]; The light dynamic stall case is particularly affected by negative damping, which is quantified by the area inside the clockwise hysteresis loops.

eters which are most significant. Examples are references [3],[4],[5],[6], [7][8][9]and [10]. Analytical and semi-empirical models[11, 12, 13, 14, 15, 16] have used this understanding to predict the rotor loads (Beddoes reviews pre-1980 calculation methods in reference [17]). More recently the phenomena has been modelled using CFD. Examples are references [18],[19],[20],[21] and [9]. Guil et al.[22] provides a still longer list of previous calculations.

Another adverse effect of the dynamic stall process is that hysteresis of the loads, as shown in figure 1.2, produces negative aerodynamic damping, i.e. over the affected part of the pitching cycle, the pitching moment acts in the same sense as the rotation. Under some conditions this can lead to self-sustaining motion described as *stall flutter*. This is an aeroselastic condition, which unlike *classical* flutter, has only a torsional mode. Of most concern is that the aerodynamically induced moment oscillations cause significantly increased torsional loading at the blade root. Stall flutter is discussed by Ham[23, 24] and by Carta[25]. Tarzanin[26] provides a semi-empirical prediction method.

1.3 Flow Control Approaches

To delay the onset of retreating blade stall is clearly desirable. Were this objective to be pursued without regard for any other, the solution would be simply to employ thicker, cambered blade sections. The design of rotor blades however, is a compromise since the blade must perform through a range of incidence, and in flow conditions which vary throughout the rotation. For cambered (non-symmetric) blades, movement of the centre of pressure as the angle of attack is adjusted, causes undesirable oscillatory pitching moments. Thicker sections may promote locally supersonic flow whilst the blade is advancing, leading to drag divergence and a surface pressure distribution dependent on the location of shock waves. The flight envelope is equally dependent on the contribution of the advancing blade and these factors must be measured against performance benefits.

Extensive research in blade design has been responsible for large improvements in performance and efficiency, for example Wilby reviews the development of the BERP rotor tip in reference [27]. However, the field is highly developed and is now an area

of diminishing returns. For further advances, clearly some alternative method of flow control is required.

1.3.1 Passive Control

A number of passive control methods have been explored to treat the problems of stall. Some of these have found their way into production, for example vortex generators are a common feature of fixed wing aircraft. Generally such methods intend re-energising the boundary layer by inducing transition to turbulence or by creating vortical structures to bring faster moving fluid closer to the wall surfaces thereby alleviating the fluid tendency to separate when confronted with an adverse pressure gradient.

Passive flow control is typically optimised for a particular condition. For helicopters, even when the aircraft flight condition is *steady*, the local blade environment may vary considerably through the rotation (figure 1.1). Whilst a particular method may be developed to benefit the retreating blade, invariably its effect will then be detrimental to advancing blade performance.

1.3.2 Active Control

To delay stall without compromising performance over the unaffected remainder of the rotation, some means of active control is sought. The immediate questions are where and how this should be applied.

Higher Harmonic Control

For current designs at extreme forward speeds, much of the lift is already being created over the fore and aftmost regions of the disc[1]. The limit of local blade contribution as the stalled condition is approached on the retreating blade, could in theory be compensated for in other regions of the disc. As previously mentioned, in the conventional rotor head system, the pilot does not have independent control over the instantaneous blade angle of attack. The cyclic pitch mechanism allows blade pitch variation between a maximum and minimum (separated by 180 deg.) only once-per-revolution. Since conventionally, the angle of attack is not optimised

between these limits, redistributing the loads via so-called Higher Harmonic Control (HHC) suggests the possibility of developing currently unharnessed lifting potential. Nguyen[28] and Nguyen and Chopra[29] used a finite element method to represent the blade structure together with an analytic model for airloads and calculated the response of the airloads to higher harmonic inputs. When control was applied to suppress vibration it was found in some circumstances that the stalled region became enlarged. An automatic stall suppression system did not necessarily improve general rotor performance.

One method of applying HHC is to have hydraulic actuators substituted in place of the conventional pitch links. This has been described as individual blade control (IBC). Yu et al.[30] in a recent review of this approach cite several successful experiments. Mostly their interest was in vibration and blade vortex interaction (BVI) noise reduction, however in one 1993/94 test program performance improvements are reported at high speed forward flight conditions. Demonstrating a need for further control development, in some other cases Yu et al. say control loads were actually increased.

A drawback of IBC method described, is that the arrangement is only able to deliver full blade feathering from the blade root. Several on-blade methods have also been considered for flow control, these include shape adjusting aerofoils, mechanical trailing edge flaps, various circulation control and jet flap devices, and synthetic jet actuators, each of which will now be discussed in turn.

Dynamic Shape Deformation

An ideal rotor would deliver high lift at low speed without detriment in transonic conditions. Such conflicting requirements might be met with a 3-D continually deforming blade, and with sensors and control algorithms sufficient to its operation throughout a range of flight conditions. The tip region is where most lift is generated and where locally supersonic flow is first encountered. If, more realistically, control is to be limited to only a part of each blade, then this is where it is likely to be most effective.

Chandrasekhara et al.[31, 32] performed experiments with an 'adaptive airfoil'. A

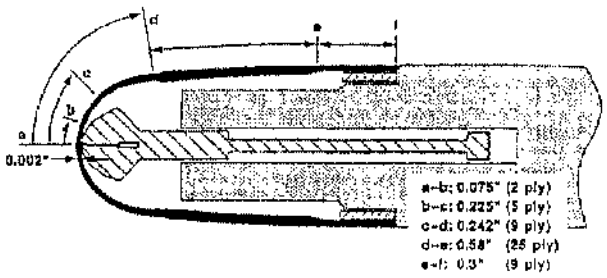

Figure 1.3: ***Dynamically Deforming Leading Edge*** Aerofoil[31]

wing having a deformable carbon fibre leading edge was used (figure 1.3). With some small deformation from an initial NACA 0012 profile[31], the stalling angle of attack was increased from 14° to 18°. Yu et al.[33] used a computational method to investigate a number of novel concepts for the control of dynamic stall, and found that lift hysteresis could be reduced with a deforming leading edge. In earlier wind tunnel experiments, Liiva and Davenport[3] studied the stall of various aerofoils, correlating the stall character with profile shape. A leading edge 'glove' (fairing) was used to alter the shape of a dynamically pitching wing. The results were less encouraging, peak C_N being reduced without altering the character of the stall.

There are some practical difficulties regarding the implementation of these methods on a real helicopter. Whilst the leading edge must be plyable enough to deform under a small control load it must also be rigid to possible external impacts which might be faced by a rotor in a real environment. As with all blade mounted actuators, additional weight has also to be considered.

Mechanical Flaps

On a conventional rotor blade, the circulation hence lift, varies with the angle of attack. The blades ability to produce lift is limited by its stalling incidence. It has already been stated that extending the limits of helicopter rotor performance calls for control of lift generation independent of incidence. Commonly employed on fixed wing aircraft, mechanical flaps can be used to greatly increase the lift which may be generated. A flap deflection alters the effective sectional geometry and therefore the circulation.

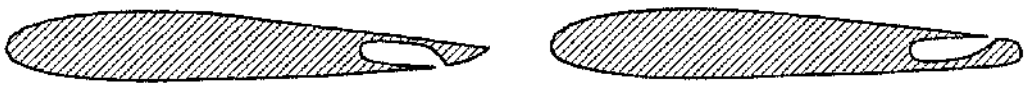

Figure 1.4: **Circulation Control Aerofoils**

Unfortunately, aerofoils which employ flaps tend to stall at incidence lower than the stalling incidence of their unflapped equivalent owing to separation of the flow ahead of the flap. A method of improving this situation is to blow high pressure air tangentially over the flap from slots at its hinge, to either delay separation or induce reattachment. The concept of 'blown flaps' has been around for a number of years now, and there are successful examples of its use in service on fixed wing aircraft (for example, the Buccaneer uses blowing at the leading edge and over the flaps[34] to maintain attached flow).

Jet Flaps and Circulation Control

Dispensing with the need for a mechanical flap and using instead a jet sheet directly from the trailing edge, the original 'jet flap' (now sometimes referred to as the 'pure jet flap') effects control by varying the jet strength hence the effective chord of a 'virtual' flap. Although large lift coefficients are possible, lift versus jet momentum efficiency is low. In the fifties, early advocates of jet flaps saw their potential for improved integration of lift production, directional control and propulsion on fixed wing aircraft [35]. For this type of application the large jet momentum provides also the thrust.

A more efficient variation of the jet flap makes use of the Coanda effect. A Coanda surface is employed on the airfoil underside at the trailing edge, the circulation is dependent on the position of jet detachment and therefore on the jet momentum.

When the blowing is tangential to the upper surface and when the entire trailing edge is rounded then it is possible to exercise greater control over the deflection of the Coanda sheet. In the literature, this is more commonly referred to as a circulation control aerofoil. Figure 1.4 illustrates two circulation control aerofoils. Cheeseman

and Seed[34], and Wood and Nielsen[36] provide reviews of the development of circulation control methods from a rotor craft perspective.

Raghavan et al.[37] performed laminar CFD computations of circulation controlled cylinders and elliptic aerofoils. These were either set in an unsteady freestream or were subject to unsteady blowing (though not both these conditions at the same time). On comparing lift and drag results with experimental data it was concluded that more detailed modelling was required. Ghee and Leishman[38] also considered unsteady blowing for circulation control of a cylinder, discussing the dependence on freestream Mach number and reduced frequency of actuation. With a view to higher harmonic control, Lorber et al.[39] used a pulsed jet to perform experiments at values of Mach number, Reynolds number, pitch angle, jet momentum coefficient and jet oscillation frequency to represent full scale conditions for helicopter rotor operation. The jet oscillation frequency was varied up to 25 Hz, which roughly speaking corresponds to about three or four oscillations per blade rotation. Results were very satisfactory under these conditions; Cn (and Cm) changing almost linearly with jet momentum and with almost immediate response to jet variation.

Elements of the above concepts have also been used in combination. Blowing from a 2-D slot located at the hinge of a large mechanical flap on a NACA-0015 wing, it was determined by Seifert et al.[40] and by Nishri and Wygnanski [41] that oscillatory blowing was more effective for separation control (over the flap) than steady blowing. Their oscillatory blowing essentially had an unsteady component superimposed on a steady mean jet flow and was described using two blowing momentum coefficients. In subsequent experiments[42], coherent structures introduced by oscillatory blowing were shown to be the reason for its superiority, these also gave post stall improvement. Stall was delayed and post stall performance again improved by similar oscillatory blowing from a slot close to the leading edge ($x/c = 0.1$). The best results were achieved with forcing frequencies corresponding to the most unstable frequencies of the separating shear layer. It was found to be beneficial to reduce the steady jet momentum to zero as the separation location moved towards the actuator location, leading to essentially zero net mass addition actuation. The methods were also investigated for suppression of dynamic stall by Greenblatt and Wygnanski[43] and Greenblatt et al.[44]. Useful increases in $C_{l_{max}}$ were reported.

The preceding methods of improving helicopter performance have some common limiting factors. Each of them is likely to increase the blade complexity and weight and none can be implemented without development of complicated control algorithms, which for adequate let alone optimal control will involve consideration across a large multidimensional parameter space. Conceptually some of the schemes have been around for a relatively long time and whilst never being ruled out have yet to progress from simplified investigations. Design alterations which quickly find their way to operational testing tend to be those which can be easily incorporated on existing aircraft. This in mind, a formidable obstacle for methods which use jet blowing is the increased complexity of the hub. On most typically proposed systems, air is bled from the engines and pumped to locations where blowing will be effective. This is complicated on a rotor, since it is necessary to regulate the jet strength depending on the azimuth position, and on a more comprehensive system, as a function of spanwise position. Asides from inefficiencies associated with throttling of the bleed, the required 360-degree continual flow regulation through the already complex rotating hub presents an immense complication. For rotorcraft application, it would be more convenient to have discrete flow control devices which do not require hub based pumping and throttling of a secondary air supply.

1.4 Synthetic Jets

The phenomena of acoustic streaming, whereby a jet flow is induced by an oscillating boundary, has been discussed over centuries. More recently it has been observed that the effect can be considerably enhanced if the oscillating surface operates inside a cavity. Ming et al.[46] used a loudspeaker fitted with a brass nozzle, claiming this as a new phenomenon. Ming et al. also claimed that the approach had been successfully used for separation control. Chang et al.[45] connected a loudspeaker to a plenum inside a wing. A slot opening located close to the leading edge allowed excitation of the external flow. Low level excitation at the shear layer instability frequency was found to delay separation, hence stall. Stronger forcing was successful over a wider frequency range however, and this was attributed to the unsteady introduction of vortical disturbances.

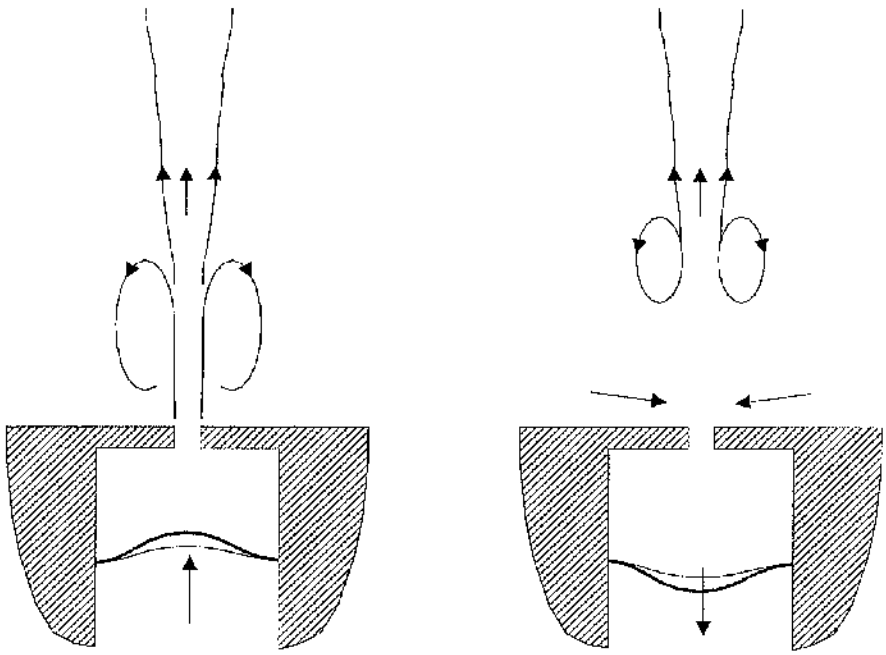

Figure 1.5: **Synthetic Jet Illustration**, actuators are illustrated during blowing (left) and suction (right) schedules. During blowing there is a focussed expulsion from the deforming cavity. During suction there is a diffuse intake.

The actuator used by Ming et al.[46] might now be described as a synthetic jet actuator. Recently such actuators have been attracting increasing attention for the treatment of a number of flow control problems. A synthetic jet flow is created by the entrainment of otherwise ambient fluid. The jet is not a secondary fluid injected into a primary atmosphere, rather the jet is '*synthesized*' from its surroundings. The most commonly proposed synthetic jet actuator comprises an oscillating surface such as a piston or diaphragm enclosed in a rigid cavity which has an opening to the ambient atmosphere. This is illustrated in figure 1.5. When fluid in the cavity is compressed an amount is expelled via the opening. When the cavity volume is once again increased, fluid is instead ingested. The opening effectively acts as a nozzle for flow alternately travelling to and from the cavity. On the compression stroke, escaping fluid separates at the exterior edge of the opening. The resultant shear layer quickly begins to roll-up producing a vortex ring which surrounds the edge. A two dimensional sectional representation of the cavity shows this as separate counter rotating vortices. The vortex ring (or opposite sense vortices in 2-D) continually moves away from the exit plane as the induction stroke begins. As fluid becomes drawn into the cavity, the vortex system should be sufficiently removed so that its motion is little affected by the intake. Repetition of the cycle, focused expulsion of fluid followed by diffuse intake, creates a train of vortices from the opening. Experiments suggest that these may quickly lose their individual identity, merging instead into a jet flow. Over a number of complete cycles, the net mass flow across the exit plane is zero, i.e. the jet flow is entirely formed (or *synthesized*) from the ambient fluid.

An alternative synthetic jet actuator, having instead, an oscillating cantilever placed over the rigid cavity has been developed by Jacobson and Reynolds[47] as a laboratory flow control device. This design, and its application for flow control, is discussed in references [48], [49] and [50].

So far, the experiments considering synthetic jets have mostly been demonstrations of their capability for flow control and potential for improvement of aerofoil performance. Such experiments consider the use of actuators for the alleviation of blade vortex interaction (BVI) effects[51], aerofoil lift improvement[52][53][54], for control of forebody flow assymmetry[55](e.g. missile forebodies), flow control over a

cylinder[56][57][59][60][61][62], separation control over a backwards facing step[59] and for the vectoring of a primary jet[63]. There have also been some studies which look more specifically at how a synthetic jet is developed. In either case, investigations are thinly spread over a range of configurations and operating conditions, so that most results stand almost alone, without further independent verification elsewhere in the literature.

1.4.1 Jet Actuator in an Otherwise Stagnant Atmosphere

Amongst the available literature, operating conditions have been replicated and results corroborated for only particular cases of a synthetic jet issuing into a quiescent atmosphere. From Schlieren images and hot wire anemometry, the formation of a zero-mass jet is explained by Smith and Glezer[64]. A circular deforming diaphragm, set in a cavity and having a high aspect ratio (0.5mm x 75mm) rectangular orifice was used to develop the jet. For the hot-wire experiments, the diaphragm deflection amplitude was controlled while all other parameters, including the frequency of deformation, were fixed. Results of this investigation describe the development of the escaping vortices and their transition to turbulence for a nominal case (i.e. for fixed operating conditions).

The operating conditions of the Smith and Glezer nominal case[64] were roughly adopted for the RANS two-dimensional CFD simulations of Kral et.al.[65] who imposed a sinusoidal velocity boundary condition to represent the flow at the jet exit, and also for the two and three-dimensional DNS simulations of Rizzetta et al.[66]. The latter initially began by modelling a domain which included the cavity from which the jet is developed.

Mallinson et al.[67] performed RANS simulations as well as experiments. They used similar operating schedules to those of Smith and Glezer[64], Kral et al.[65] and Rizzetta et al.[66] and some qualitative agreement with these authors was found even though Mallinson et al. used an axisymmetric formulation to represent a circular jet orifice.

Other papers which consider a synthetic jet actuator operating in an otherwise still atmosphere, but under operating or freestream conditions which differ from those

of Smith and Glezer[64] include the computations of Mittal et. al[68], the experiments of Smith and Swift[69], and those of Gilarranz et al.[70] and Rediniotis[59] who demonstrated that a net suction could also be produced by an axisymmetric actuator. Earlier, Coe et al.[71] generated a synthetic jet using a number of adjacent actuators. The main focus of this work was in micro-machining.

1.4.2 Adjacent Synthetic Jet Actuators

Papers discussing the future use of synthetic jet actuators generally anticipate these being arranged in arrays. So far however, there is very little in the literature that looks closely at the interaction between actuators when a number of these are placed in close proximity. Smith, Trautman and Glezer[72] used PIV to experiment with two high aspect ratio jets placed parallel to one another. Issuing into a stagnant atmosphere, these were found to merge into a single jet flow, the development and subsequent behaviour of which was studied. When there was a relative phase difference between the actuators, the vortices from the respective actuators were no longer horizontally-aligned, i.e. at any instant the set of vortices from one orifice had travelled a greater streamwise distance than the others. The net effect of the interaction in the region between the actuators is to turn the merged jet in the direction of the actuator which is leading in phase. If the jet is issuing into an otherwise still environment, Smith, Trautman and Glezer observed that the jet continued to cant over as the phase difference θ was increased until $\theta = 130°$ when the direction of the merged jet is tangential (parallel) to the exit plane. This last result was successfully simulated by Kral and Guo [73] using a two dimensional *RANS* approach. The operating conditions were set to reflect the experimental parameters of Smith, Trautmann and Glezer. The jet flow was imposed by a time varying velocity boundary condition which was applied within shallow cavities representing the adjacent actuator exits. Results were plotted in terms of time evolution of vorticity. The authors claimed that vorticity contour plots compared well with the experiments, but from the figures published, the comparison seems to worsen as the phase difference is increased (to $\theta = 130\,\mathrm{deg}$).

The imposition of a velocity boundary condition to represent each actuator has a

more dubious validity when a number of actuators are modelled. This is especially the case in crossflow or where the operation of each jet is not identical. In a physical experiment there would be competition for fluid between actuators and it seems reasonable to assume that the instantaneous nozzle velocity profiles of each would be significantly dependent on the operation of the others. It would be expected that suction towards each actuator exit would alter and perhaps inhibit the development of those vortices between the adjacent exits.

Smith, Trautman and Glezer[72] noticed that the outer vortices decelerated at a greater rate compared with a single (actuator) jet system. On the resultant jet, they observed generally that this spread faster with streamwise distance, with a stronger entrainment of ambient fluid.

1.4.3 Synthetic Jets in Crossflow

Thus far there has been little investigation of the operation of deforming cavity type actuators in a crossflow. Sauerwein and Vakili [74] performed water tunnel experiments with various circular and small aspect ratio rectangular orifices. Visualisations were presented, but without numerical data. The authors claim that a jet of fluid was apparent although this is not clear from the figures. These do however indicate that successive vortex rings from the same orifice did not interact but instead travelled individually downstream, canted so that their *azimuthal* axes were parallel to the downstream direction. Similar experiments have also been carried out by Wood et al.[61], who found that the interaction of successive vortex rings depends on the Strouhal number. These authors observed that the periodic actuation produced steady longitudinal vortices which were instrumental in delaying separation over a circular cylinder. Again for this paper, circular orifices were used. High aspect ratio actuators might be expected to give a different flow behaviour.

Mittal et al.[68] performed 2-D simulations of a slot actuator in various crossflow and operating conditions. Vortices created at the downstream edge of the nozzle exit were individually convected downstream. The mean velocity field produced by these contained a 'mean recirculation zone'. Although no combination of parameters produced a persisting recirculation zone, it was claimed that this finding was in

support of the results of Amitay et al.[56], who observed permanent recirculation regions.

1.4.4 Synthetic Jet Applications

A large number of papers have considered the application of the jets for the alleviation of topical flow problems and improvement of aerodynamic performance. Generally for these, only the macro effect of the jets are important, quantified in terms of for example, lift and drag coefficients C_L and C_D. There is much less emphasis on how a synthetic jet develops or how the ejected fluid interacts with the freestream.

Smith, Amitay and others[56][57][75][76] began a series of experiments, first using synthetic jets to modify the 'apparent aerodynamic shape' of a cylinder, so altering the separation position and character and hence the lift and drag. They were able to rotate the cylinder so that the angle of the jet exits could be altered with respect to the freestream. An aerofoil shaped fairing was then added on the lee side[77][58], see figure 1.6, instrumented with pressure transducers and fitted so that they were still able to rotate the cylinder, hence the actuators, on what was now effectively the aerofoil's leading edge. A number of interesting observations were made. Investigating the effect of jet location, Smith et al.[77] found that for their model the flow could be reattached on the upper surface even when the blowing was from below the dividing streamline. Under the conditions ($Re_c = 3 \text{ x } 10^5$), this indicated that the actuators were having a 'global' effect as opposed to merely interacting locally with the boundary layer. The forcing required to induce reattachment was found to be much reduced as the position of the actuators was moved further downstream. The implication of this is that for actuation upstream of separation, the level of forcing provides a means of compensating when the actuator is some distance removed from the preferred location, although the results indicated that a considerable range may be required.

In further experiments[58], this same aerofoil, nominally stalled at 5°, could with help from the jets maintain fully attached flow to 17.5°, with partial recovery of lift to still higher angles of attack. The mechanism by which this was achieved was seen to

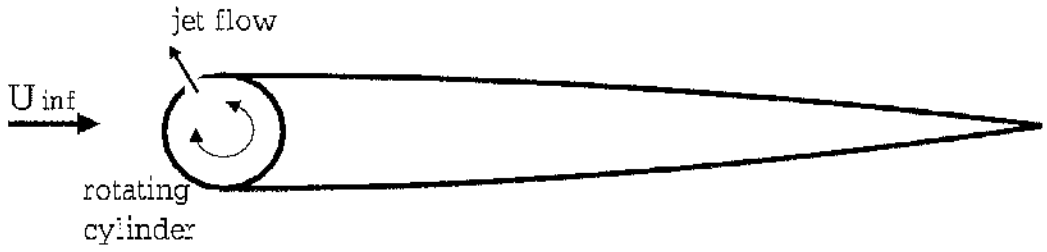

Figure 1.6: **Circular Cylinder with Aerofoil Fairing**, as used by Smith et al.[77], here the cylinder can be rotated to vary the actuator position and jet direction.

depend on the forcing frequency. At a low frequency, of the same order as the natural shedding frequency, the input forcing was naturally amplified and caused large scale vortical structures to be convected across the aerofoil surface. The unsteadiness of this process however, led to large oscillations (at the actuation frequency) of the aerodynamic forces (peak to peak ΔC_L fluctuations were witnessed, up to 55% of the mean level for attached flow). At frequencies an order of magnitude greater, the reduced scale (but increased number) of disturbances introduced, serves to displace streamlines in a fashion which modifies the 'apparent aerodynamic shape' of the aerofoil.

In water tunnel experiments, visualised using PIV, Rediniotis et al.[59] demonstrated controlled reattachment of the separated shear layer from a backward-facing step using an actuator placed on its lee.

In simulations, Hassan[51][78] demonstrated improvements in lift using a NACA 0012 profile with an array of ten zero mass jets positioned on both the upper and lower surfaces between $x/c = 0.13$ and $x/c = 0.23$. At zero angle of attack, where otherwise no net lift would be observed for the symmetrical aerofoil, it was seen that with only the jets on the lower surface enabled, improvement in the mean lift was achieved through the development of circulatory flow regions and alternate high pressure regions which then travel downstream across the aerofoil's underside. The extent of mean lift enhancement depended on a Mach number ratio, defined as M_{jet}/M_{∞}.

Hassan represented synthetic jet actuators using a sinusoidally varying velocity at

the aerofoil surface. A similar approach was taken for the work of Wu et al.[53], Ravindran[54] and Donovan et al.[52], who each present positive results for synthetic jet enabled aerofoils at post stall conditions.

1.5 Summary

Improvements in the high speed and load carrying performance of helicopters may require taking advantage of lifting potential in regions of the rotor disc where lift is currently not optimised. This will require actuation in addition to the conventional cyclic pitch control. There is evidence to show that the objective might be achieved by oscillatory blowing. It is convenient to use actuators which are blade mounted and have minimal connections. One suggested technology is synthetic jets. These introduce no net fluid mass. Instead, the actuators working fluid is the fluid in which it is embedded. The technology for producing synthetic jet actuators is rapidly developing. It has been shown that the effects of synthetic jet actuation are predictable and thus suitable for flow control. It has been reported from experiments, that settled behaviour is achieved within a small number of actuator cycles making the actuators particularly suited to control applications where time scales are small. For rotor blade application, the actuators are failsafe. Proposed actuators may be remotely activated via an electrical supply, without the need for a complicated, hub based, pumping-and-throttling air management system. They offer flexibility, i.e. microfabricated and arranged in arrays, their control could be very specific to location. The immediate challenge is to gain a better understanding of how the flow from an actuator interacts with a primary crossflow across a range of conditions and to use this knowledge to develop a control strategy.

A CFD investigation of synthetic jet actuators is performed in the following chapters. In chapter 2, a single synthetic jet developed from a deforming cavity is considered in an otherwise still atmosphere. This situation has been studied previously by a number of other authors and so allows some level of code validation. Novel contributions come in chapters 3, 4 and 5.

A synthetic jet actuator embedded in a flat plate is considered in chapter 3. There are two aspects to this chapter. First, using the actuator with different operating

settings, different flow regimes are observed. The establishment of closed recirculation regions has already been discussed by others, but previously this has only been encountered for bluff body flows. The second aspect of chapter 3 is that the deforming cavity model is compared with an alternative approach where the actuator is represented by a time-varying velocity profile. This method, and comparisons with deforming cavity flows, have also been discussed before but not for crossflow cases. This is a matter of significance; demonstrating that the exterior effect of a deforming cavity can be produced with only a simple velocity profile, it is possible to think separately about the way in which the internal actuator design affects the flow exiting the cavity from the way in which flow exiting the cavity affects the external (primary or crossflow) behaviour.

In chapter 4, freestream and operating conditions are varied and the resulting flow is categorised in terms of the external flow regime. A similar parameter study over such an extensive region of the parameter field is not found elsewhere in the literature.

The velocity profile type actuator is modelled on the surface of an aerofoil in chapter 5. The actuator exit and its immediate surroundings are modelled using a fine grid distribution to preserve small scale structures. The effect of these on local pressure distribution is studied. More commonly for CFD studies of synthetic jet enabled aerofoils, the actuators are represented at individual grid nodes and results are given in terms of the the effect on the integrated coefficients, C_l, C_d and C_m. The detail with which the synthetic jet location is represented in chapter 5, and the consideration of the response in terms of pressure distribution is a unique combination amongst the current literature.

Chapter 2

The Synthetic Jet Actuator in an Otherwise Still Atmosphere

2.1 Overview

It is first appropriate to study the operation of a synthetic jet in an atmosphere which is at rest prior to actuation. The recent surge of interest in using these actuators for flow control has placed an emphasis on their ability to synthesize a jet flow from the surrounding fluid. Physically, the otherwise still atmposphere is the simplest environment in which a jet can be produced. All flow velocities are induced by the actuation and the only geometric scales are those related to the dimensions of the actuator, making characterisation simpler. The aim of this chapter is first to develop an actuator model. The suitability of this is tested against published data derived from experiments and simulations. The model then allows an examination of the mechanisms of synthetic jet formation.

This chapter first describes the target test case. Next the particular numerical developments made to simulate the actuator are described. Numerical tests are then made to show that the conclusions are independent of the computational grids and time-step used. Comparison is then made with the published data, considering several criteria. The formation of the jet is then described.

2.2 Review of Test Case

As discussed in the introduction (Chapter 1), papers on synthetic jets broadly fall into one of four categories

1. a single zero-mass actuator operating in an otherwise still environment
2. adjacent actuators in an otherwise still environment
3. one or more actuators set in a crossflow
4. flow control *applications* where zero-mass actuators may be appropriate.

Within these categories, the case of a single jet operating at conditions similar to those used by Smith and Glezer[63] is the most repeated. The works of Kral et al.[65] and Rizzetta et al.[66] are simulations of this experiment. These, and Mallinson et al.[67](computation and experiment), offer corroboration to an extent not available for other cases.

For comparison with and between these papers[63][65][66][67], there are a number of prominent criteria,

1. **jet exit velocity profiles** averaged over a cycle and at instants $\omega t = \pi/2$ and $3\pi/2$[66].
2. **profiles of the streamwise velocity** are given for various distances from the jet exit in references [63][65][66][67], and provided the main comparison for the simulations of Kral et al.[65] and Rizzetta et al.[66] which agreed well with the measured profiles[63], except at the jet edges.
3. **streamwise variation of the jet half-width** is a measure of the jet spreading given in[63][65]
4. **time history of the centreline velocity** was measured experimentally in [63], and used for comparison in [66]
5. **decay of the centreline velocity** was plotted in [63][65][66][67]

6. **Qualitative Description of the Jet Formation** process using Schlieren visualisation, vector and contour plots was given in [63][65][66][67]. These indicate the scale of the vortex pairs and the distance they travel before dissipating.

For the current study, computations are made of a flow situation following cases described by Smith and Glezer[63], Kral et al.[65], Rizzetta et al.[66] and Mallinson et al.[67]. An actuator having an exit width $h = 0.5mm$, operating at 1000Hz and issuing into an otherwise still environment with a peak exit velocity of around $20-25$ m/s emerges as the best test case.

2.2.1 Results of Smith and Glezer[63]

Smith and Glezer[63] used an actuator with a circular diaphragm set in a cavity. The interior dimensions of the cavity are undisclosed, and this may well also have been circular. A slot exit (to the ambient exterior) of $0.5mm$ x $75mm$ is described, i.e. a rectangular exit. The diaphragm was driven at resonance, which was nominally $1140Hz$. For smoke visualisations of the jet development in the spanwise direction, the operating frequency was reduced to $360Hz$. These visualisations identified a spanwise instability which the authors suggested as being responsible for the breakdown of the primary vortex cores. Schlieren images were used to show this breakdown in the plane normal to the (slot) span. Based on a velocity at the exit plane U_0 and the slug length L_0, a Reynolds number, Re_{U_0} describes the synthetic jet,

$$U_0 = L_0/T \tag{2.1}$$

$$L_0 = \int_0^{T/2} u_0(t)dt \tag{2.2}$$

where T is the actuator period. The exact definition of u_0 is not given, and so it is unknown if this is a peak value at the centreline, or an average to take account of the distribution across the nozzle exit. Measurements were made using hot-wire anemometry. The values of Re_{U_0} varied between 104 and 489, the nominal case having $Re_{U_0} = 383$.

If u_0 varies sinusoidally in time as,

$$u_0(t) = V_0 sin(\omega t) \tag{2.3}$$

then these values correspond to a Reynolds number, Re_{V_0} in the range 320 to 1500, with the nominal case having $Re_{V_0} \approx 1200$. For this case, the vortices produced by actuation were found to remain laminar and intact beyond $y/h = 8.5$, before transition to turbulence and breakdown. Hot wire results were used to produce a number of plots describing the transport of the primary vortices, the jet velocity and its time variation.

2.2.2 Results of Kral et al.[65]

By imposing a velocity at the boundary , Kral et al.[65] compared a number of actuator configurations. Laminar and turbulent flow conditions were modelled. Synthetic jet flows were initiated by an exit velocity,

$$\overline{u}_n(\xi = 0, \eta, t) = U_0 f(\eta) sin(\omega t) \tag{2.4}$$

where ξ and η denote the streamwise and cross-stream directions respectively, $\overline{u}_n$ is the streamwise velocity and,

$$f(\eta) = \begin{cases} 1 \\ sin(\pi\eta) \\ sin^2(\pi\eta) \end{cases} \tag{2.5}$$

The synthetic jets were compared against steady jets and pulsed blowing (i.e. without a suction schedule).

Time-step independence was not discussed. The published results were calculated using a dual time method employing 100 real time steps per actuation cycle and with approximately 50 subiterations per real time-step. A grid of 161 x 325 vertices was used for an actuator having a nozzle exit width of $0.5mm$ in a $16mm$ x $18mm$ domain. A detailed grid resolution study was not given. It was claimed however, that calculations on a coarser grid having 70 x 111 vertices over a $12mm$ x $12mm$ domain, captured the basic flowfield but in less detail.

Comparisons were made with the experiments of Smith and Glezer[63]. Laminar modelling of synthetic jet actuation failed to produce a jet flow. Without the turbulent dissipation, the vortices produced over each actuation cycle fail to break down into a mean jet flow and are instead convected out of the domain. For the turbulent synthetic jet cases, a top-hat velocity profile ($f(\eta) = 1$) was found to gives the best comparisons. However in order to have equivalent mass flux for each of the velocity profiles used and so compare their *relative* performance, different nozzle exit widths were used in each case. Qualitatively, velocity vector plots and vorticity contour field plots agreed with the experiments. Streamwise profiles were normalised by the jet half width and by the freestream velocity and also showed good agreement. However, this normalisation procedure aids agreement by causing some data points to be fitted. The comparisons improve with increasing distance from the actuator. At the jet edges however, there are significant discrepancies, the computed velocities being clearly greater than those reported from experiment.

2.2.3 Results of Mallinson et al.[67]

Mallinson et al.[67] performed both hot-wire experiments and computations. Their experimental actuator had a circular nozzle. The computations again represented the flow from the actuator nozzle by an imposed velocity. The formulation assumed axisymmetric flow about a fixed jet centreline. No mention was made of time-step resolution. Published results are computed on a grid having 110 x 151 nodes over a simulated domain of $12.75mm$ x $32.0mm$ (in their experiments, the minimum nozzle exit width was $0.5mm$). In comparison with results generated using half the number of cells, it was stated that only small differences were observed. The flow from an axisymmetric actuator could be expected to be quite different from that using a high aspect ratio slot. The comparison that Mallinson et al.[67] make with the other papers, is mostly qualitative. They observe that regions of standing vorticity of opposite-sense become established downstream of the actuator exit, noting the resemblance with the descriptions of [63] and [65]. These regions were fed by vortices produced at the nozzle over each actuator cycle.

2.2.4 Results of Rizzetta et al.[66]

The DNS / Chimera grid calculations of Rizzetta et al.[66] initially included a deforming cavity. Exit profiles were first generated and then imposed simply as velocities on a grid having only an exterior domain. No asymmetry about the nozzle centreline was observed and so published results were calculated on a further reduced grid having a symmetry boundary along the jet centreline. To qualify grid and time-step independence, Rizzetta et al.[66] show time histories of the jet centreline velocity at two streamwise locations. These are identical for coarse and fine grids, and show only a small discrepancy for only a part of the cycle when considering the three different time-steps which were used. Grid independence away from the locations considered is not however certain; Rizzetta et al.[66] found it necessary to stretch the vertical grid point distribution towards the upper boundary in order to overcome 'numerical anomalies'. It is conceded by these authors that this grid stretching makes resolution of vortex convection valid for only a limited distance. Comparison is made with the experiments of Smith and Glezer[63] in terms of normalised streamwise velocity profiles. Similar discrepancies were apparent at the jet edges as previously discussed for Kral et al.[65]. Conclusions especially pertinent for the current work, are that an exact modelling of the cavity geometry (and presumably its deformation) is vital to exit profiles and subsequent jet formation. Two and three dimensional results were presented. For two-dimensional cases, a train of vortices was seen to develop from the exit, i.e. these did not break down or merge into a turbulent jet flow. These authors concluded that it may be necessary to model in three dimensions to simulate the mechanisms of vortex breakdown / dissipation.

2.3 Numerical Formulation

This study uses the University of Glasgow compressible flow solver *pmb2d*[79]. The baseline code is summarised in Appendix *A* which is adapted from reference [80].

Previously Kral et al.[65] have represented the flow from a synthetic jet actuator by imposing a time-periodic velocity at the jet exit. This method also requires a suitable treatment of the other flow variables. Whilst the use of a periodic velocity boundary condition guarantees that the average velocity is zero over the actuation

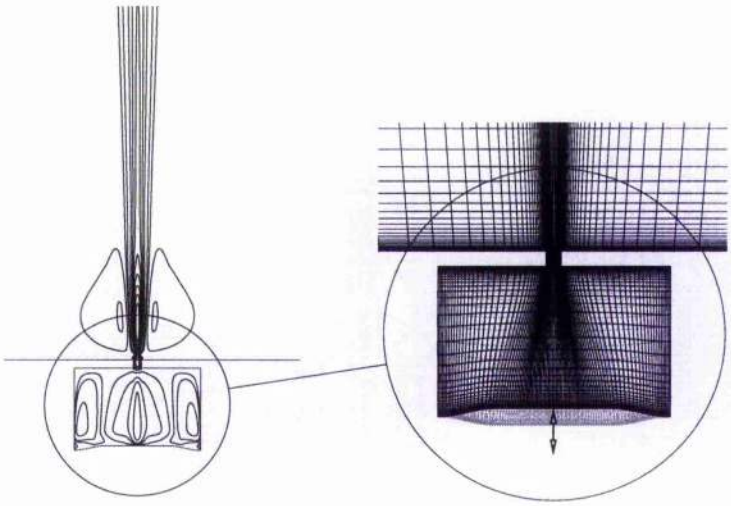

Figure 2.1: **Jet Flow from a Deforming Cavity**

period, for a zero-mass jet, a simultaneous treatment of the time dependent density is needed to satisfy,

$$\oint dm = \oint \rho(x,t)\ h\ V_0 \sin(\omega t) dt = 0 \tag{2.6}$$

The requirement to devise pressure, density and turbulent parameters at the jet exit boundary may be circumvented by modelling the full deforming cavity. This is the approach taken in this chapter. The main modification to the baseline code is for grid deformation, described in this section. Also discussed are the grids used for the current study and the boundary conditions.

2.3.1 Grid Deformation

There are many situations in CFD where an ability to alter the grid between time steps is useful or essential. For domains incorporating a single rigid moving body, a simple translation of grid points may be made. For such a problem, the relative position of points to one another, and hence the overall shape (if not the orientation) of the grid, is unchanged. An example of this is a pitching aerofoil, where the entire grid can be rigidly rotated about the pitching centre, through an angle

representing the incremental change in angle of attack. For domains which incorporate a deforming body or which have two or more components whose position relative to one another is changing, simple translation and rotation of an initial grid is not possible. An example of this is an airfoil and moving flap configuration. The synthetic jet actuator having a deforming cavity floor, also falls into this category, i.e. the cavity floor moves relative to the other walls, the nozzle and the exterior surfaces (see figure 2.1). For this problem, it is necessary to have a different grid at each time step in which a shape deformation has occurred. Since the motion of the cavity floor is a required input, the difference between successive grids is known, facilitating automatised grid regeneration.

The current work uses multiblock grids, where the domain is divided into a number of subdomains, or blocks, each of which has its own structured grid. The grid points along any block boundary are shared with adjacent blocks. Block structured grids are especially suitable for automated deformation of grids where localised deformation is required.

The deforming cavity used in current studies has exactly the same initial (mean or undeformed) dimensions as used by Rizzetta et al.[66] for their *DNS* study. These authors however, moved the entire cavity floor vertically, in the manner of a close-fitting rigid piston. For the current investigation, the motion of the cavity floor more closely resembles that of a diaphragm, with the lower corners of the cavity fixed. The cavity is shown on the right side of figure 2.1, which illustrates the extremes of the cavity floor deformation. In achieving the deformation of the cavity, the x coordinates of grid points along the cavity floor are unchanged in time. Referring to figure 2.2 for dimensional descriptors; along the cavity floor $y = y_d(x, t^*)$ and the deformation is given by,

$$y_d(x,t) = A \sin^2 f(x) \sin(\omega t) - r \tag{2.7}$$

where,

$$f(x) = \begin{cases} \frac{2\pi}{q}(x+s) & -s \leq x < 0.25q - s \\ \frac{\pi}{2} & 0.25q - s \leq x \leq 0.75q - s \\ \frac{2\pi}{q}(x+s) - \pi & 0.75q - s < x \leq q - s \end{cases} \tag{2.8}$$

GRID	CAVITY	NOZZLE	EXTERIOR DOMAIN
fine	191 x 87	51 x 55	179 x 81
medium	96 x 44	26 x 28	90 x 41
coarse	73 x 25	13 x 25	65 x 31

Table 2.1: Summary of Deforming Cavity Grids

This is relative to an axes system where the x-axis runs along the actuator exit plane and the y-axis runs vertically along the *left* side of nozzle.

Having determined the grid point coordinates for the next time step, of points along the moving block boundary, the new position of interior grid points is then calculated using Transfinite Interpolation (TFI) to redistribute these between the revised boundaries.

By setting the amplitude of maximum diaphragm displacement to $A = 0.5467h$, the volume displaced by the diaphragm motion corresponds to Rizzetta's piston (where $A = 0.41h$).

2.3.2 Grids and Boundary Conditions

Three grids have been used in this chapter to consider the effects of grid point density. These are described as a fine grid, a medium grid (which has been derived from the fine grid by removing every second grid point in each direction) and a coarse grid. Each grid comprises of seven blocks. Blocks 1, 2 and 3 are inside the cavity as indicated in figure 2.2, block 4 represents the nozzle and 5, 6 and 7 are the exterior environment. Detail of the grid points used in each of these regions is given in table 2.1. All of the grids have the same spatial dimensions; the undeformed cavity measures $15h$ x $10h$, the nozzle is h x h and the exterior is $106h$ x $150h$ where h is the nozzle width.

When modelling a synthetic jet actuator including the deforming cavity, solid surfaces are modelled using the established adiabatic wall boundary conditions, as described in Appendix A. This includes the surface of the deforming diaphragm.

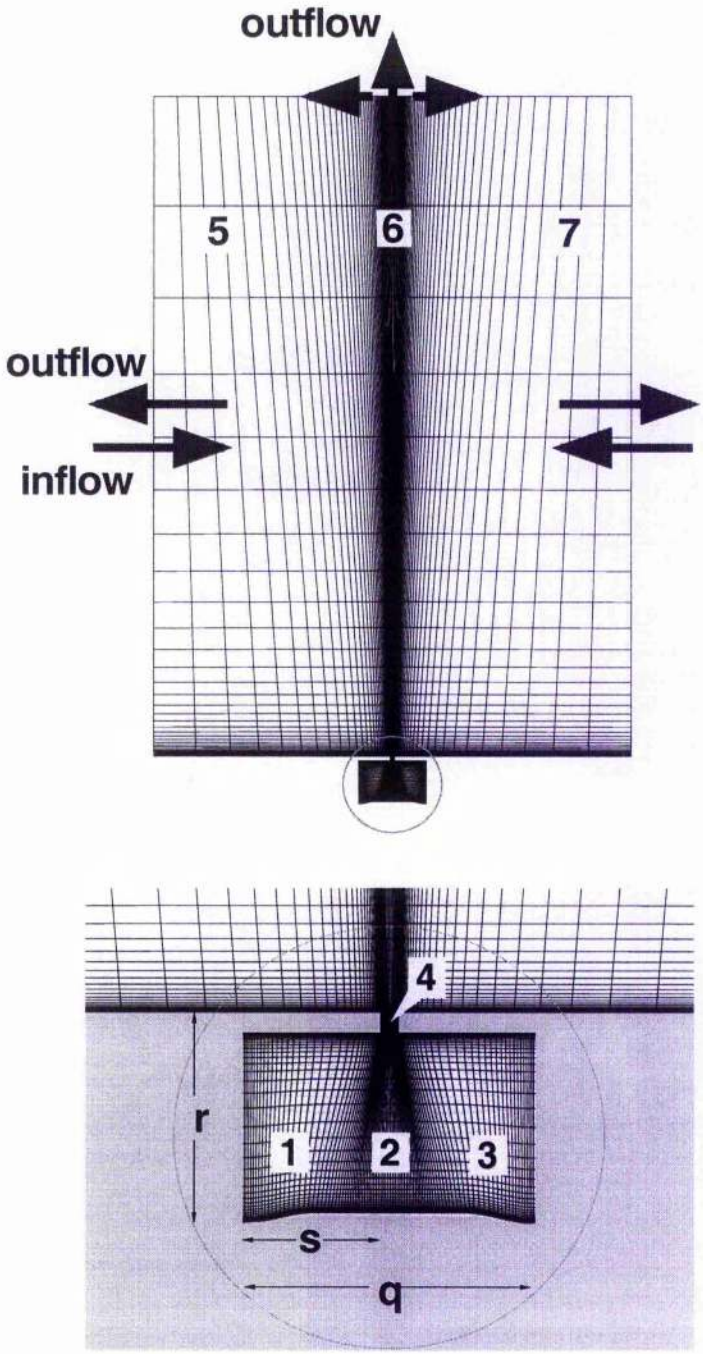

Figure 2.2: **Deforming Cavity Grid, top;** domain for the synthetic jet / still atmosphere model showing directions of flow and block numbering, lower edges of the domain and cavity surfaces are treated as solid walls, $v = 0$ at the left and rightmost vertical boundaries. **bottom;** close-up of the deforming cavity

Whether the synthetic jet is generated from an imposed periodic velocity condition or from the complete modelling of a deforming cavity, boundary conditions on the free boundaries are more problematic. The difficulty is that any boundary used to define a computational domain, especially those aligned in the general direction of the jet flow, and which is placed within reasonable distance of the jet exit, should allow disturbances to pass out of the domain. For a rectangular domain, especially on the jet-aligned (i.e. vertical) boundaries, inflow or outflow cannot be presumed. For subsonic boundaries, consideration of the characteristics indicates that for outflow boundaries one variable must be explicitly specified, however for inflow boundaries three are required.

For current calculations,boundaries of the exterior have the pressure and density set with freestream values ($p^* = 1/\gamma M_\infty^2$, $\rho = \rho_\infty$). In addition, the right and left-most exterior boundaries have the v component of velocity, i.e. the streamwise component, set so that $v = 0$. This assumes that in physical reality, flow which is tangential to these boundaries is considerably less than flow in a direction normal to them.

2.4 Numerical Tests

In order to show that the flow behaviour is adequately approximated, it is necessary to first show that the solution converges with increased grid resolution and decreased time steps. The impact of these factors is considered in this section.

Solutions developed on the medium and coarse grids show vortices emanating from the cavity. These then feed into regions of opposite sense vorticity either side of the cavity exit between which a jet forms. This is consistent with the mechanisms described in the literature. Solutions developed using the fine grid show some marked differences however. In this case, the flow is asymmetrical inside the cavity and its nozzle, and in the exterior domain. The reasons for this behaviour need to be considered. It is hypothesized that this is borne out of a failure for vortices produced by the actuation to sufficiently dissipate.

In physical reality, the dissipation of flow structures is solely a viscous effect. In a CFD solution however, dissipation has an additional numerical source which is

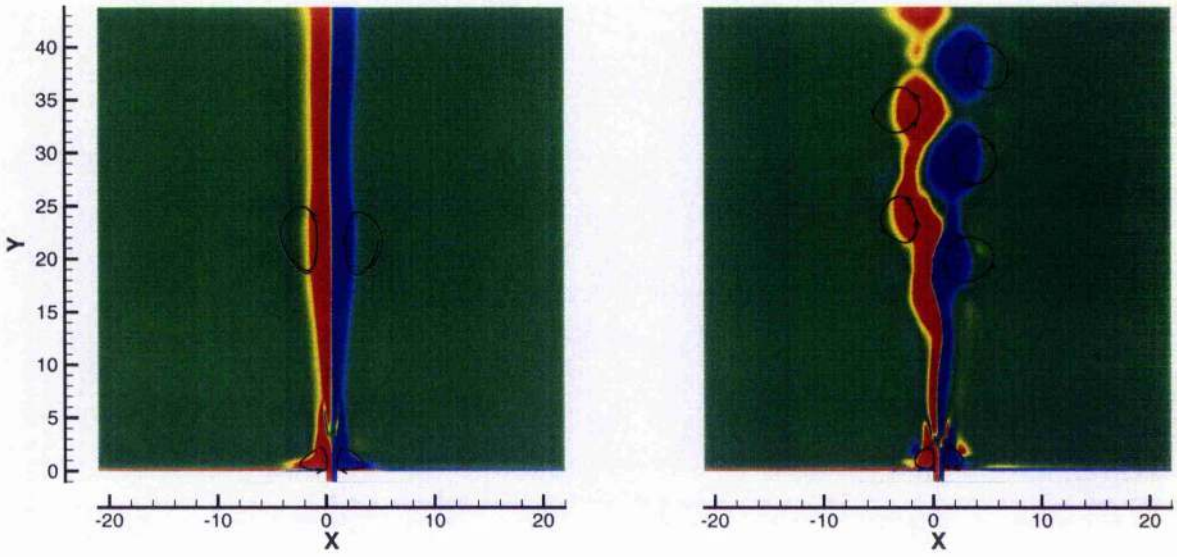

Figure 2.3: **Influence of Grid Density on Flow Behaviour**, Colour contours of vorticity illustrate symmetric and asymmetric flow behaviour. The location of vortices is indicated by streamtraces. **left:** symmetric flow calculated on the medium grid, **right :** asymmetric flow calculated on the fine grid.

dependent on the grid spacing. In either case, the degree of dissipation is significantly increased if the flow is turbulent. The results of Smith and Glezer show that synthetic jet flow becomes turbulent only a short distance downstream of the actuator exit plane. Dissipation observed in CFD solutions which attempt to mimic their experiments has a dependence on the turbulence modelling.

Turbulence is produced in regions of fluid shearing. It is largely introduced at solid surfaces in the CFD solution, via the wall boundary conditions. Turbulence levels within the current computed jet flows are low and the results are found to be essentially laminar. Turbulent dissipation is compensated by numerical dissipation due to grid stretching however, and this is greater for medium and coarse grids.

There are both computational and physical reasons why highly resolved solutions of laminar synthetic jets may be asymmetric. The laminar pulses being modelled may be naturally unstable; the alternate shedding of vortices which occurs for bluff bodies at low Reynolds numbers is an example of a similar, natural phenomena. Also, CFD solutions may be prone to the partial reflection of acoustic waves from the domain boundaries. This is entirely an effect of modelling. Although the direct impact of reflected waves on flow structures existing within the domain may be small, it may be sufficient to induce instabilities.

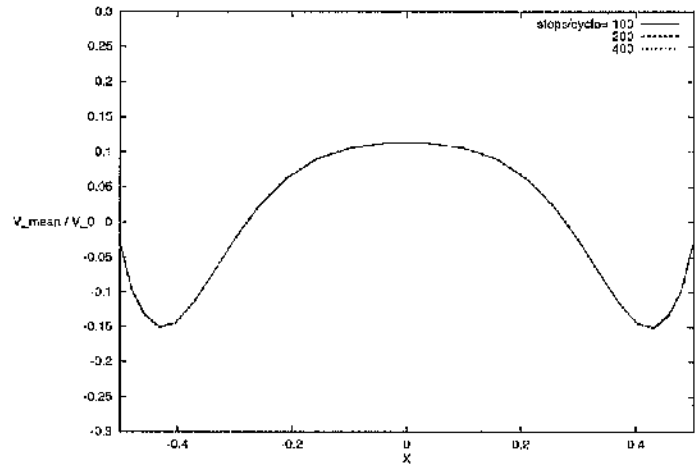

Figure 2.4: **Time-Step and Mean Exit Velocity Profiles,** Results calculated on the medium grid are identical and appear as a single line.

Jet exit velocity profiles from the medium grid are shown in figure 2.4. These

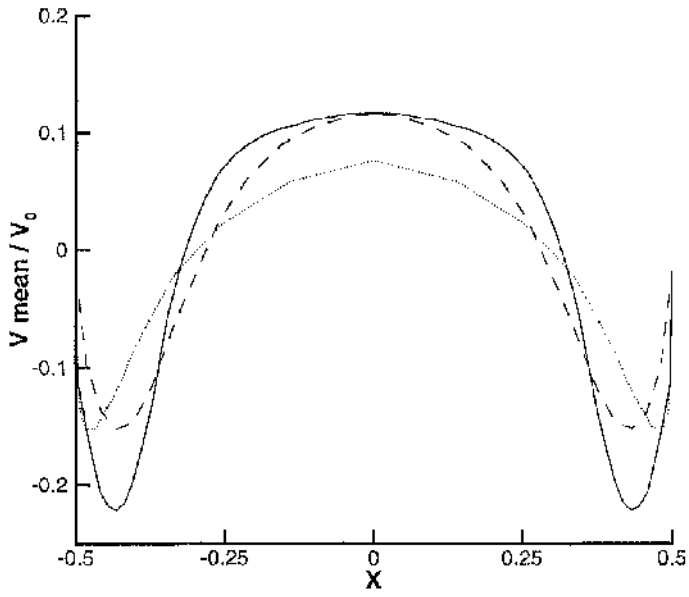

Figure 2.5: **Grid Density and Mean Exit Velocity Profiles, solid:**fine grid, **dashed:**medium, **dotted:** coarse

have been averaged over a complete actuator cycle. The almost exact overlapping of results obtained using 100, 200 and 400 time-steps per cycle indicates that the results obtained using 100 time steps per cycle are independent of time step.

The instability which is apparent in figure 2.3, develops over a number of cycles. The asymmetry begins downstream of the exit, and works its way back towards the nozzle over a number of cycles. Exit profiles calculated on the fine, medium and coarse grids are compared in figure 2.5. Fine grid results are taken on the 6th cycle. At this point, flow from the cavity is still symmetric. The plots show the same trend in each case, i.e. a mean suction at the jet edges and mean blowing in the centre. Suction peaks are considerably greater for the fine grid. At the nozzle centre, profiles are successively fuller and the mean velocity at the centre shows a convergence with increasing grid density.

The mean streamwise velocities are normalised in the manner of Smith and Glezer. The normalisation uses the cross-stream distance at which the streamwise velocity has decayed to half its centreline value. Figure 2.6 shows results from the medium

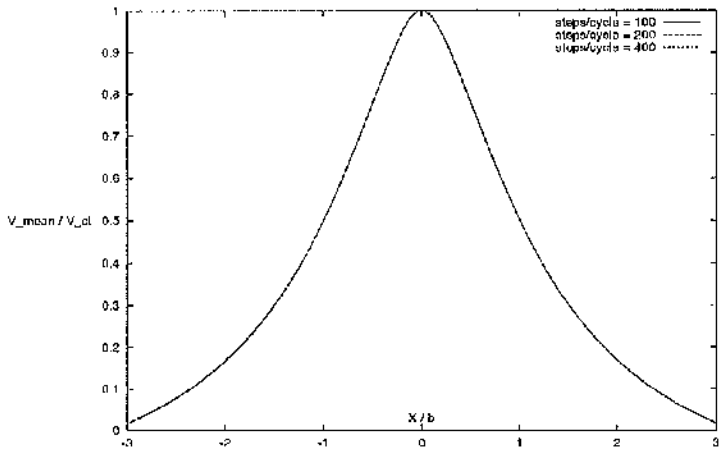

Figure 2.6: **Time-Step and Normalised Streamwise Velocity** vs. x/b, $y/h = 35.4$, Results calculated on the medium grid are identical and appear as a single line.

grid at a centreline location of $y/h = 35.4$. This is relatively far downstream. Since the difference between cases should become increasingly apparent in the downstream direction, the overlapping of results obtained using 100, 200 and 400 steps per cycle again indicates that 100 time steps per cycle is adequate.

Cycle-averaged profiles calculated on fine, medium and coarse grids are compared in figure 2.7 at a downstream location, $y/h = 9.8$. Once again, the fine grid results have been obtained by averaging over the 6th cycle. Profiles are similar over the jet centre. Successive refinement causes the normalised velocity to be increased at the jet edges. The normalisation procedure means that for a symmetric jet, some data points occur automatically, i.e. $v/V_{cl} = 1$ at the jet centre, and $v/V_{cl} = 0.5$ when $x/b = \pm 1$. For the results in the figure, the half-width b, has been calculated as the average of half-width to the right of the geometric centre, and half-width to the left. A slight asymmetry of the fine grid synthetic jet flow can be seen in figure 2.7. This behaviour determines that $v/V_{cl} \neq 0.5$ when $x/b = +1$ for the affected cases.

Streamwise profiles are shown for downstream station, $y/h = 35.4$ in figure 2.8. Fine grid results are omitted since the asymmetry at this location is such that the peak streamwise velocity differs considerably from the velocity at the geometric centreline, and results are not comparable. The streamwise profile for the medium grid is fuller

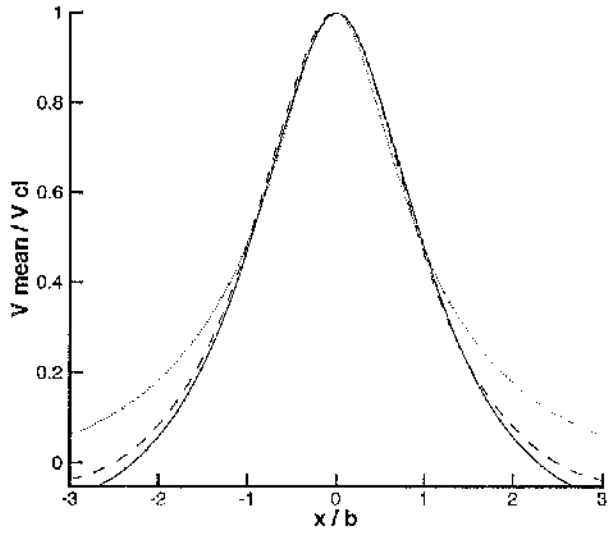

Figure 2.7: **Grid Density and Normalised Streamwise Velocity**, $y/h = 9.8$, **solid:**fine grid, **dashed:**medium, **dotted:** coarse; There is significant variation at the jet edges.

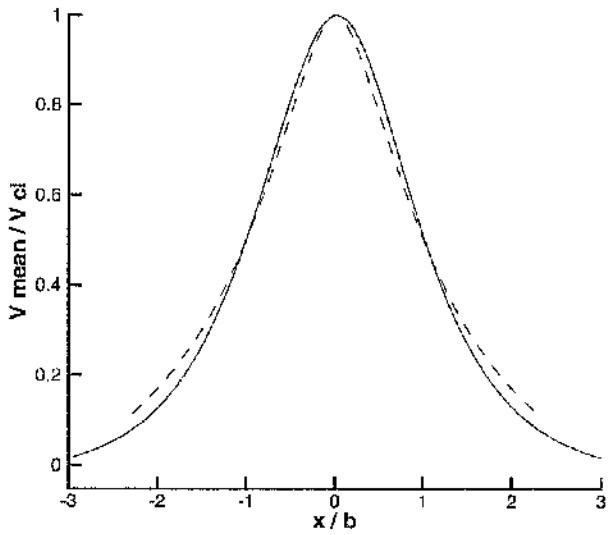

Figure 2.8: **Grid Density and Normalised Streamwise Velocity**, y/h = 35.4, **solid:**medium grid, **dashed:**coarse grid

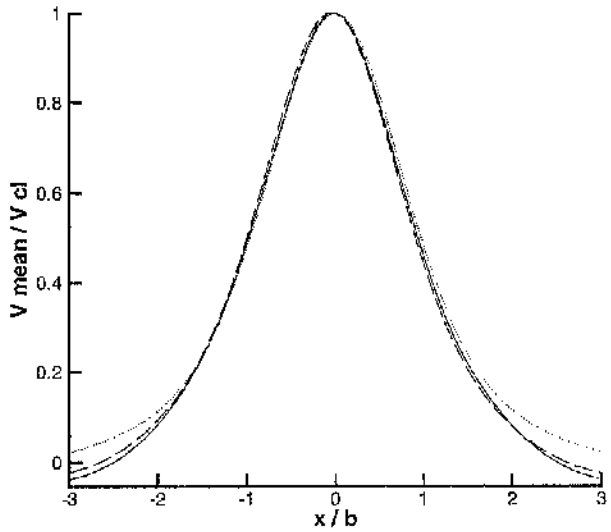

Figure 2.9: **Normalised Streamwise Velocity Demonstrating Self-Similarity**, calculated on the medium grid at streamwise locations, **solid:** y/h = 9.8, **dashed:** y/h = 23.6, **dotted:** y/h = 35.4

than in figure 2.7, with increased normalised velocity at the jet edges. However, the normalised coarse grid profile is sharper than at $y/h = 9.8$.

Figure 2.9 shows mean streamwise velocity profiles calculated on the medium grid at different stations. Broadly the same profile shape is seen for each plot, establishing a degree of self-similarity.

Normalised velocity profiles allow investigation of synthetic jet self-similarity. However, significantly different jet flows may share the same profiles. A thorough description of the flow behaviour requires also a knowledge of the normalising coefficients, V_{cl} and b. The streamwise decay of centreline velocity, V_{cl}, and the increasing jet half width b, are shown in figure 2.10 for medium and coarse grids. These have been plotted in the manner of Smith and Glezer.

The centreline velocity continues to increase after the exit plane between the regions of standing vorticity, until $y/h \approx 10$ after which there is a slow decline. This is due to the entrainment of surrounding ambient fluid. Spreading of the jet means that the initial momentum is shared by an ever greater mass. After $y/h \approx 25$ on the coarse

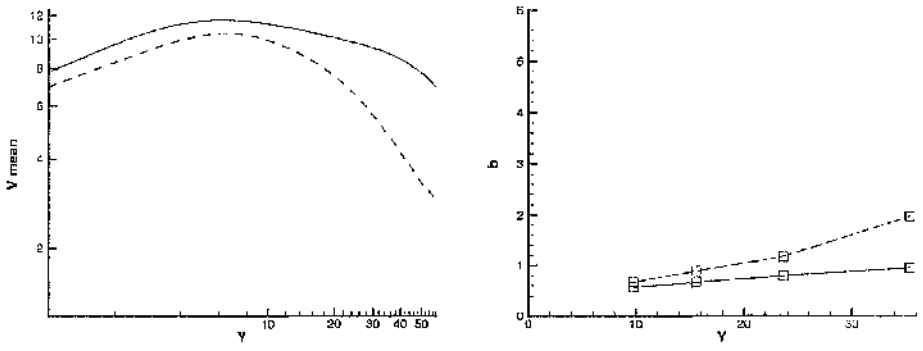

Figure 2.10: **Centreline Velocity Decay and Jet Spreading**, **left:** decay of centreline velocity calculated on the medium (**solid**) and coarse (**dashed**) grids. **right:** jet half-width, calculated on medium and coarse grids.

grid, and $y/h \approx 40$ on the medium grid, the centreline velocity decays more rapidly. It is thought that this corresponds to the position of the jet front after 10 cycles. Results for medium and coarse grids demonstrate the same trend. Velocities are lower on the coarse grid and the data diverge after the peak velocity is reached. The increasing difference after $y/h \approx 10$, between coarse and medium results indicates different spreading rates.

Jet half width b, is plotted on the right of figure 2.10. The spread of the jet is examined at discrete locations, $y/h = 9.8$, 15.6, 23.6 and 35.4. In each case the behaviour is consistent with the decaying centreline velocity. The jet spreads faster on the coarse grid. At $y/h = 35.4$, the change of gradient occuring at the jet front and observed in the centreline velocity plot, appears to coincide with an increase in the rate of jet spreading.

2.4.1 Assessment of Numerical Tests

Regarding variations with time-step, all the results presented here would seem to suggest that 100 time steps per cycle and perhaps even less, are adequate for a time-converged solution. This leaves the matter of grid convergence.

For the exit profiles (figure 2.5), given that their grid densities are not hugely dissimilar, the difference between the medium and coarse grid probably owes more to

the different distributions across the exit plane; especially at the edges. Comparison of normalised data with the fine grid is only valid whilst these show the same symmetric behaviour. It is seen that the jet flow developed using a fine grid does not remain symmetrical about the actuator centre line. The instability causing flow asymmetry is first apparent some distance downstream of the actuator. Initial vortex pairs slow almost to a halt and are impacted by succeeding pairs. On coarse grids the initial pairs are quickly dissipated and merge with those that follow. On finer grids, successive pairs struggle against each other; this unstable behaviour then propagates back towards the exit.

The mean exit profile calculated on the fine grid after six cycles (figure 2.5) has significantly greater (negative) velocity peaks at the edges of the nozzle, and a fuller profile at the centre. Net mass flow appears close to zero. To mitigate the discrepancies between the fine grid exit profile and the profiles calculated on the other grids, it must be emphasised that coarse and medium results have been taken over an interval when the exterior flow is settled over a large region of the domain. Fine grid averages have been obtained at a time when there may be significant cycle to cycle differences close to the exit. In identifying the trend of mean suction at the nozzle edges and blowing at the centre, the solutions agree well.

Normalised profiles of mean streamwise velocity (figures 2.7, 2.8 and 2.9) are similar on medium and coarse grids, testifying to the self-similarity of the jet flows. This is especially true close to the jet centre. Fine grid results can only be compared whilst these display reasonable symmetry. At $y/h = 9.8$ after six cycles, there is good agreement. There is some discrepancy between streamwise velocity results at the jet edges. This has no discernible trend with downstream distance. However, the data are normalised by the jet half-width b, which has been calculated as an average of half-width either side of the jet centre. If the jet is not perfectly symmetric this represents a compromise value, the effect of which increases outward from the centre.

The normalised profiles are dependent on the normalising coefficients, V_{cl} and b. There is good qualitative agreement between medium and coarse grids for V_{cl} versus y. The same trends are apparent, although coarse grid velocities are generally lower and after attaining peak velocity, the decay is greater. The jet half-width b, increases linearly except at the jet front where spreading is greater.

In summary, the numerical tests have demonstrated time-step convergence when using the medium grid. Grid convergence was shown for regions close to the actuator exit but only for an interval six cycles after actuation was commenced. The development of flow asymmetry thereafter for calculations on the fine grid meant that results sets could no longer be compared.

2.5 Formation of the Jet

The process by which a synthetic jet forms is illustrated in figure 2.11. The four rows show the first four cycles after actuation commences. During the blowing part of the cycle, counter rotating vortices are formed at the corners of the nozzle exit. These are convected downstream under the influence of fluid still being ejected. Their motion is slowed during the suction schedule since there is no new momentum addition in the streamwise direction and entrainment of ambient fluid by the escaping vortices means that momentum is spread over an ever increasing fluid mass.

The atmosphere surrounding the actuator exit is no longer at rest when the second system of counter rotating vortices is developed (second row in figure 2.11). Travelling in the wake of the first, these catch up with the, by now almost stationary, initial vortex system. The second set of vortices is still travelling relatively quickly when the two systems meet. These begin to merge, forming a single system moving with a slow common velocity. Entrainment of ambient fluid however, means a continual deceleration.

The process is then repeated for further cycles. Successive vortex pairs travel in the wake of the previous pair until impacting and merging with a downstream system which has had contributions from all previous cycles. After several cycles, this system is considerably smeared and is far enough removed from the exit that the latest vortices from the actuator are travelling only slowly at impact. Viscous losses mean that ultimately a balance is reached and the momentum introduced is insufficient to move the summed vortical system. This then becomes stationary some distance from the exit (bottom row in figure 2.11).

2.6 Comparison with Published Data

The synthetic jets of Smith and Glezer[63], Kral et al.[65], Mallinson et al.[67], and Rizzetta et al.[66] are described as symmetric. The criteria established and used in these papers to discuss synthetic jet behaviour therefore only relates to jet flows whose peak streamwise velocity coincides with the geometric centreline. It was observed in section 2.4 that results obtained on a fine grid were asymmetric. It was hypothesised in section 2.4 that artificial dissipation of vortices may mean that results generated on relatively coarse grids better represent the process by which a synthetic jet forms. For comparison with published data, the computational results are those calculated on the medium grid and are from the tenth actuator cycle.

2.6.1 Actuator Exit Velocity

The streamwise velocity (v) at the actuator exit plane, averaged over a complete cycle, is plotted on the left side of figure 2.12. The plot on the right shows profiles at two instants half a cycle apart. In figure 2.12, peak to peak *mean* values are seen to be an order of magnitude lower than velocity values at some instants of the actuator cycle. The profiles show both qualitative and quantitative agreement with the result of Rizzetta et. al.[66]. As observed by these authors, there is a mean inflow (suction) at the actuator edges with mean blowing across the centre. Rizzetta et al.[66] and Mallinson et al.[67] placed some emphasis on the variation of the flow behavior with cavity geometry. Although current profiles were generated with a diaphragm type motion of the cavity floor, and the Rizzetta et al. results are from piston type motion, this difference does not appear to be significant.

2.6.2 Streamwise Velocity

Streamwise velocity profiles are plotted in figure 2.13 at streamwise distances of $y/h = 9.8$ and $y/h = 15.6$ from the jet exit plane. These demonstrate the self similarity of the resulting jet. For the plots of streamwise velocity shown, the profiles have been normalised with respect to the maximum centreline velocity and the jet half width, b, following references [65],[63] and [67]. The profiles are compared in the

figure, with those of Kral et al.[65]. In comparison with the experiments of Smith and Glezer [63], both Kral et al.[65] and Rizzetta et al.[66] found their computational results to have slightly higher velocities at the jet edges. Figure 2.13 shows that the current results have slightly lower edge velocities than Kral et al.[65].

2.6.3 Centreline Velocity Variation

The time variation of centreline velocity at a distance $y/h = 5.0$ downstream from the exit plane is shown on the left of figure 2.14. This is compared with that of Rizzetta et al [66]. Peak velocity values are lower than observed by these authors and there is less variation. The mean value is slightly greater however.

On the right of figure 2.14, the decay of mean centreline velocity with downstream distance is plotted. Comparison is made with the computational results of Kral et. al.[65], who claim good agreement with the experiments of Smith and Glezer[63]. The quantitative differences in figure 2.14 indicate that the current jet model has significantly lower jet spreading. Despite this, the broad trends found in the published results are replicated. The centreline velocity continues to increase to a distance of around $y/h = 10$. From this point on, there is a steady decay. Kral et al. claim to have run their computations for 27 cycles, which may explain the absence of the jet front in their plots. Also noted by Smith and Glezer[63], Kral et al. have a decay rate close to $v \propto y^{-\frac{1}{2}}$, which is characteristic of turbulent steady jets. It has already been pointed out that turbulence levels are low for the current results. Smith and Glezer[63] state that their nominal case appeared to remain laminar beyond $y/h = 8.5$. At large values of y/h however, the jet was turbulent and this needs to be reprepresented in the computations. Given that the velocity at any point is dependent on the velocity upstream, discrepancies between the cases grow in the downstream direction. The low spreading rate is verified in figure 2.15 which shows the jet half-width, b.

2.7 Summary

A synthetic jet model based on the deformation of a closed cavity was developed and the resulting flow behaviour compared with the existing literature.

Time-step resolution was evaluated and for the flow conditions considered, convergence was demonstrated for relatively large time-steps of $1/100^{th}$ of the actuation cycle. Grid resolution was also studied using grids described as fine, medium and coarse. Evaluation was made by considering mean velocity at the jet exit and at various downstream locations, the jet half-width, and the decay of centreline velocity.

The jet flow calculated on the fine grid was found to be asymmetrical. This behaviour is attributed to the combination of reduced numerical dissipation using this grid, and low turbulence production. The instability first becomes apparent a distance downstream of the actuator after a number of cycles. Over time, this moves back towards the actuator exit. The existing literature does not discuss asymmetric flows, and therefore fine grid results were only considered at a time and locations when they were broadly symmetric.

The behaviour close to the actuator, characterised by the exit profiles, streamwise profiles at $y/h = 9.8$, and centreline velocity indicates good agreement between solutions calculated on the different grids. Further downstream, the onset of asymmetry in fine grid solutions, and differences in jet spreading between medium and coarse, mean that agreement cannot be claimed. Downstream results on the medium and coarse grids do show the same qualitative behaviour however.

Results obtained on the medium grid were used to compare with the existing literature. Other authors[66][67] assert that the influence of cavity geometry may be considerable. The geometry chosen is that of Rizetta et al.[66]. The mode of deformation is slightly different to these authors however, with the cavity floor acting as a diaphragm rather than as a piston. The volume displacement is the same for each case. Despite the small difference, exit velocity profiles show good qualitative and quantitative agreement.

Normalised streamwise velocity profiles are also similar to published profiles. Previous computational results[65][66] have maintained slightly higher streamwise velocity

at the jet edges than seen in experimental[63] data. Current streamwise results lie between the two.

The jet centreline velocity and half width were also compared. There is reasonable agreement of jet centreline velocity close to the actuator exit. The computed value is always higher than that observed in previous computations or experiments however, and the plots diverge downstream. At the same time, the jet half-width increases at a rate which is lower than in the literature. Turbulence levels were low in the computed results, and the centreline velocity and jet half-width are instead consistent with a laminar rather than a turbulent jet. This causes no problem close to the actuator, it is known that transition to turbulence occurs some distance downstream of the actuator exit.

In the chapters which follow, the synthetic jet will be considered when operating in a turbulent boundary layer. It will be shown that flow normal to the wall is considerably restricted by the presence of a crossflow. In a crossflow, the features of significance exist close to the surface in which the actuator is embedded and the actuator has little influence at large distances normal to its exit plane.

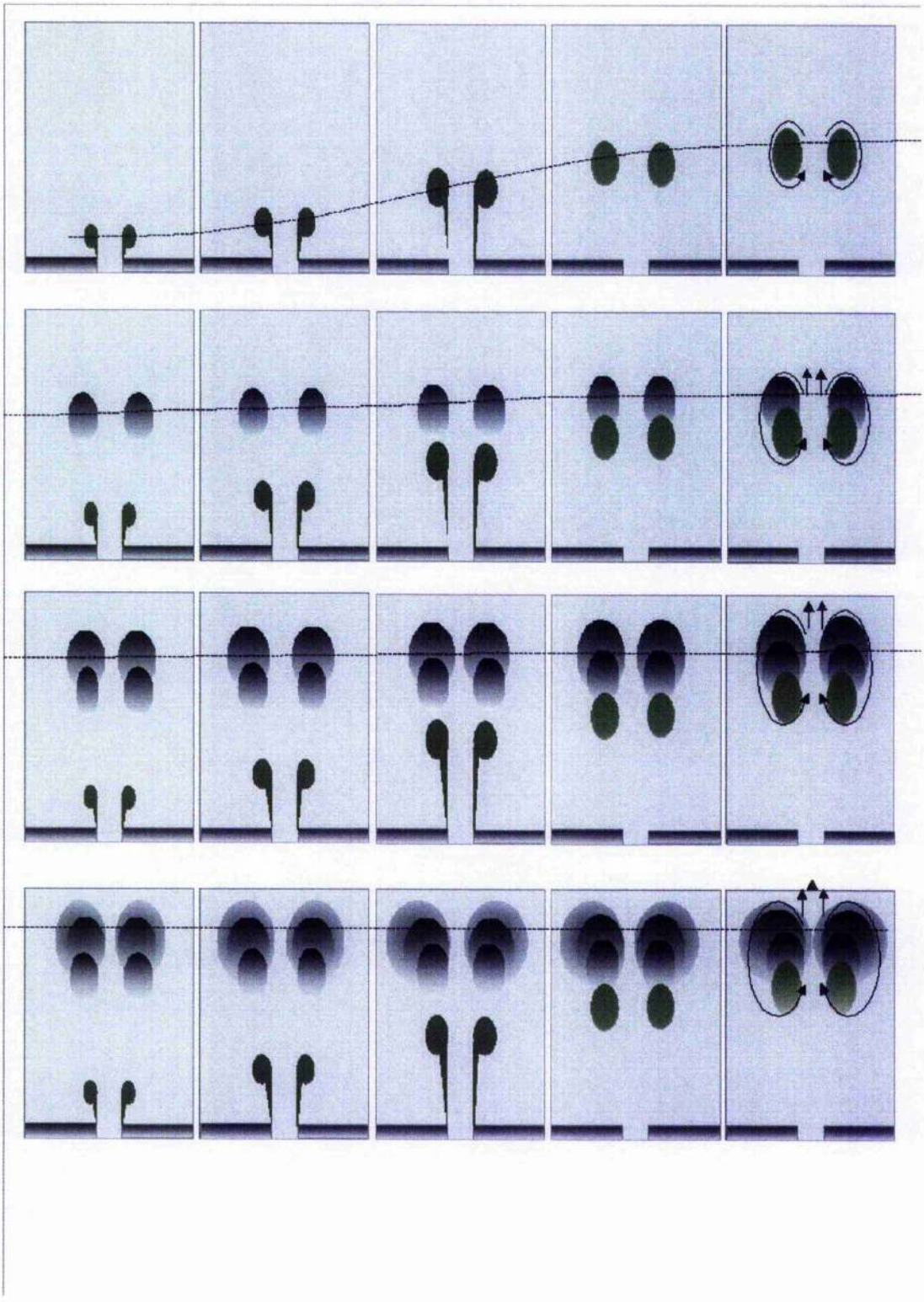

Figure 2.11: **Synthetic Jet Formation**, Five equally spaced instants (columns) of four synthetic jet cycles (rows) are shown, each blowing cycle produces a set of counter rotating vortices, the merging of which causes the formation of a jet flow.

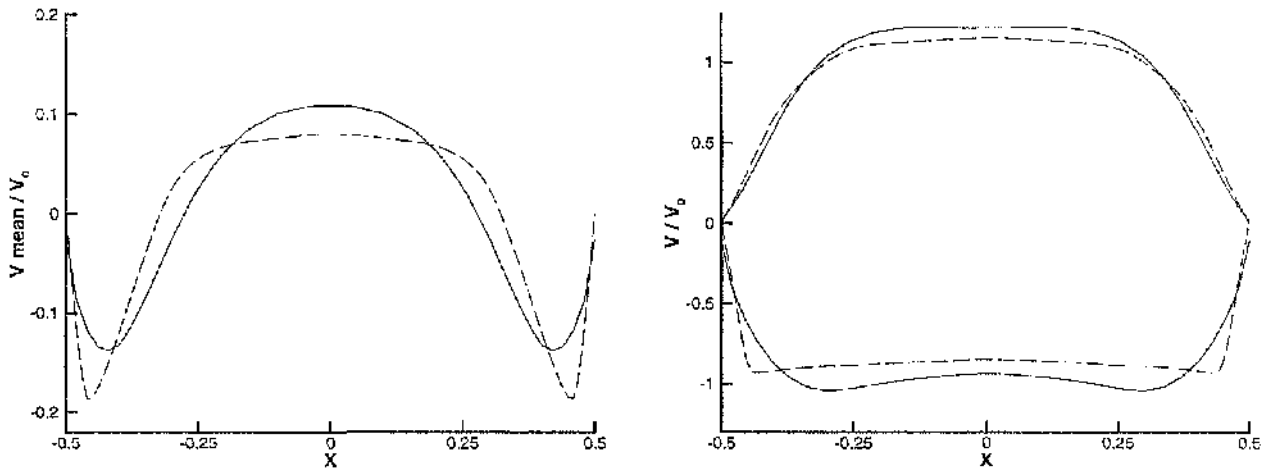

Figure 2.12: **Actuator Exit Profiles, left,** cycle averaged v velocity at the exit plane, dashed line indicates results of Rizzetta et. al.[66]; **right,** instantaneous exit profiles separated by a half cycle

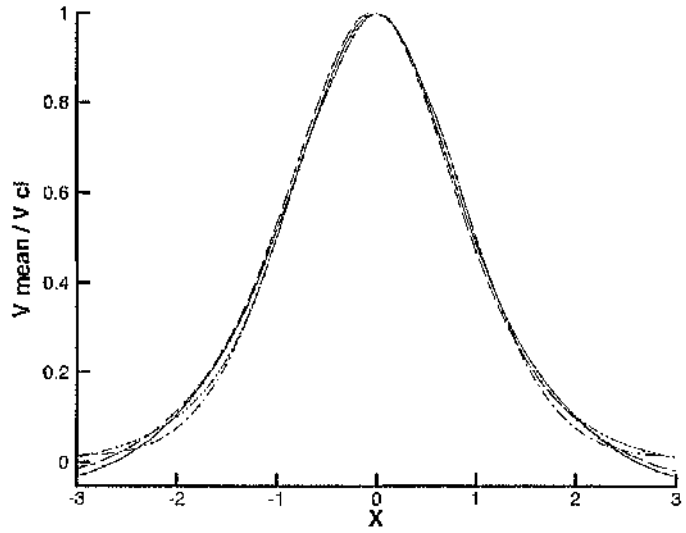

Figure 2.13: **Streamwise Mean Velocity Profiles**, cycle averaged v velocity at streamwise stations $y/h = 9.8$ (solid) and $y/h = 15.6$ (dashed), and comparison with Kral et. al[65] (dot-dash, dot-dot-dash)

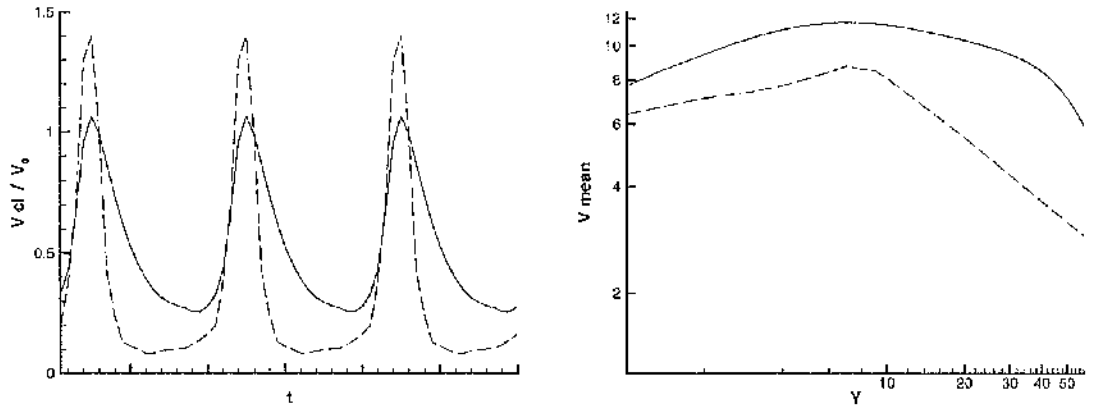

Figure 2.14: **Centreline Velocity, left,** solid line, variation with time at $y/h = 5.0$; dashed, Rizzetta et. al.[66]; **right,** solid line, variation of mean velocity with downstream distance; dashed, Kral et. al.(7), dotted line shows a jet decay rate proportional to $(y/h)^{1/2}$

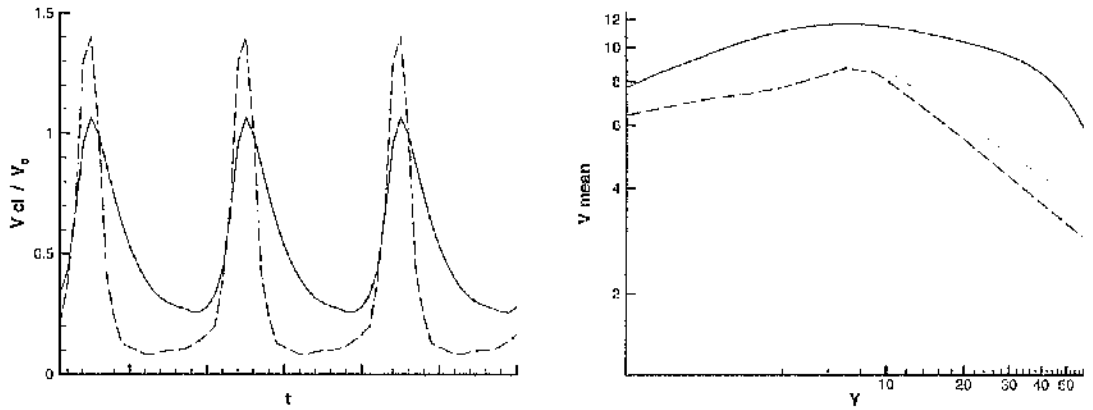

Figure 2.15: **Variation of Jet Half-Width,** b vs. y/h; dashed line, Kral et al.[65]. The comparison illustrates the low jet spreading of current results.

Chapter 3

The Synthetic Jet in Cross Flow

3.1 Overview

In the previous chapter, a synthetic jet was considered whilst operating in an initially still atmosphere. However, in practical applications a primary flow which requires to be controlled is usually involved. The simplest possible configuration which involves a primary flow and a synthetic jet actuator, has the actuator embedded in a flat plate which is aligned with the flow direction. In this chapter, a CFD model of this situation is developed. The deforming cavity which was used in the previous chapter is subjected to a crossflow. Deflections of the cavity floor are of similar magnitude as those used previously. The flow structures which develop through actuation, and the effect these have on the local surface pressure distribution are investigated.

This chapter also compares the deforming cavity model with another simpler model. The alternative approach simulates flow to and from the cavity by imposing a time-varying velocity profile at the actuator exit plane. The benefits of the simpler model are that in the absence of the cavity fewer grid points are required and the incorporation of synthetic jets in more complex geometries is simplified. The flow from a deforming cavity is likely to vary depending on the specific cavity design. Even for a (2-D) slot actuator there are a number of dimensions which may have a bearing on the exit velocity magnitude, profile, and time variation. These include nozzle exit width, cavity height, cavity width, and the mode and magnitude of diaphragm deflection. If it can be shown that an imposed velocity adequately represents the

flow from a deforming cavity then the cavity geometry can be described using only the nozzle exit width, h. This makes simpler the characterisation of control cause and effect, separating the control problem of how flow from the cavity exit affects the primary flow from that of actuator internal design.

3.2 Numerical Formulation

3.2.1 Simplified Actuator Model

Results obtained from a deforming cavity embedded in a flat plate set in crossflow, are compared with those from a simplified actuator model in order to validate the use of the latter, alternative approach. For the simplified model, the cavity and nozzle are removed and a velocity boundary condition is instead imposed at the nozzle exit plane ($y = 0$). The time varying exit velocity used to develop the current results is defined on an axis system having its origin at the upstream edge of the actuator exit,

$$v(x,t)_{y=0} = V_0 \sin^2(\pi x/h)\sin(\omega t) \quad \text{for} \quad 0 \leq x \leq h \tag{3.1}$$

3.2.2 Grids and Boundary Conditions

The grids used for the calculations are as shown in figure 3.1. The grid shown in the figure consists of 11 blocks including four blocks representing the cavity. The simulated actuator flow was imposed at the lower boundary of the middle exterior block (block 4). Across both the wall surfaces and the actuator exit plane, turbulent parameters were set as for a wall surface (defined in Appendix A). On the left and upper boundaries of the external grid, freestream conditions are applied. On the right (downstream) boundary, density and velocity are extrapolated linearly (1st order extrapolation) from the interior whilst the pressure is set at a constant *freestream* value. Of the lower boundaries, blocks 2, 3, 5 and 6 use wall surface conditions. The lower boundaries of the left and rightmost blocks (blocks 1 and 7) use *symmetry* boundary conditions, i.e. they are calculated as though the condition

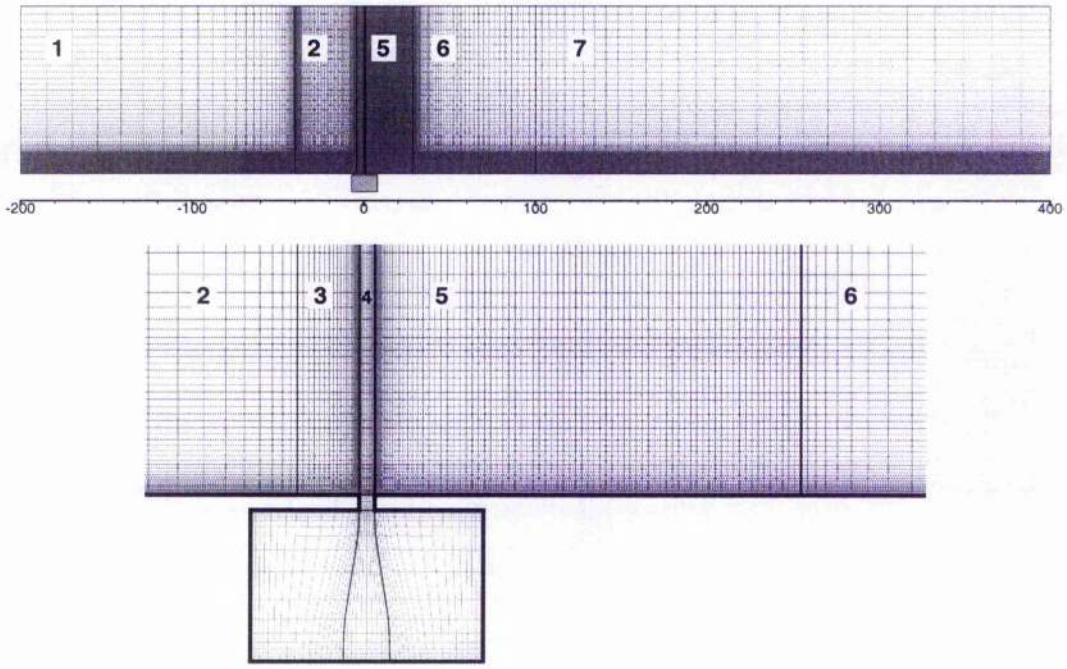

Figure 3.1: **Crossflow Grid, top:** A four block cavity is connected to seven exterior blocks. For cases where the flow from the actuator was represented by a time varying velocity boundary condition, the cavity was removed and the boundary condition applied across the nozzle exit plane. The flat plate in which the actuator is embedded is represented by the lower boundaries of blocks 2, 3, 5 and 6. **bottom:** Close up view of the cavity and the region of uniform spacing which extends downstream. Every third vertex is shown for clarity.

of the fluid immediately outside the domain is identical to that immediately inside. A mathematical description is given in Appendix A.

In anticipation that the oscillatory blowing cycle of the actuator would lead to the periodic production of organised structures which would then be convected in the direction of the crossflow, a region having uniform grid spacing, $\triangle_{IJ}$, is incorporated in the grid to minimise the artificial dissipation of such phenomena due to grid stretching. In the crossflow direction, mesh point spacing does not exceed $\triangle_{IJ}$ for a distance $5h$ upstream, and between $25h$ and $49h$ downstream of the jet exit. These dimensions were chosen so that travelling vortices remain within the uniformly

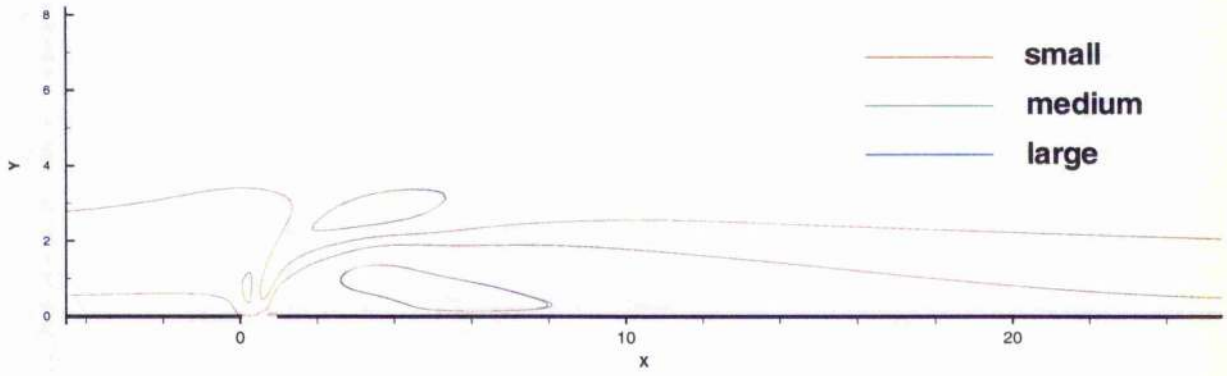

Figure 3.2: **Time Step and the Mean Velocity Field**, Contours of Velocity Magnitude; $Re_h = 350$, $k_h = 0.1\pi$, *red* line corresponds to time-step $\Delta t^\star = 0.025$; *green*, $\Delta t^\star = 0.05$; *blue*, $\Delta t^\star = 0.1$

spaced region for at least one actuator period, even for the fastest crossflow, lowest frequency cases (low k_h). Normal to the lower surface, mesh points are stretched out until the distance between consecutive points reaches the required $\triangle_{IJ}$, this value is then maintained until a distance of $6.5h$ from the bottom edge before stretching again resumes.

3.3 Numerical Tests

3.3.1 Time Step Study

It is necessary to demonstrate that a sufficiently small time-step is being used to follow the evolution of the flow. To do this three cases were run at reduced frequency of $k_h = 0.1\pi$; each case using a different time-step. The time steps used were $\Delta t^\star = 0.1$, $\Delta t^\star = 0.05$ and $\Delta t^\star = 0.025$, corresponding to 100, 200 and 400 steps per cycle. The Reynolds number was $Re_h = 350$ and the Mach number $M = 0.1$. The grid used had a region of medium uniform spacing, $\triangle_{IJ} = 0.1h$. The actuator was modelled a distance of $200h$ from the leading edge.

Contours of velocity magnitude averaged over the tenth cycle are shown in figure 3.2. These are generally overlaid, except for certain parts of the domain where the use of the largest time-step give a small variation.

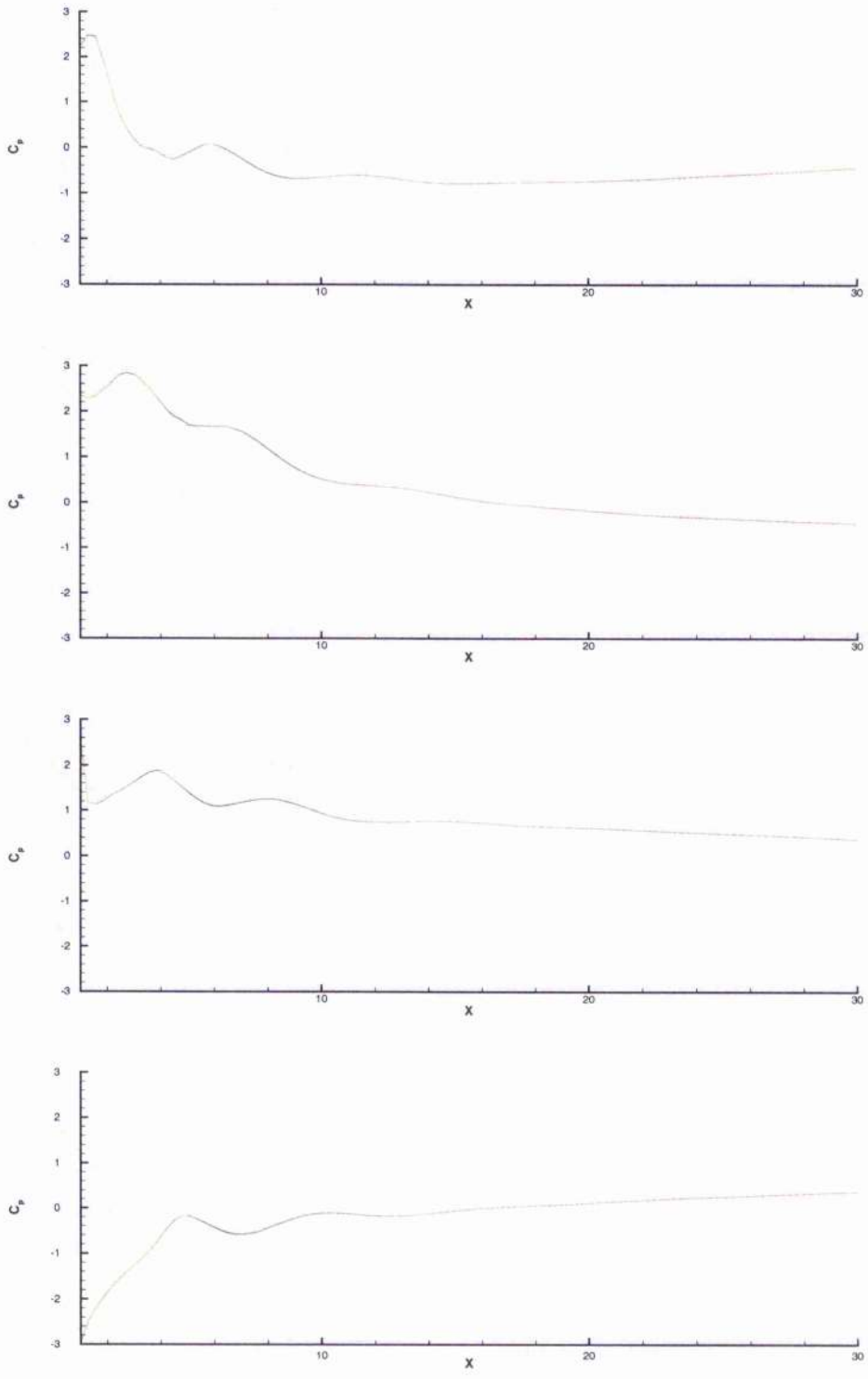

Figure 3.3: **Time Step and the Downstream Pressure Distribution**, Surface pressure is shown at four instants of the cycle; $Re_h = 350$, $k_h = 0.1\pi$, *red* line corresponds to time-step $\Delta t^\star = 0.025$; *green*, $\Delta t^\star = 0.05$; *blue*, $\Delta t^\star = 0.1$

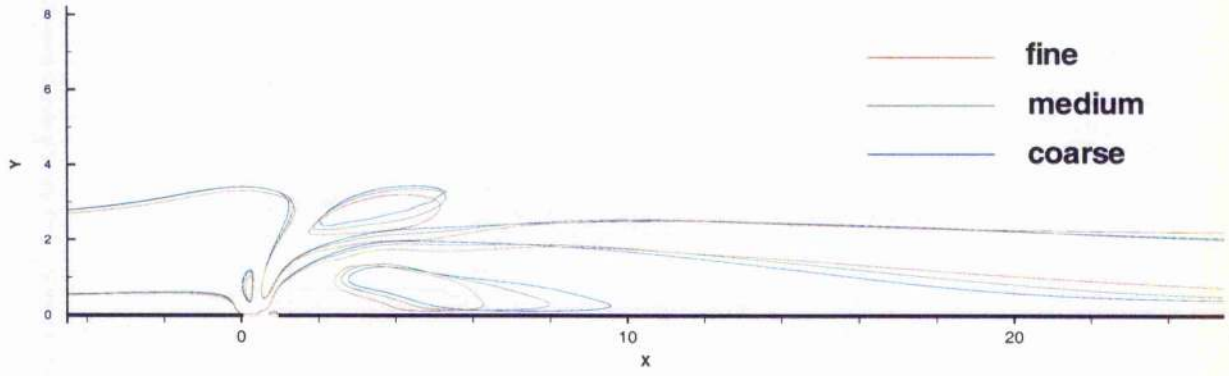

Figure 3.4: **Grid Density and the Mean Velocity Field**, Contours of Velocity Magnitude, $Re_h = 350$, $k_h = 0.1\pi$, *red* line corresponds to grid having $\triangle_{IJ} = 0.1h$; *green*, $\delta = 0.2h$; *blue*, $\delta = 0.3h$

Similar duplication of pressure distribution is demonstrated for four instants of the tenth cycle in figure 3.3.

3.3.2 Grid Dependence

The grids used for this study include a region at least $25h$ x $6.5h$, of uniform spacing ($\triangle_{IJ}$), beginning $5h$ upstream of the actuator block. Since the location of any coherent flow structures introduced into the crossflow may change with time, and since the gradients which these impose on the solution variables cannot be confidently judged in advance, this region has the purpose of preserving the solution quality over an extended region.

To gauge the effect that the exact value of $\triangle_{IJ}$ might have, cases were run on grids similar to that illustrated earlier (figure 3.1). Three different uniform spacings were used, a coarse spacing of $\triangle_{IJ} = 0.3$, a medium spacing of $\triangle_{IJ} = 0.2$ and a fine spacing of $\triangle_{IJ} = 0.1$. The block representing the actuator exit is positioned 200 exit widths downstream from the plate's leading edge. Cases were run at $Re_h = 350$ and $M = 0.1$. A reduced operating frequency of $k_h = 0.1\pi$ was used.

Figure 3.4 shows contours of velocity magnitude averaged over the tenth cycle after actuation commences. The contours are generally evenly spaced between coarse, medium and fine cases. The medium spaced region has a grid density 4 times that

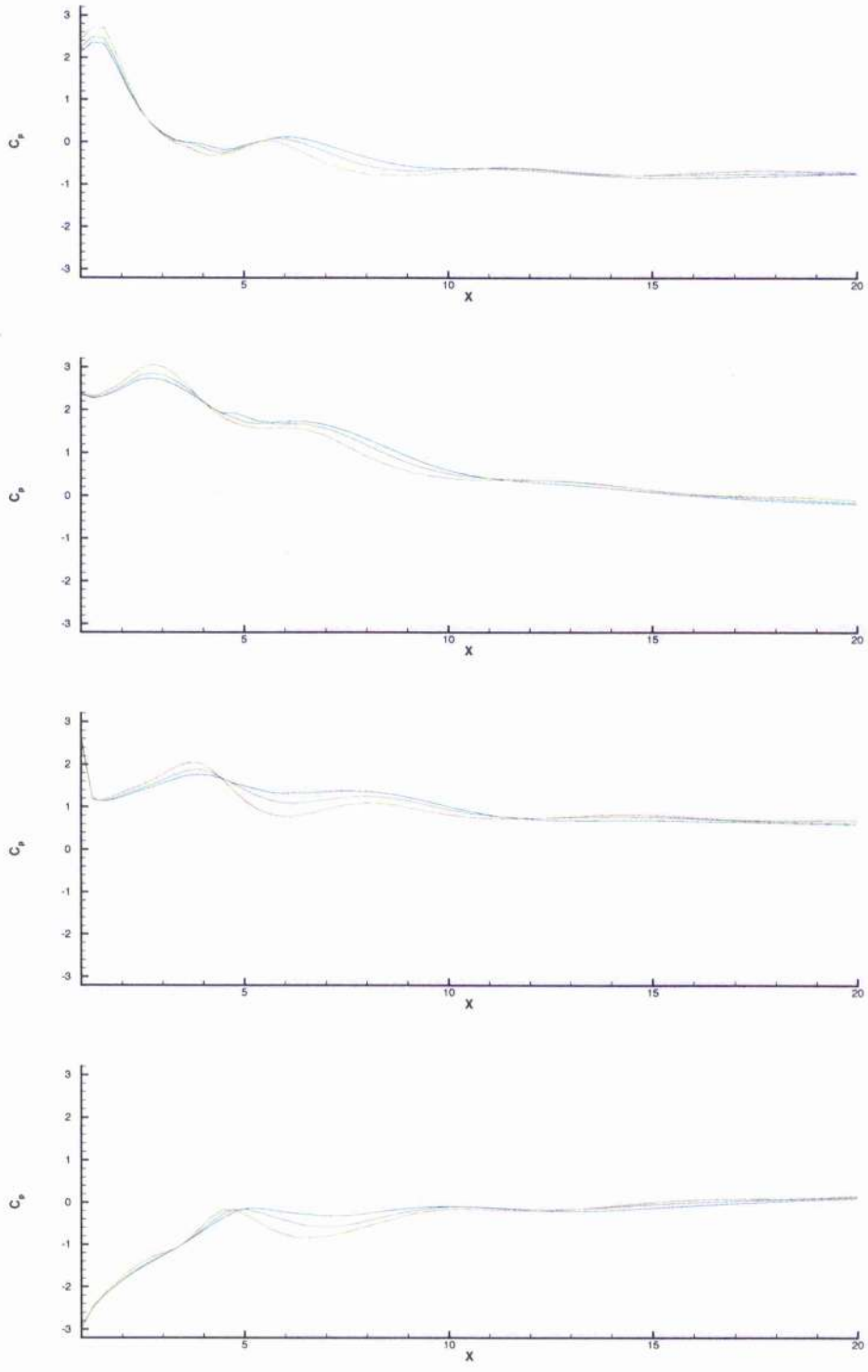

Figure 3.5: **Grid Density and the Downstream Pressure Distribution**, Surface pressure is shown at four instants of the cycle; $Re_h = 350$, $k = 0.1\pi$, *red* line corresponds to a grid having $\triangle_{IJ} = 0.1h$; *green*, $\triangle_{IJ} = 0.2h$; *blue*, $\triangle_{IJ} = 0.3h$

of the coarse, and the fine grid 9 times that of the coarse. The spacing between contours is therefore reducing with increasing grid density.

Favourably affecting the pressure on the surface is the main purpose of flow control for the current application. The effect on the surface pressure coefficient, C_p, is shown in figure 3.5 at four instants on the tenth cycle.

3.4 Results

To demonstrate the validity of imposing a velocity boundary condition to represent the flow generated by a deforming cavity, equivalent cases using both methods are required. In order to achieve this equivalence, the following approach was taken,

Deforming cavity cases were first calculated. Each of these used a unique combination of reduced frequency, and distance from the leading edge, x_{le}. The exit flow rate for each case was then calculated at intervals of the cycle and corresponding sinusoidal velocity boundary conditions were set attempting to match the flow rate from the cavity exit. Table 3.1 lists the cases which were calculated.

For each of the deforming cavity cases, the peak cavity floor deflection was set at $A = 0.698h$. This standard deformation gives different mass flow from the actuator when it is operating in different conditions.

For a known deflection, the mass flow rate is easily calculated if the fluid is incompressible. In this event, with reference to figure 2.2, the volume displaced (per unit span) by the diaphragm when deflected through A is given by,

$$\mathcal{V} = 0.75\ q\ A\ \sin(\omega t) \tag{3.2}$$

where $q = 15h$ is the length of the cavity floor and the instantaneous peak floor deflection is $Asin(\omega t)$. The non-dimensional volume flow rate from the nozzle is equal to the rate of volume displaced by the diaphragm,

$$\dot{\mathcal{V}}^*_{exit} = \dot{\mathcal{V}}^*_A = \frac{3q^*\ A^*\ k_h}{2}\ cos(2kt^*) \tag{3.3}$$

which has a maximum value of $3q^*A^*k_h/2$.

CASE	ACTUATION	α / V_0	k	x_{lc}
1a	deforming cavity	$\alpha = 0.698$	0.025π	$200h$
1b	imposed velocity	$V_0 = 2.42$	0.025π	$200h$
2a	deforming cavity	$\alpha = 0.698$	0.125π	$200h$
2b	imposed velocity	$V_0 = 5.0$	0.125π	$200h$
3a	deforming cavity	$\alpha = 0.698$	0.125π	$100h$
3b	imposed velocity	$V_0 = 5.0$	0.125π	$100h$
4a	deforming cavity	$\alpha = 0.698$	0.16π	$40h$
4b	imposed velocity	$V_0 = 4.5$	0.16π	$40h$
5a	deforming cavity	$\alpha = 0.698$	0.16π	$100h$
5b	imposed velocity	$V_0 = 4.5$	0.16π	$100h$
6a	deforming cavity	$\alpha = 0.698$	0.2π	$100h$
6b	imposed velocity	$V_0 = 3.8$	0.2π	$100h$
7a	deforming cavity	$\alpha = 0.698$	0.16π	$200h$
7b	imposed velocity	$V_0 = 4.5$	0.16π	$200h$

Table 3.1: Actuator in Crossflow Cases

For current cases, $k_h = 0.025\pi$, 0.125π, 0.16π and 0.2π. Since A, h and q are constant, corresponding peak incompressible mass flow rates would be 1.23, 6.17, 7.89 and 9.87 respectively.

For the synthetic jet model that has been developed, it is clear (see for example figure 2.3) that the volume displaced by the deforming cavity floor is small relative to the total volume of the cavity. Since the fluid is not actually incompressible this introduces differences in magnitude and phase of volume displacement between the cavity floor and nozzle exit, i.e. the compression or rarefaction caused by the cavity floor motion is not simultaneously manifested as an identical volume displacement at the actuator exit. This makes it difficult to predict the flow from the cavity in advance.

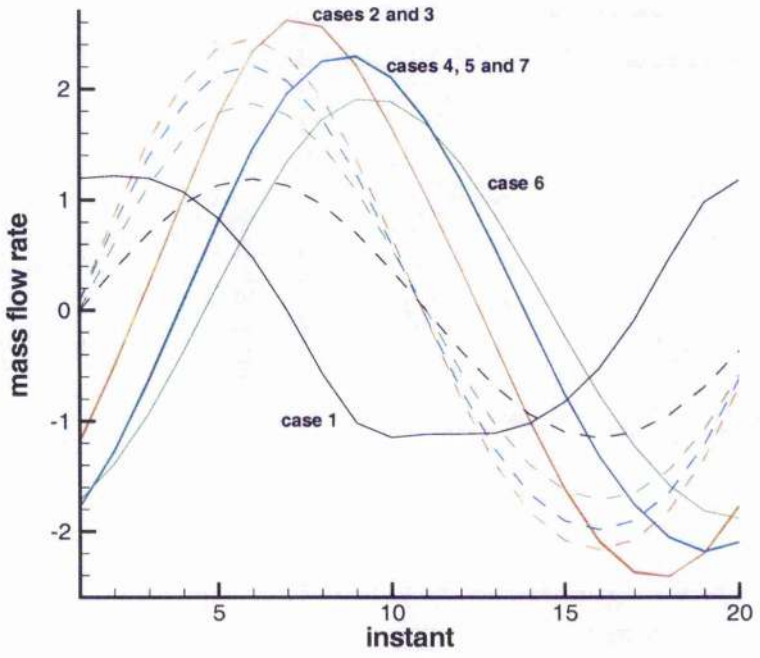

Figure 3.6: **Evaluation of Mass Flow Rates**The massflow rate is shown for each case. Rates for cases sharing the same reduced frequency overlap. In all cases the plots approximate a sine wave. For cavity cases (solid lines), $t^\star = 0$ corresponds to the point where the cavity floor has returned to its initial undeformed position whilst travelling upwards. For imposed velocity cases (dashed lines), $v_{exit}(t^\star = 0) = 0$ at the beginning of the blowing schedule.

3.4.1 Mass Flow Rate

Figure 3.6 indicates the fluid mass crossing the nozzle exit plane for cases 1-7. Mass flow rate has been calculated at 20 instants of the operating cycle each separated by an equal interval, $T/20$. This is achieved by averaging over each cell and then summing according to,

$$\dot{m}_{exit} = \sum_{i=2}^{N} (\frac{\rho_i + \rho_{i-1}}{2})(\frac{v_i + v_{i-1}}{2})(x_i - x_{i-1}) \tag{3.4}$$

where index i indicates the grid node and N the number of nodes across the actuator exit.

Figure 3.6 shows that the mass flow rate varies approximately sinusoidally in time for all cases. Suction during case 1 gives the greatest exception. The deforming cavity cases have peak mass flow rates, $\dot{m}_0$, of approximately $\dot{m}_0 = 1.21$, 1.9, 2.25 or 2.5. It can be seen that the peak mass flow varies depending on the reduced frequency, the four values above corresponding to one of the frequencies, $k_h = 0.025\pi$, $k_h = 0.125\pi$, 0.16π or 0.2π which were used. To emulate the mass flow behaviour using a velocity boundary condition, the exit velocities were set making the assumption that the fluid density at the exit is equal to that of the freestream, i.e. $\rho_{jet} = \rho_\infty$, and therefore,

$$\dot{m}_{exit} = \dot{m}_0 \ sin(\omega t) \tag{3.5}$$

Using the sine squared velocity profile given in equation 3.1, the peak exit velocity is set as

$$V_0/U_\infty = 2\dot{m}_0^* \tag{3.6}$$

giving $V_0/U_\infty = 2.42$, 3.8, 4.5 and 5.0.

On the actual boundary representing the jet exit however, the density is in fact calculated as part of the solution. The effect of the exit density assumption can therefore be assessed by comparing the actual mass flow rates achieved against the rates implied by the $\rho_{jet} = \rho_\infty$ assumption (which are $\dot{m}_{exit} = 1.21$, 1.9, 2.25 or 2.5). Peak rates are only slightly lower in all cases.

It was briefly mentioned that figure 3.6 demonstrates the dependence of mass flow rate on reduced frequency, k_h. It can be seen in figure 3.6 that the instantaneous mass flow rate from a deforming cavity is reduced when the reduced frequency k_h, is increased. This is contrary to the incompressible analysis of equation 3.3, which gives $\dot{m} \propto k_h$.

The computational experiments in this section only differ in reduced frequency and the actuator location. The exact overlapping of results for cases 2 and 3, and cases 4, 5 and 7, having the same reduced frequency strongly asserts that the mass flow rate is entirely independent of the actuator location, and therefore of the nominal exterior boundary layer. This is consistent with the incompressible flow behaviour, $\dot{m} = f(k_h, \alpha)$.

As well as a variation in the mass flow depending on the reduced frequency, deforming cavity cases also show a difference in phase. These all begin with the cavity floor in the flat undeformed position and moving upwards, corresponding to the maximum rate of volume displacement. The incompressible flow condition represents the theoretical limit, producing no phase lag between maximum volume displacement by the diaphragm and maximum mass flow rate at the nozzle exit. From figure 3.6, it can be seen that case 1a, which has a relatively low reduced frequency ($k_h = 0.025\pi$), closely approximates this behaviour. Otherwise the deforming cavity results in figure 3.6 have a considerable phase difference. This appears as a phase lead of up to almost half a cycle (180^o) in figure 3.6. The phase may also be considered as a lag of greater than 180^o and will be discussed as such in this chapter. The phase lag is greatest for cases 2 and 3 ($k_h = 0.125\pi$), and excepting case 1a, falls consistently with increasing reduced frequency and decreasing peak mass flow rate.

3.4.2 Exit Velocity Profiles

Exit velocity profiles for cases 3, 5 and 6 are shown on the left of figure 3.7. Profiles for cases 1, 2 and 7 are shown on the right. These are given for five equally spaced instants during actuation.

Figure 3.6 implies that the velocity varies periodically and with a phase difference between cases. Different velocity magnitudes can also be expected, corresponding

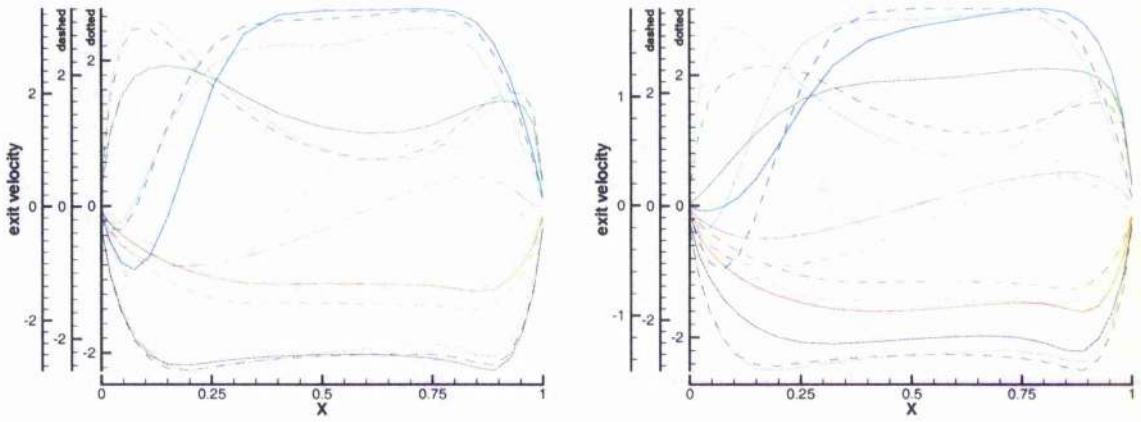

Figure 3.7: **Actuator Exit Profiles, Variation with Reduced Frequency**, **Left:** $x_{le} = 100h$, **solid** case3a, **dashed** case 5a, **dotted** case 6a, **Right:** $x_{le} = 200h$ **solid** case1a, **dashed** case 2a, **dotted** case 7a, Given the phase difference in terms of mass flow rate, the results above suggest that the exit velocity profiles are reasonably independent of the reduced frequency, k.

to the variation in mass flow rate. Besides magnitude and phase, the exit velocity, $v = v(x,t)$, is characterised by a spatial profile at each instant.

Reference to figure 3.6 shows that a phase difference exists between cases having different reduced frequencies. For the cases considered, data has been obtained at intervals which are 1/20th of the actuation cycle, i.e. $T/20$. Considering figure 3.6, $T/20$ is approximate to the phase interval between case 3a and case 5a and between case 5a and case 6a. With this in mind, the profiles for case 3a shown in figure 3.7 are obtained at time t, when the diaphragm has returned to the undeformed state whilst moving upwards, and then at $t+nT/20$, where $n = 4$, 8, 12 and 16. Profiles for cases 5a and 6a are taken at $t + (n+1)T/20$ and $t + (n+2)T/20$ respectively, to account for the difference in phase. For these, $n = 0$, 4, 8, 12 and 16. To demonstrate the similarity between profiles whilst accounting for the different massflow rate of each case, three velocity axes are used. On the right of figure 3.7, results are similarly treated. Normalised in the manner described, the profile shapes are similar. Once again emphasizing that the difference in phase is only approximately accounted for, these results suggest that over the range of reduced frequency considered, the

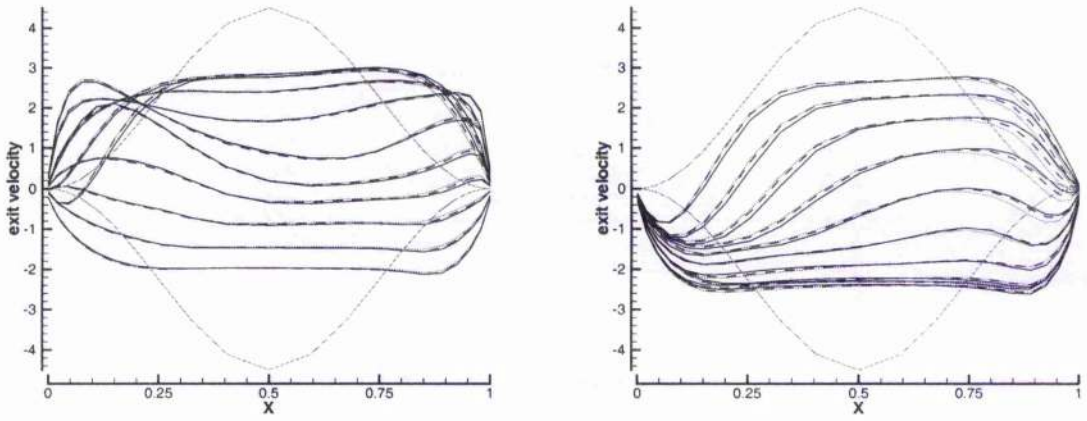

Figure 3.8: **Actuator Exit Profiles, Variation with x_{le}, Left:** Actuation through the first half of the cycle, i.e. late suction through peak blowing stages, **solid** , case 4a; **dashed** , case 5a; **dotted** , case 7a, **Right:** Actuation through the first half of the cycle, i.e. late blowing and through peak suction, **solid** , case 4a; **dashed** , case 5a; **dotted** , case 7a. The above profiles demonstrate that the shape, magnitude and phase of exit velocity profiles are independent of x_{le}. Extreme profiles for the imposed 'sine squared' velocity boundary condition are included for comparison.

instantaneous profile shape is reasonably independent of the reduced frequency.

The dependence of exit profiles on x_{le}, hence on the boundary layer thickness, δ, is examined in figure 3.8. Profiles for cases 4a, 5a and 7a, which have actuation at the same reduced frequency, $k_h = 0.16$, are plotted at 20 instants of the cycle. It was established in figure 3.7 that the profile shape is independent of the reduced frequency k_h. In figure 3.8 profiles are identical, matching not only in terms of their shape, but also in magnitude and phase. This is consistent with results shown for the time variation of mass flow rate in figure 3.6, which gives overlapping plots for cases having the same reduced frequency. Figure 3.8 is conclusive that the magnitude, shape and phase of exit profiles is independent of x_{le}.

On the left of figure 3.8, profiles corresponding to the first half of the cycle (shown in figure 3.6) are plotted. This begins just after peak suction. During the suction part of the cycle, i.e. where $\int v\,dx < 0$, the profiles are approximately symmetric about the centre of the nozzle exit. In the late stages of suction and the early stages of blowing, the velocities are greater towards the upstream side of the exit and have a minimum downstream of the centre. Close to peak blowing, the profile fills out downstream of the centre to remove the inflection. The plot on the right of figure 3.8 begins shortly after peak blowing. The full profile has begun to collapse close to the upstream nozzle edge. This process continues throughout the remainder of the blowing. There is already a net suction before a similar collapse can be seen close to the downstream edge. This leaves the centre region having the lowest suction velocity. The profile again fills out to produce approximate symmetry around peak suction.

The profiles developed from the deforming cavity are at all times different from the profiles imposed in their massflow-equivalent velocity boundary condition cases. The cavity never produces the same extremes of velocity as the velocity boundary condition and during blowing, the massflow is biased towards the downstream side of the exit rather than being evenly distributed about the centre.

For velocity boundary condition cases, the crossflow (u) velocity over the actuator exit is maintained at a constant value of zero. Actual U velocity profiles calculated using the deforming cavity are shown in figure 3.9. These are from cases 4a, 5a

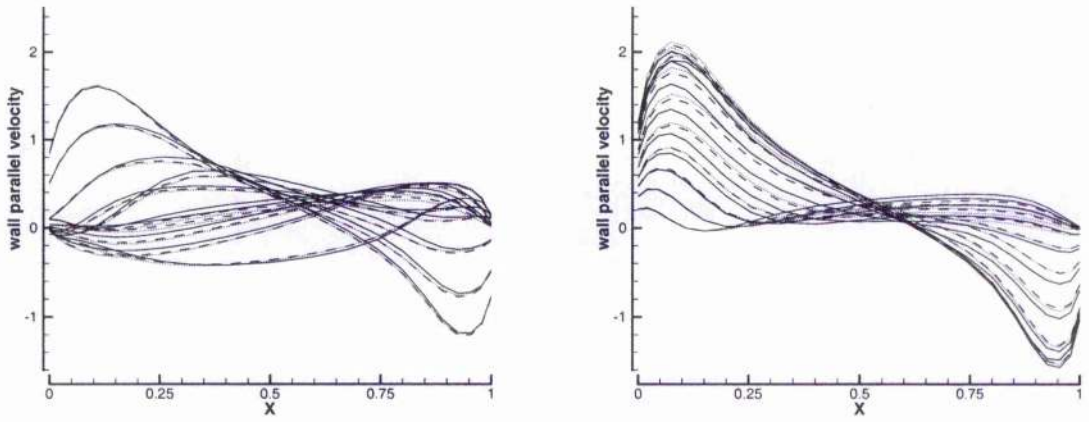

Figure 3.9: **Actuator Exit Profiles, 'U' Velocity, Left:** late suction through peak blowing, **solid,** case 4a; **dashed,** case5a; **dotted,** case7a, **Right:** late blowing and through peak suction.

and 7a and correspond to the exit-normal (v) profiles shown in figure 3.8. Similar results were obtained for the other cases. During suction and early blowing, the flow is towards the centre of the actuator. This causes local crossflow speeds to exceed the freestream speed ($u/U_\infty = 1$). Upstream and downstream peaks are of similar scale indicating that at the exit plane the freestream velocity has little direct influence.

3.4.3 Mean Flow Behaviour and Surface Pressure Effects

Figures 3.10 to 3.16 are plots of the cycle averaged flow. These show unit vectors indicating mean flow direction, overlayed on colour contours of velocity magnitude. Corresponding graphs of mean pressure coefficient C_p, along the flat plate surface are also included. Correlation between the mean flow field behaviour and surface pressures is apparent for each figure. Where the flow is generally away from the surface, the pressure reduces, and when it is towards the surface, it is increased. The magnitude of this effect depends on the velocity magnitude. The effectiveness of a synthetic jet actuator therefore depends on its ability to influence both the local flow direction and velocity magnitude. In each of the cases considered in this section, actuation reduces the local surface pressures.

Figure 3.10, compares the flow field and pressure results of cases 1a and 1b. There is close agreement between the cavity generated flow (1a) and that produced by imposing a velocity boundary condition (1b). There is a mean rotational flow at the downstream edge of the exit and then another larger region of mean rotation downstream. These effects are associated with a mean reduction in the local surface pressure. Although other comparisons between cavity generated and velocity boundary condition cases are not generally so close, there is qualitative agreement between a number of the plots shown in figures 3.11 to 3.16. Cases 2b, 5a, 5b, 6a, 6b, 7a and 7b all show a dominant region of mean rotation. Between these cases, the main differences are in the scale of the apparent mean recirculating region. This is illustrated by figure 3.17, where surface pressure plots from cases 5, 6a and 7a developed using a deforming cavity are compared with their counterparts 5b, 6b, and 7b which have been developed using an imposed velocity boundary condition. The data have been plotted using two different scales for the pressure axes. The similarity of the plots for these cases indicates that the same flow behaviour is being exhibited regardless of the means by which the actuation is being applied. Based on figures 3.11-3.13, the same cannot be said of cases 2-4. For these, there are considerable differences both in flowfield characteristics and in surface pressure distribution, depending on the actuation.

It is emphasized that figures 3.10-3.16 show mean flow behaviour and that the presence of an apparent mean structure at a location does not necessarily indicate a permanently established structure. Figures 3.18 to 3.24 show contours of vorticity for each case at five equally spaced instants of the cycle. Since four different reduced frequencies are used, the figures relate to cycles of different time duration. Case 1 ($k_h = 0.025\pi$) has an actuation period of $T^* = 40$, cases 2 and 3 ($k_h = 0.125\pi$) have a period of $T^* = 8$, cases 4,5 and 6 ($k_h = 0.16\pi$) have a period $T^* = 6.25$, and case 7 has a period of $T^* = 5$. The actuation period correlates with the distance travelled by fluid moving at the freestream velocity allowing rates of convection to be considered. Corresponding deforming cavity and imposed velocity results are shown side by side in the figures. These are sequenced to take account of the phase difference identified in figure 3.6, i.e. blowing and suction events are synchronised to the nearest $T/20$.

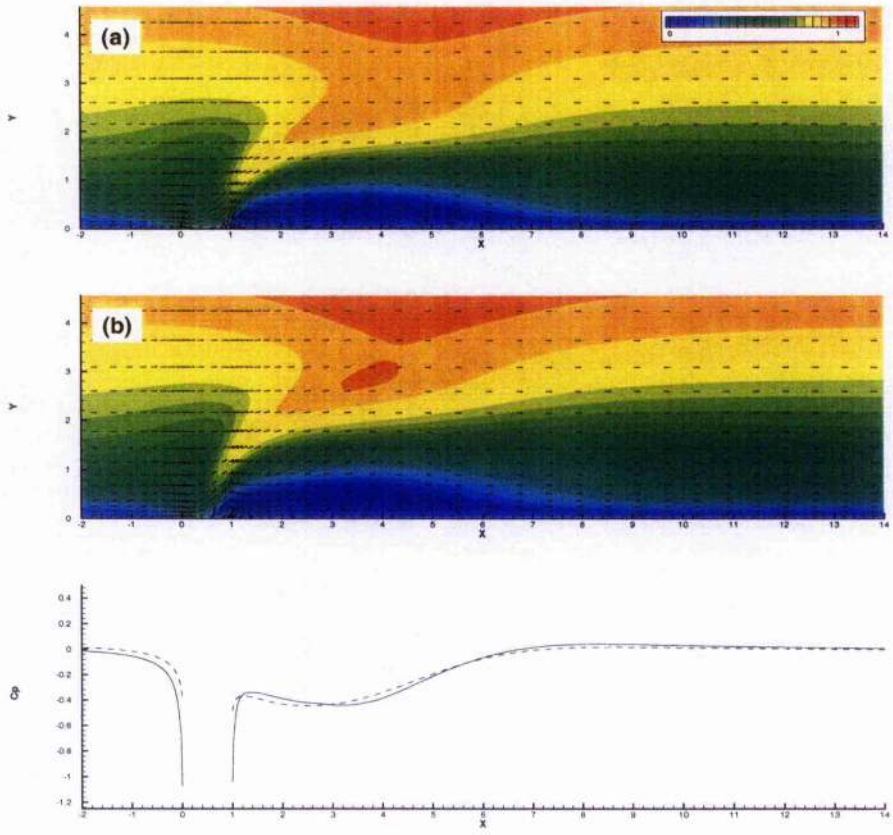

Figure 3.10: **Mean Flow Velocities and Surface Pressures, Case 1**
top and middle: Cases 1a and 1b respectively, colour contours show velocity magnitudes in the vicinity of the actuator, unit vectors indicate the flow direction. **bottom:** reduced surface pressures are associated with regions of mean recirculating flow, **solid,** case 1a; **dashed,** case 1b. A mean recirculating region can be seen in each of the vector plots. Mean pressure distribution is similar regardless of whether the jet flow is from a deforming cavity or by a time varying velocity boundary condition.

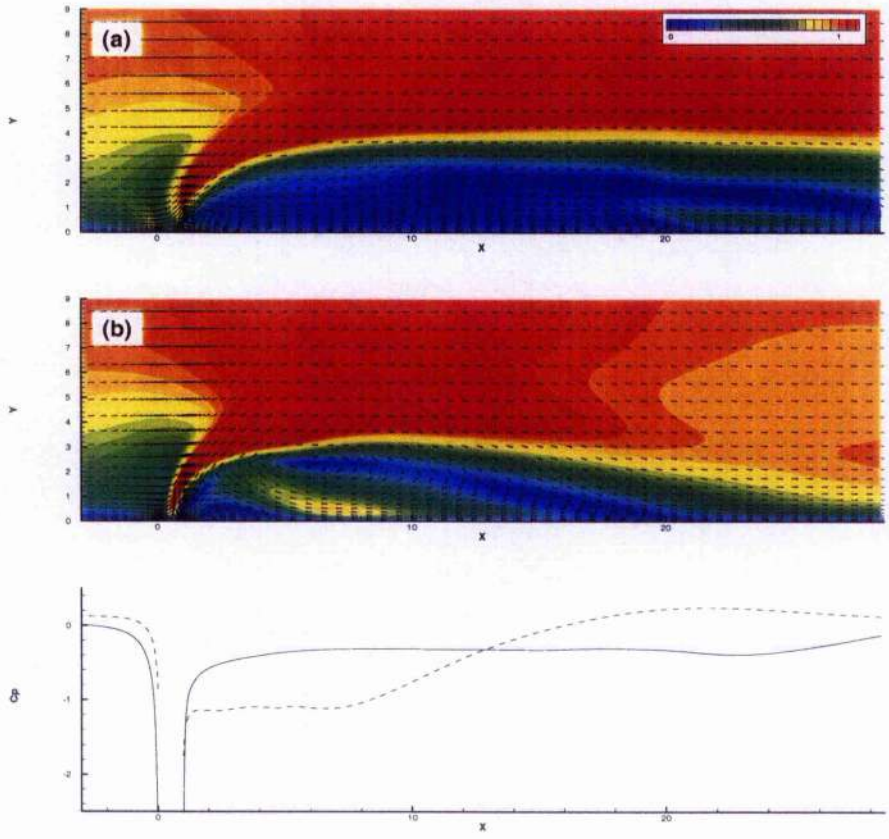

Figure 3.11: **Mean Flow Velocities and Surface Pressures, Case 2**
top and middle: Cases 2a and 2b respectively, colour contours show velocity magnitudes in the vicinity of the actuator, unit vectors indicate the flow direction. **bottom:** reduced surface pressures are associated with regions of mean recirculating flow, **solid,** case 2a; **dashed,** case 2b. Mean flow behaviours appear different depending on the means of representing the actuator.

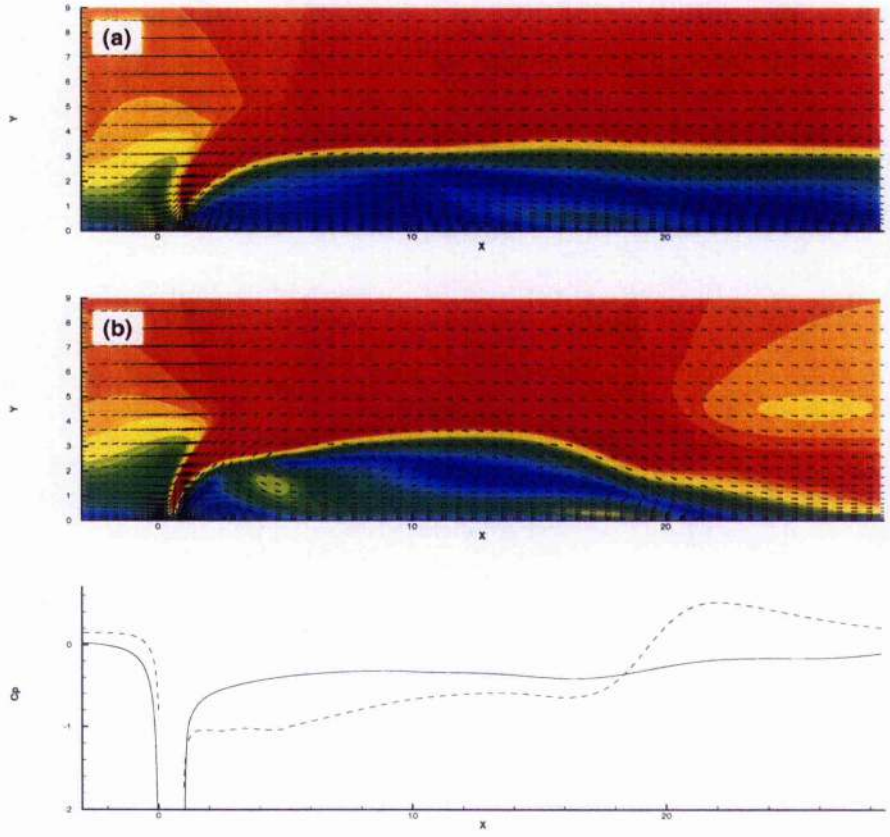

Figure 3.12: **Mean Flow Velocities and Surface Pressures, Case 3**
top and middle: Cases 3a and 3b respectively, colour contours show velocity magnitudes in the vicinity of the actuator, unit vectors indicate the flow direction. **bottom:** reduced surface pressures are associated with regions of mean recirculating flow, **solid,** case 3a; **dashed,** case 3b. Mean flow behaviours appear different depending on the means of representing the actuator.

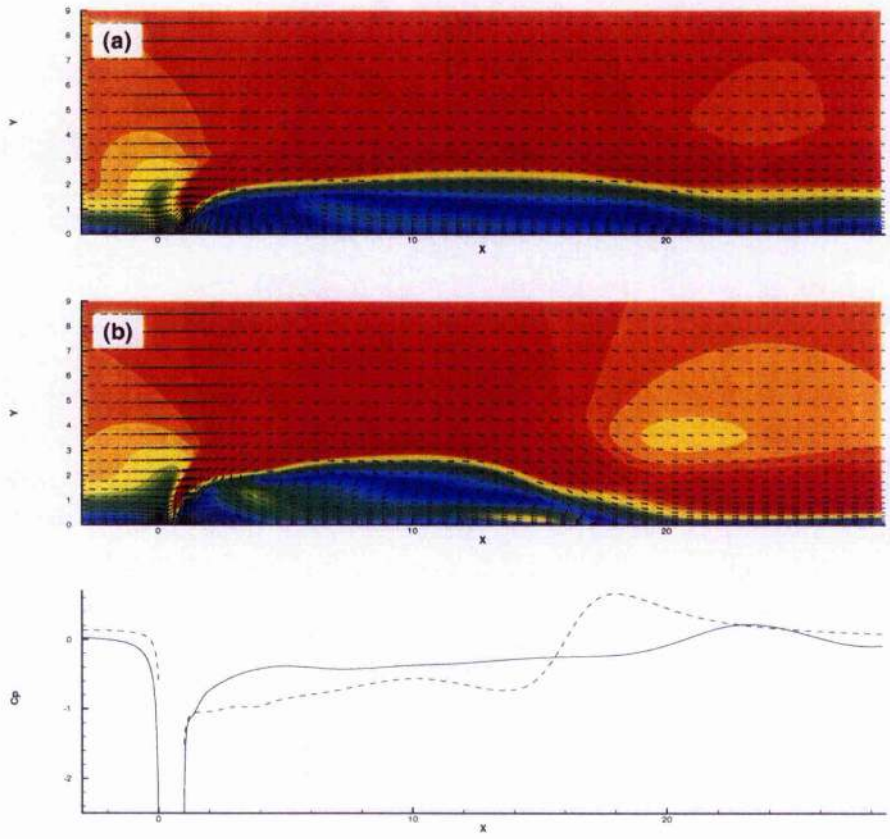

Figure 3.13: **Mean Flow Velocities and Surface Pressures, Case 4**
top and middle: Cases 4a and 4b respectively, colour contours show velocity magnitudes in the vicinity of the actuator, unit vectors indicate the flow direction. **bottom:** reduced surface pressures are associated with regions of mean recirculating flow, **solid,** case 4a; **dashed,** case 4b. Mean flow behaviours appear different depending on the means of representing the actuator.

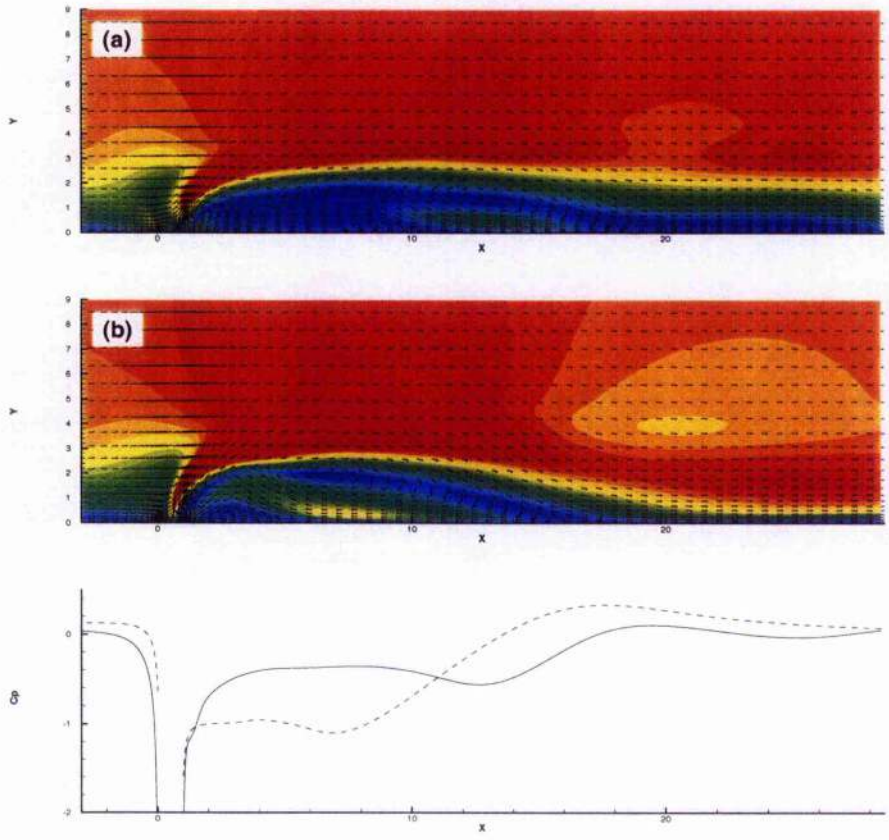

Figure 3.14: **Mean Flow Velocities and Surface Pressures, Case 5**
top and middle: Cases 5a and 5b respectively, colour contours show velocity magnitudes in the vicinity of the actuator, unit vectors indicate the flow direction. **bottom:** reduced surface pressures are associated with regions of mean recirculating flow, **solid,** case 5a; **dashed,** case 5b. Similar behaviour can be observed for either actuation approach. For the deforming cavity case (5a), a mean recirculating region is located some distance downstream of the actuator. This is larger for the oscillating velocity boundary condition case (5b) and is located closer to the actuator exit. The scale and location of this structure are reflected in the mean surface pressure distribution.

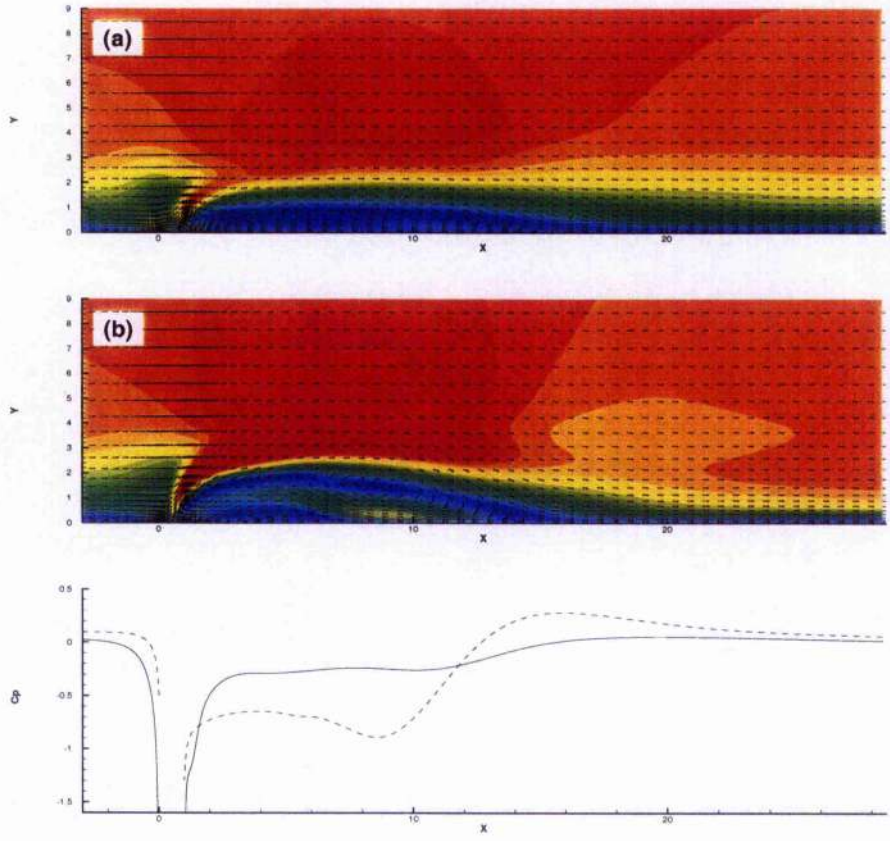

Figure 3.15: **Mean Flow Velocities and Surface Pressures, Case 6**
top and middle: Cases 6a and 6b respectively, colour contours show velocity magnitudes in the vicinity of the actuator, unit vectors indicate the flow direction. **bottom:** reduced surface pressures are associated with regions of mean recirculating flow, **solid,** case 6a; **dashed,** case 6b. A mean recirculating region exists in each case. This is considerably larger when the synthetic jet flow is imposed via a time varying velocity boundary condition.

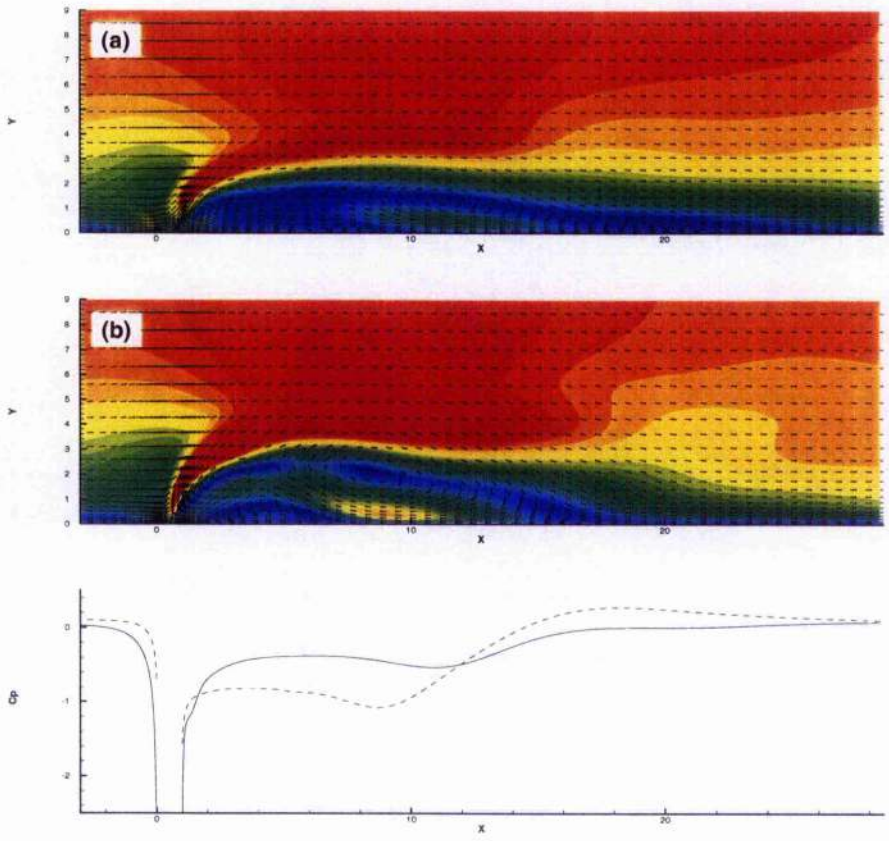

Figure 3.16: **Mean Flow Velocities and Surface Pressures, Case 7**
top and middle: Cases 7a and 7b respectively, colour contours show velocity magnitudes in the vicinity of the actuator, unit vectors indicate the flow direction. **bottom:** reduced surface pressures are associated with regions of mean recirculating flow, **solid,** case 7a; **dashed,** case 7b. A mean recirculating region is again produced for each case.

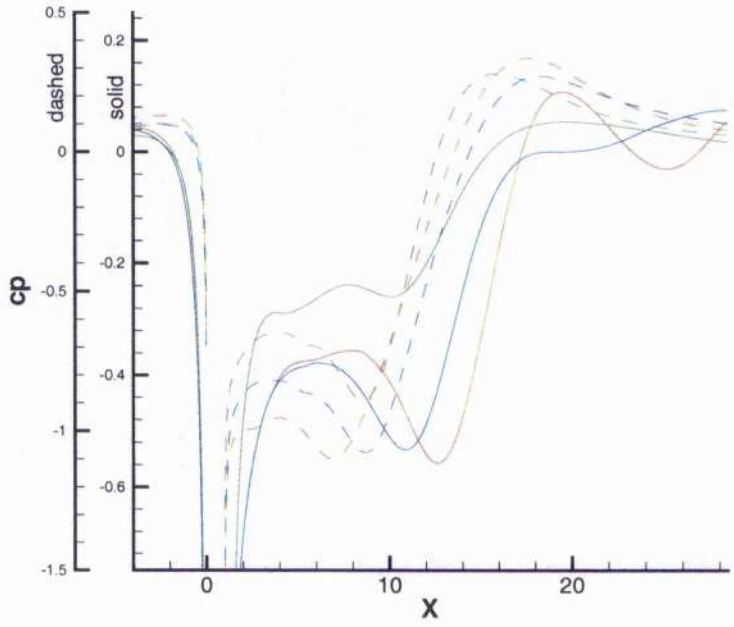

Figure 3.17: **Mean Surface Pressures, Cases 5, 6 and 7**, These cases have shown similar mean behaviour. C_p differences between them are most noticeably in terms of scale, this is seen by plotting the C_p distribution on normalised axes. *Red*, Case 5; *Green*, Case 6; *Blue*, Case 7.

Figures 3.18-3.24 establish three different patterns of behaviour. Figure 3.18 gives results for case 1. Here, vortices produced on actuation are individually convected under the influence of the crossflow. Cases 2b, 5b, 6a, 6b, 7a and 7b are shown in figures 3.19 and 3.22-3.24. These have previously been identified as displaying the same mean behaviour. In these figures (3.19 and 3.22-3.24), actuation can be seen to produce vortices which then appear to be consumed by a recirculation bubble which becomes established a short distance downstream of the exit. The exact location of this bubble may change during the course of the cycle, but it shows no tendency to be swept off downstream. This is a different flow regime to that demonstrated in figure 3.18.

Cases 2a, 3a, 3b, 4a, 4b and 5a (figures 3.19 to 3.22) demonstrate features from both of the above regimes. This intermediate behaviour will be referred to as the *transition* between the regimes which have already been mentioned. In these cases, vortices are individually convected, but are not accelerated towards the cross flow velocity. Instead, these become caught in the lee of vortices which succeed them and decelerate, dissipating close to the actuator exit. Were the freestream and operating parameters to be adjusted continuously to facilitate a change of regime, it is hypothesised that the furthest downstream vortices ultimately become stationary preceeding a permanently established recirculating region.

Comparing deforming cavity and velocity boundary condition actuation, both are shown to be capable of producing the same kind of flow regimes. However, as evidenced by figure 3.19, this does not always happen for the same conditions of freestream and massflow rate. A velocity boundary condition which more closely approximates the time-varying exit profile of the deforming cavity could reasonably be expected to reduce the range where there is a difference in flow behaviour between the two approaches. In all of the current comparisons, the velocity boundary condition generates stronger vorticity.

3.4.4 Summary

The operation of a synthetic jet actuator issuing into a crossflow has been investigated. The actuator introduces vortices to the flow at the downstream nozzle edge.

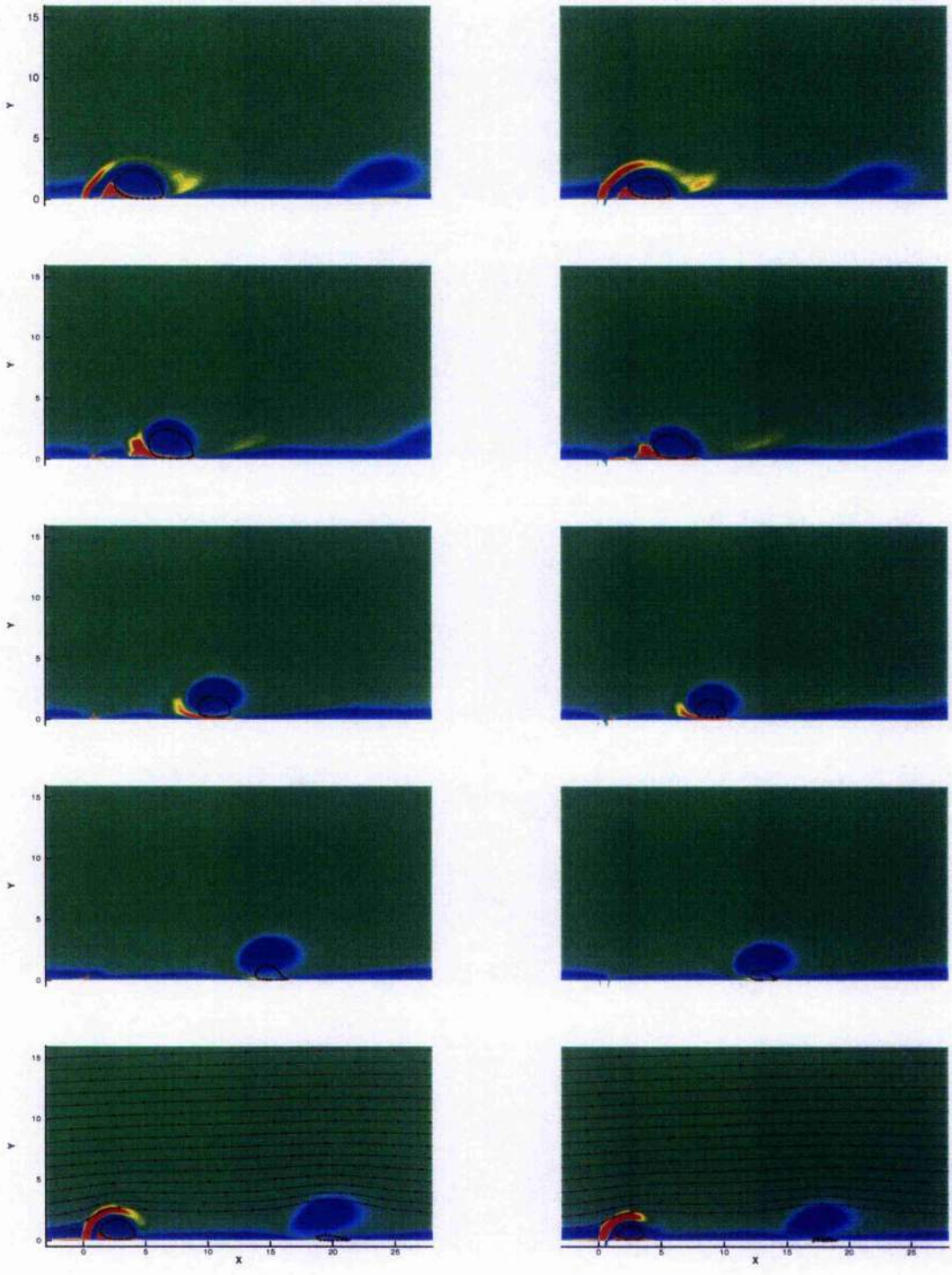

Figure 3.18: **Sequenced Vorticity Plots, Case 1, Left Column:** case 1b, **Right Column:** case 1a, Streamlines are used to indicate rotational fluid structures, and in the bottom frames, are used to illustrate the cross flow. Vortices produced on each blowing schedule are similar for cases 1a and 1b. These are individually convected by the freestream.

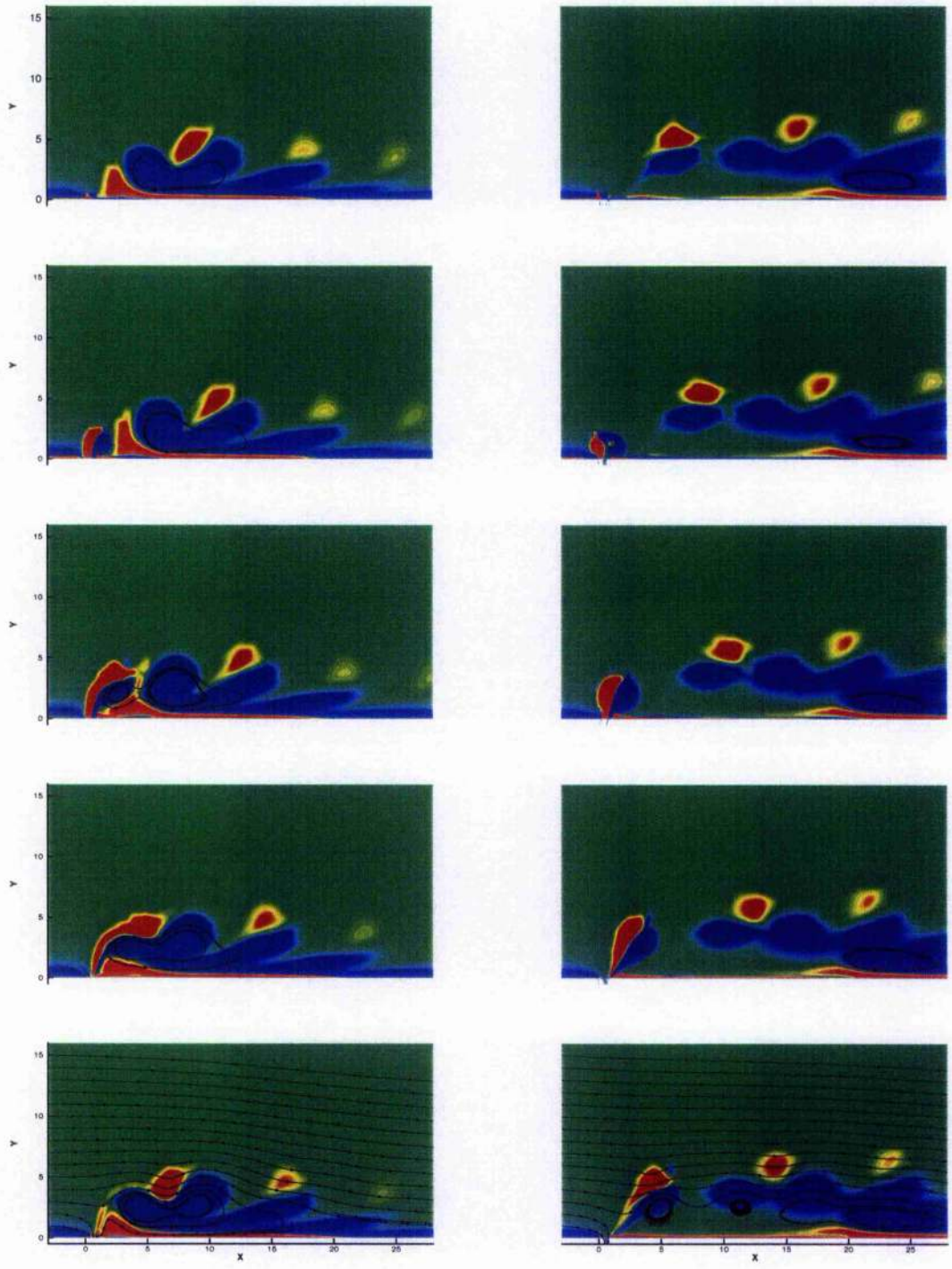

Figure 3.19: **Sequenced Vorticity Plots, Case 2, Left Column:** case 2b, **Right Column:** case 2a, Different flow behaviours are apparent depending on how the actuation is represented. On the left, a recirculating region is permanently established close to the actuator exit. This occurs further downstream for the deforming cavity case shown on the right.

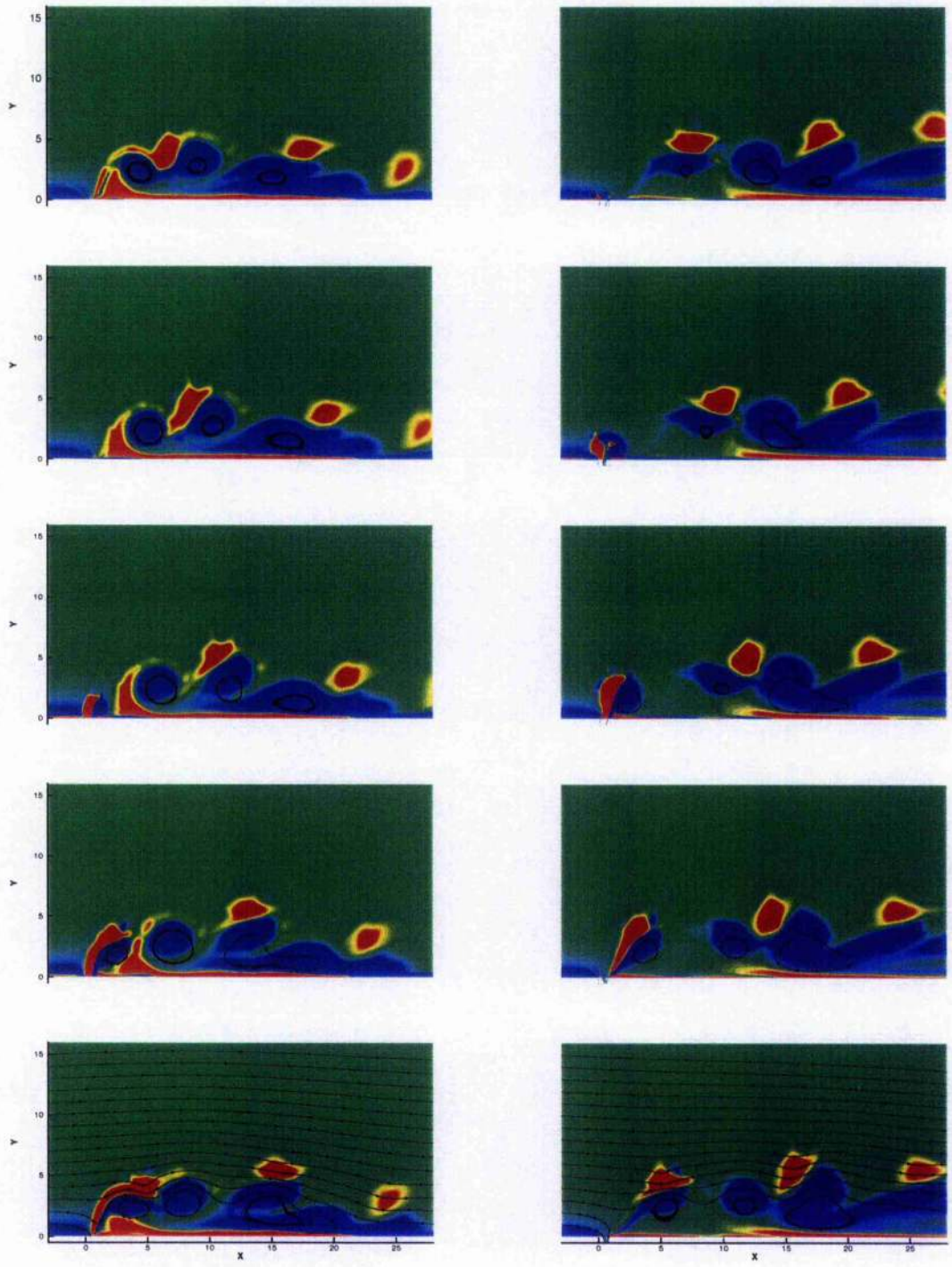

Figure 3.20: **Sequenced Vorticity Plots, Case 3, Left Column:** case 3b, **Right Column:** case 3a, Vortices slow after an initial acceleration and dissipate within a short distance of the actuator exit. For Case 3, freestream fluid travels a distance of $x/h = 8$ per cycle.

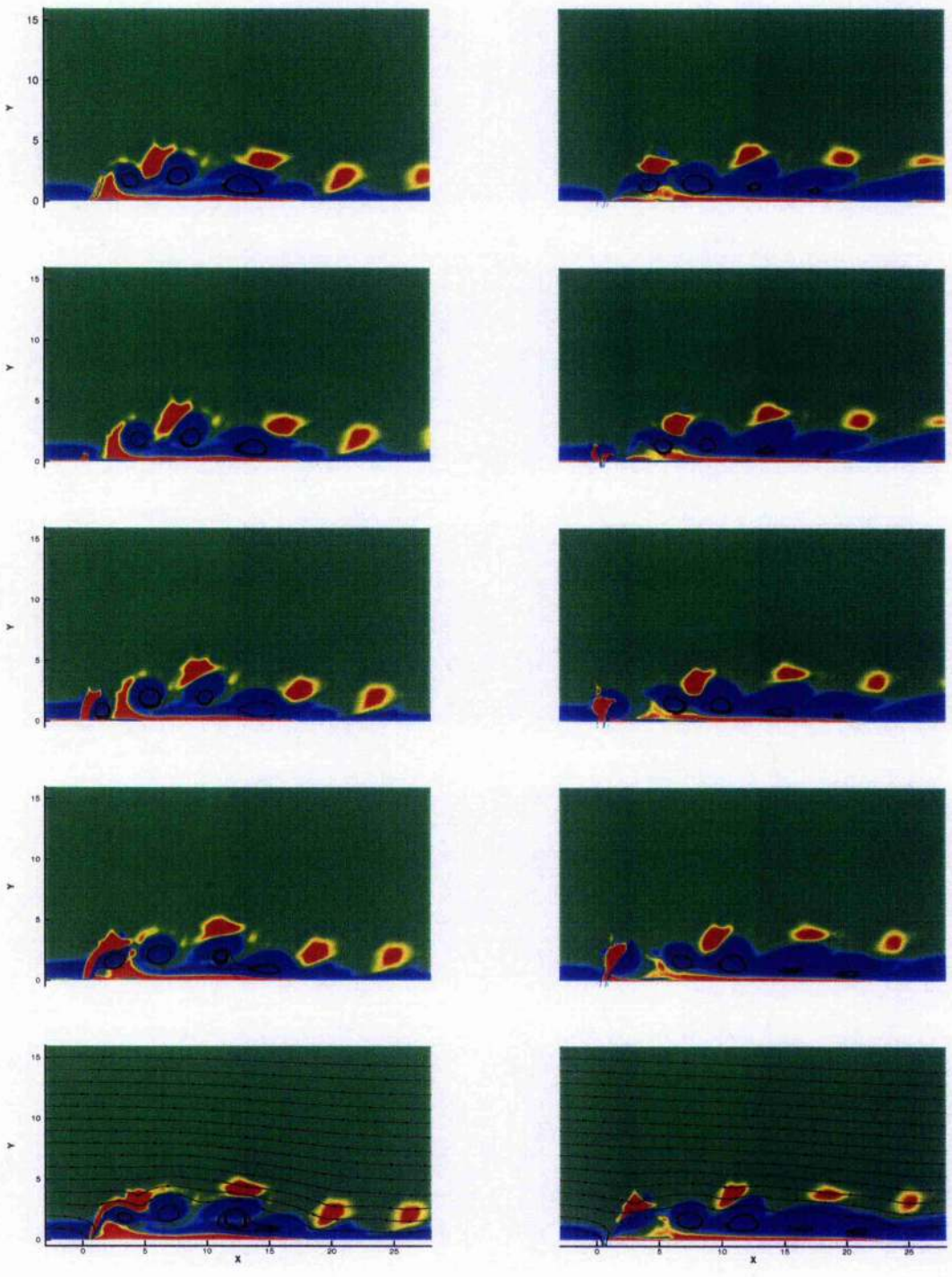

Figure 3.21: **Sequenced Vorticity Plots, Case 4, Left Column:** case 4b, **Right Column:** case 4a, Once again, vortex motion is impeded, and vortices dissipate within a short distance of the actuator.

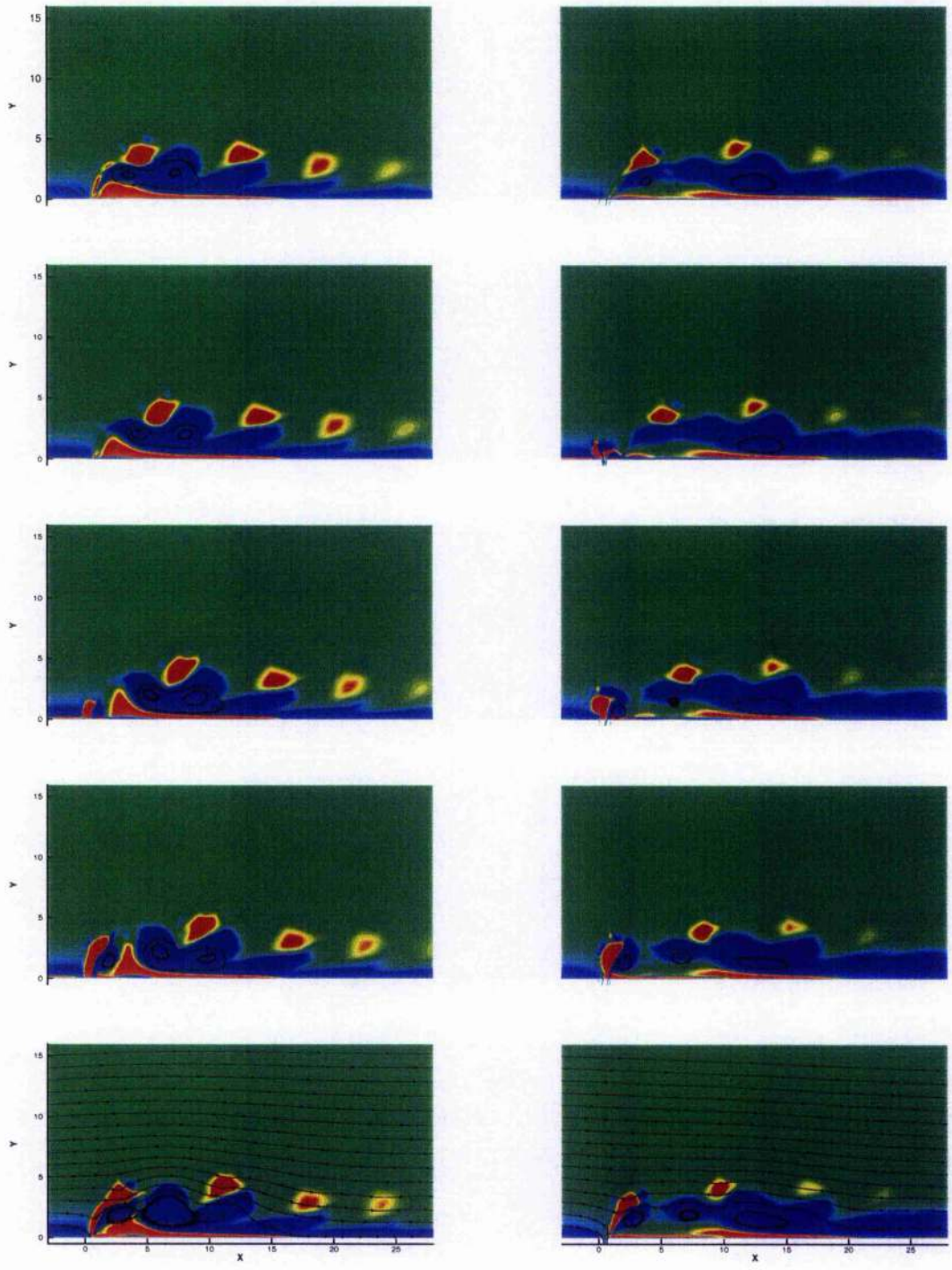

Figure 3.22: **Sequenced Vorticity Plots, Case 5, Left Column:** case 5b, **Right Column:** case 5a, On the left (5b), a recirculating region is permanently established close to the actuator exit. For the deforming cavity case (5a), vortices dissipate some short distance downstream.

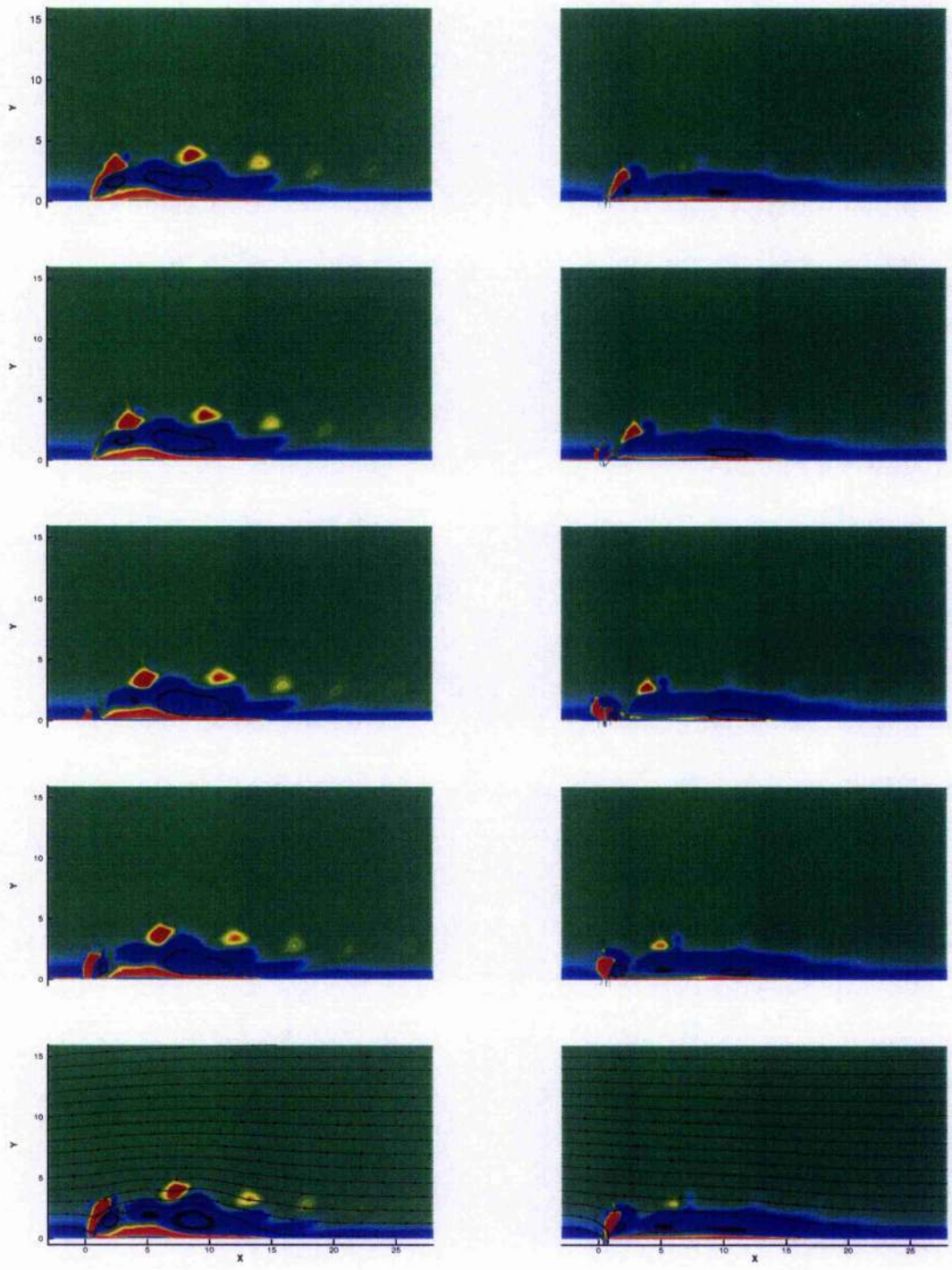

Figure 3.23: **Sequenced Vorticity Plots, Case 6, Left Column:** case 6b, **Right Column:** case 6a, In either case a permanently established recirculating region is formed. The small scale of this reflects the lower mass flow rates for ejected fluid.

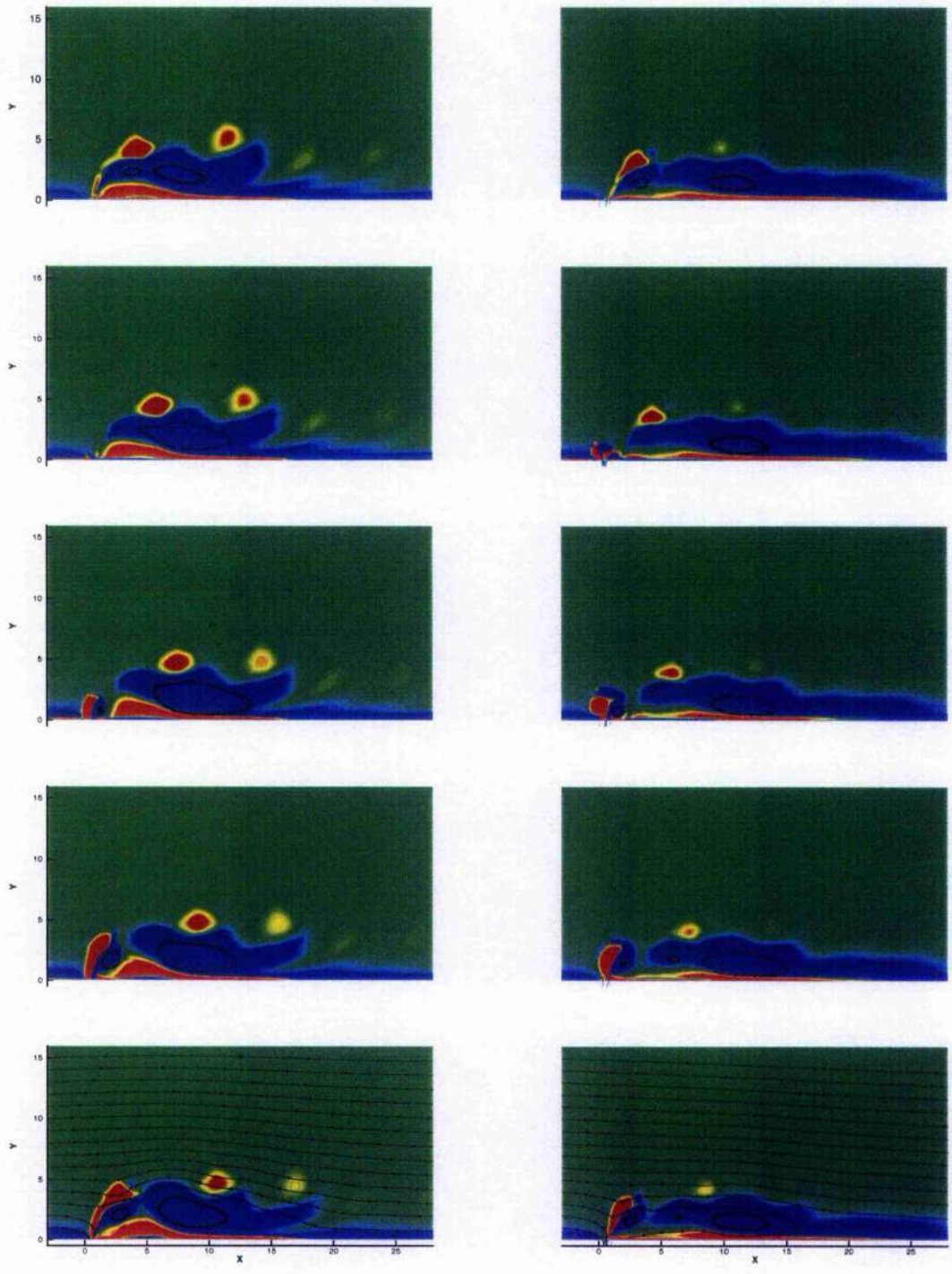

Figure 3.24: **Sequenced Vorticity Plots, Case 7, Left Column:** case 7b, **Right Column:** case 7a, For either representation of the actuator, a permanent recirculation region is formed.

The subsequent behaviour of these vortices and the reaction of the primary flow may be classified as one of two flow regimes depending on freestream and operating parameters. The first regime is described as individually convected vortices, in which case vortices introduced by the actuator are accelerated by the freestream such that the distance between successive vortices increases moving downstream. The alternative flow state has successive vortices instead feeding into a recirculation region which becomes permanently established a short distance downstream of the actuator exit.

Using the deforming cavity model developed in chapter 2, initial cases were run at a constant Reynolds Number Re_h, and using a constant cavity floor deflection, A. Massflow rate from the cavity nozzle varied with the reduced frequency k_h but was found to be independent of the flat plate length upstream of the actuator, x_{le}, and hence of the local boundary layer thickness, δ.

The flow behaviour produced by a deforming cavity type synthetic jet actuator in a crossflow, was compared with a simpler actuator representation where the actuator exit velocity is imposed as a boundary condition at the nozzle exit plane, i.e. without modelling the dynamics of the cavity. The simple actuator model represented the jet flow with a symmetric velocity profile whose magnitude varied sinusoidally in time. This differed considerably from complex time varying profiles generated by the deforming cavity. Peak imposed velocities were required to be greater in order to produce the same periodic mass flow. This had the effect of introducing stronger vorticity to the crossflow. Despite the differences between the two models; across a practical range of reduced frequency, similar flows were observed for both the velocity boundary condition model and full deforming cavity.

Chapter 4

Synthetic Jet in Crossflow: Parameter Study

4.1 Overview

It is not sufficient that the actuator is capable of altering the crossflow behaviour. In order to be useful for control, it is necessary that the response of the primary flow is predictable, given changes in the actuator operation. This chapter is a parameter study performed in order to facilitate prediction based on experience. This is gained from a number of trial cases which consider various crossflows (defined by Re_h and x_{le}) with an actuator having different operating conditions (V_0/U_∞ and k_h).

Given the similarity of structures produced by the different actuator representations, results discussed here have been obtained by imposing a time-varying velocity as a boundary condition. Even for a simple model there are several parameters to consider, each of which may have a substantial range. The current study has considered parameter combinations at the edges of what is practically realisable. Despite the extent of the parameter space, only the same two regimes were observed as in Chapter 3.

This chapter is organised into sections which describe independently the effect of the parameters, peak velocity V_0/U_∞, actuator reduced frequency k_h, freestream Reynolds number Re_h, and x_{le}, the distance between the actuator and the leading edge of the flat plate. The emphasis is placed on how the variation of parameters

affects the flow character.

4.2 Dimensional Analysis

Dimensional analysis allows that the behaviour of a synthetic jet operating in a crossflow be characterised by the smallest number of non-dimensional parameters. This chapter uses the Buckingham-Pi theory as described in reference [81]. The first step in this process is to identify all the independent parameters which define the problem.

There are clearly two significant and independent velocity scales and two length scales; those associated with the jet and those associated with the cross flow. In the absence of a deforming cavity, the jet flow is characterised by the imposed peak velocity V_0. Ejected fluid is subjected to a crossflow defined by the freestream velocity U_∞. In the simplest model, the actuator geometry is described by the exit width h. The time varying actuation is described by a single characteristic frequency, f.

Often in publications featuring parallel flows, the boundary layer thickness δ, is used to define the crossflow. This is related to the upstream length x_{le}, over which the boundary layer is developed. Since δ and x_{le} are not independent, only one may be used for dimensional analysis according to the Buckingham-Pi theory. In computational as well as in physical experiments, it is desirable to use parameters which can be directly and independently controlled. In the current CFD experiments, X_{le} can be easily adjusted and is chosen for this reason.

A full list of the parameters which are considered, and the classification of their units in terms of mass M, length L and time T is given below,

f	actuator frequency (T^{-1})	h	actuator exit width (L)
U_∞	freestream velocity (LT^{-1})	V_0	peak jet velocity (LT^{-1})
ρ_∞	freestream density (ML^{-3})	μ	viscosity $(ML^{-1}T^{-1})$
x_{le}	distance over which the boundary layer is developed (L)		

According to Buckingham-Pi theory, the number n, of non-dimensional groups, or *pi* terms which may be used to characterise the flow behaviour, is determined by, $n = k - r$, where $k(= 8)$ is the number of parameters and $r(= 3)$, the number of reference dimensions (length L, time T and mass M). For each *pi* term, a *repeating* characteristic variable is chosen, therefore three are required for this analysis.

Using h, U_∞ and ρ_∞, then the *pi* terms are formed by considering which combinations of the remaining variables can be multiplied by each of these in turn to produce non-dimensional products. This gives the *pi* terms,

$$\prod_1 = \frac{fh}{U_\infty} \qquad \prod_2 = \frac{V_0}{U_\infty} \qquad \prod_3 = \frac{x_{ie}}{h} \qquad \prod_4 = \frac{\rho U_\infty h}{\mu_\infty}$$

The first of these $\prod_1$, can be related directly to a reduced frequency, k ($k_h = \omega h/(2U_\infty) = \pi \prod_1$). The second term relates velocity scales associated with the jet to those of the freestream. Next, the geometric scales are related. Either the boundary layer thickness δ, or the distance over which this is developed, x_{ie}, may be used to define a ratio with the actuator width, h. The final *pi* term, $\prod_4$, is a *Reynolds number*. Any boolean condition (i.e. having true or false possibilities), has a dependence on these non-dimensional independent variables. The existence of recirculation regions for example, can be given a descriptor Z having values $Z = 1$ for *true*, and $Z = 0$ for *false*. This can then be described with a relationship derived by experiment,

$$Z = f(Str_h, \frac{V_0}{U_\infty}, \frac{x_{ie}}{h}, Re_h) \tag{4.1}$$

The preceeding derivation has not considered the effects of fluid compressibility. This would require an additional dimensional parameter, the modulus of elasticity E_v, which relates pressure and density changes. In discussion of gases, the closely related sonic velocity ($a = \sqrt{E_v/\rho}$), is often used instead. If compressibility effects are known to be important, then either E_v or a should be included in the dimensional analysis. The latter directly introduces another velocity ratio, U_∞/a, i.e. the familiar freestream Mach number, M_∞.

The current study neglects Mach number effects for now, and maintains low freestream Mach numbers throughout. The ommission must be kept in mind however, espe-

cially for cases where a high velocity ratio, V_0/U_∞, is used, and therefore local Mach numbers are considerably greater than freestream.

4.3 Numerical Formulation

4.3.1 Grids and Boundary conditions

Medium density grids as described in the previous chapter were again employed for the more extensive parameter study in this chapter. These are comprised of seven rectangular blocks; the lower surface of the centre block representing the actuator. Boundary conditions were also as used in the previous chapter. Left and upper boundaries maintain a freestream condition. The outflow boundary on the right has all flow properties extrapolated from the interior solution, except the pressure which is set at the freestream value. Lower surfaces of the upstream and downstream blocks are symmetry boundaries. Other lower surfaces are wall boundaries except that of the centre jet block, where the velocity is represented as the time varying velocity,

$$v(x,t)_{y=0} = V_0 \sin^2(\pi x/h)\sin(\omega t) \quad \text{for} \quad 0 \leq x \leq h \tag{4.2}$$

In this chapter, V_0/U_∞ takes one of three values, 1.0, 2.0 or 3.0.

The parameter field is also defined by the reduced frequency k_h, plate length upstream of the actuator x_{le}, and the Reynolds number Re_h. Reduced frequency values used are $k_h = 0.025\pi$, 0.05π,0.08π, 0.1π, 0.125π, 0.16π and 0.2π. Upstream distances along the flat plate are $x_{le} = 50h$, $100h$ and $200h$. Reynolds number Re_h, based on the actuator width h were $Re_h = 350$, 700, 1750 and 3500. For an actuator of the order $h = 0.1$ to $1.0mm$, these values Re_h correspond to typical chord Reynolds numbers Re_c, for a retreating helicopter rotor blade.

In the last chapter, the simple velocity boundary condition approach was compared with the a deforming cavity, and was found to be capable of producing the same flow behaviours. It deserves to be emphasised that a Reynolds number of $Re_h = 350$ was used throughout chapter 3, and therefore this chapter diverges from previous

experience. It shall be seen that the results and trends which are reported here are consistent with what has already been learned but further validation at higher Reynolds numbers against a deforming cavity type actuator is clearly desirable.

4.3.2 Physical Interpretation of Dimensionless Parameters

The highest and lowest values for the non-dimensional parameters, Re_h, k_h and V_0/U_∞ provide eight extreme combinations. However, since each non-dimensional parameter is itself the product of a number of physical variables, any combination represents a range of physical situations. Not all of these are physically possible, for example, there is a limit to how small the actuator exit width h, can be manufactured. To put physical meaning to a combination of the non-dimensional parameters and to the range of physical possibilities which they represent, it is necessary to consider realistic values and limits for the physical variables. Tables 4.1 and 4.2 are discussed below. These provide examples of cases represented within the current parameter study, and serve to link dimensional and non-dimensional descriptions.

First consider that the non-dimensional parameters, Re_h, k_h and V_0/U_∞, can be described with the physical variables, ρ, U_∞, h, μ, f and V_0. Assuming a standard atmoshere to provide realistic constant values for density ρ, and viscosity μ, and setting these as $\rho = 1.225 kg/m^3$ and $\mu = 1.789 \text{ x } 10^5\ kg/(ms)$, the Reynolds number, $Re_h = \rho U_\infty h/\mu$, is dependent only on U_∞ and h. This is demonstrated in table 4.1, which gives Reynolds numbers for specified values of U_∞ and h. Reynolds numbers for the current study lie between $Re_h = 350$ and $Re_h = 3500$. Blank regions on the top left and bottom right of the table illustrate these bounds.

For each combination of U_∞ and h, a dimensional frequency f (Hz), can be simply calulated from any reduced frequency, $k_h = \pi f h/U_\infty$. Table 4.2 shows frequency f, for cases where the reduced frequeny is $k_h = 0.2\pi$, i.e. the highest reduced frequency used in the current parameter study. Frequencies f (Hz), correspond to the Reynolds numbers given in table 4.1.

It is important to emphasize the assumptions which have been made for the construction of tables 4.1 and 4.2. A standard atmosphere has been used to give constant values for μ and ρ. The practical possibility of U and h values is also implied by

$U_\infty(m/s)$	h (mm)											
-	0.1	0.2	0.3	0.4	0.5	0.6	0.7	0.8	0.9	1.0	1.1	1.2
5						205	240	274	308	342	377	411
10	**$Re_h < 350$**			274	342	411	479	548	616	685	753	822
15			308	411	514	616	719	822	924	1027	1130	1233
20			411	548	685	822	959	1096	1233	1369	1506	1643
25		342	514	685	856	1027	1198	1369	1541	1712	1883	2054
30		411	616	822	1027	1233	1438	1643	1849	2054	2260	2465
35		479	719	959	1198	1438	1678	1917	2157	2397	2636	2876
40		548	822	1096	1369	1643	1917	2191	2465	2739	3013	3287
45		616	924	1233	1541	1849	2157	2465	2773	3081	3389	3698
50	342	685	1027	1369	1712	2054	2397	2739	3081	3424	3766	
60	411	822	1233	1643	2054	2465	2876	3287	3698	4108		
70	479	959	1438	1917	2397	2876	3355	3835				
80	548	1096	1643	2191	2739	3287	3835					
90	616	1233	1849	2465	3081	3698						
100	685	1369	2054	2739	3424			**$Re_h > 3500$**				
110	753	1506	2260	3013	3766							
120	822	1643	2465	3287								
130	890	1780	2670	3561								

Table 4.1: **Reynolds Numbers for Combinations of U_∞ and h:** A standard atmosphere having $\rho = 1.225 kg/m^3$ and $\mu = 1.789$ x 10^5 $kg/(ms)$ has been assumed. The current parameter study uses Reynolds numbers between $Re_h = 350$ and $Re_h = 3500$

$U_\infty(m/s)$	h (mm)											
-	0.1	0.2	0.3	0.4	0.5	0.6	0.7	0.8	0.9	1.0	1.1	1.2
5						1667	1429	1250	1111	1000	909	833
10					4000	3333	2857	2500	2222	2000	1818	1667
15			10000	7500	6000	5000	4286	3750	3333	3000	2727	2500
20			13333	10000	8000	6667	5714	5000	4444	4000	3636	3333
25		25000	16667	12500	10000	8333	7143	6250	5556	5000	4545	4167
30		30000	20000	15000	12000	10000	8571	7500	6667	6000	5455	5000
35		35000	23333	17500	14000	11667	10000	8750	7778	7000	6364	5833
40		40000	26667	20000	16000	13333	11429	10000	8889	8000	7273	6667
45		45000	30000	22500	18000	15000	12857	11250	10000	9000	8182	7500
50	100000	50000	33333	25000	20000	16667	14286	12500	11111	10000	9091	
60	120000	60000	40000	30000	24000	20000	17143	15000	13333	12000		
70	140000	70000	46667	35000	28000	23333	20000	17500				
80	160000	80000	53333	40000	32000	26667	22857					
90	180000	90000	60000	45000	36000	30000						
100	200000	100000	66667	50000	40000							
110	220000	110000	73333	55000	44000							
120	240000	120000	80000	60000								
130	260000	130000	86667	65000								

Table 4.2: **Operating Frequencies for Combinations of U_∞ and h:** Frequencies correspond to Reynolds numbers in table 4.1 and are in Hertz (Hz). Values at the bottom left are impractical for currently reported actuators. A horizontal line at $U_\infty = 45m/s$ illustrates the limit when $V_0/U_\infty = 3.0$.

their inclusion in the tables. However, there is an additional consideration for velocities. In this section the velocity ratio, V_0/U_∞, has values $V_0/U_\infty = 1.0$, 2.0 and 3.0. To satisfy the assumption made in the dimensional analysis that compressibility effects are small, there have to be individual limits on the values that V_0 and U_∞ can take. If for example, a standard atmosphere is assumed where the sonic velocity $a = 340.2m/s$, and if compressibility effects become important when $V_0 = 0.4a$, then $U_{\infty_{max}} = 136.08$, 68.04 and 45.36 m/s, corresponding to each of the velocity ratios. For illustration, the limit when $V_0/U_\infty = 3.0$, i.e. $U_{\infty max} = 45$ m/s, is marked by a horizontal line in table 4.2.

There is also a limit to the operating frequency which a practical actuator can be expected to achieve. Some values of frequency shown in table 4.2, particularly toward the bottom left of the table, may be impossibly high.

4.4 Parameter Study

4.4.1 Effect of Varying the Actuator Reduced Frequency

Initial numerical experiments considered the actuator operating at various reduced frequencies. A grid having $x_{te} = 200h$ was used and the Reynolds number was set at $Re_h = 350$. Reduced frequencies were in the range, $k_h = 0.025\pi$ to 0.2π as in the previous chapter. However, in this case, the peak actuator velocity was maintained at a constant $V_0/U_\infty = 3.0$, so that the reduced frequency effects could be studied in isolation.

Figure 4.1 shows the time-average position of streaklines for seven initial cases. In each case the trace passes through the point $(x, y) = (-4h, 0.4h)$. The streakline displacement increases steadily from the lowest reduced frequency, $k_h = 0.025\pi$, to actuation at $k_h = 0.125\pi$. At higher reduced frequencies, the displacement once again decreases. Figure 4.1 also shows mean surface pressure distributions. The case where $k_h = 0.125\pi$ also gives the greatest net pressure force, $\int_x p\,dx$.

Figures 4.2 and 4.3 show sequenced vorticity field plots when $k_h = 0.08\pi$, 0.1π, 0.125π and 0.16π. In the previous chapter, different flow regimes were observed depending on the primary flow, and on the actuator location and operating conditions.

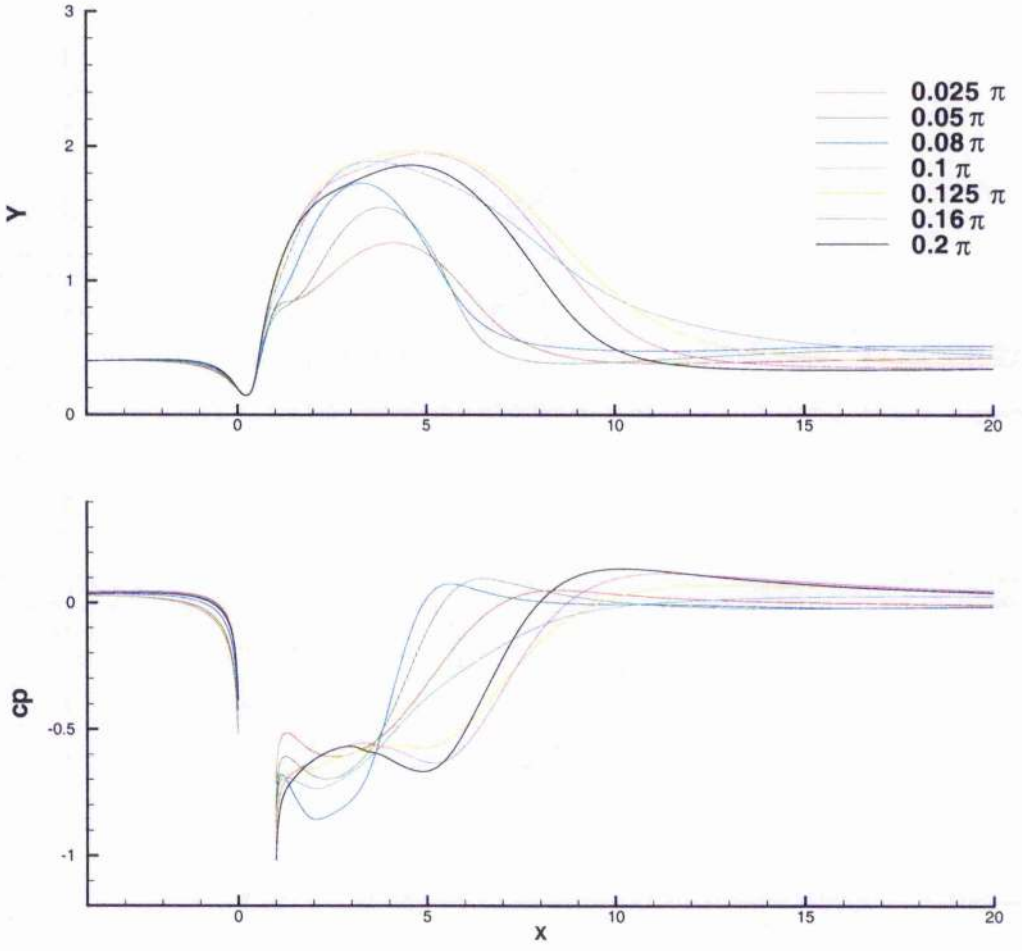

Figure 4.1: **Mean Streakline Displacement and Pressure Distribution**, variation with increasing reduced frequency k_h. In the streakline plot, the X and Y axes are scaled independently for clarity. Maximum net pressure force, $\int_X p\,dx$, and maximum streakline displacement coincide with the lowest frequency occurence of recirculating regions

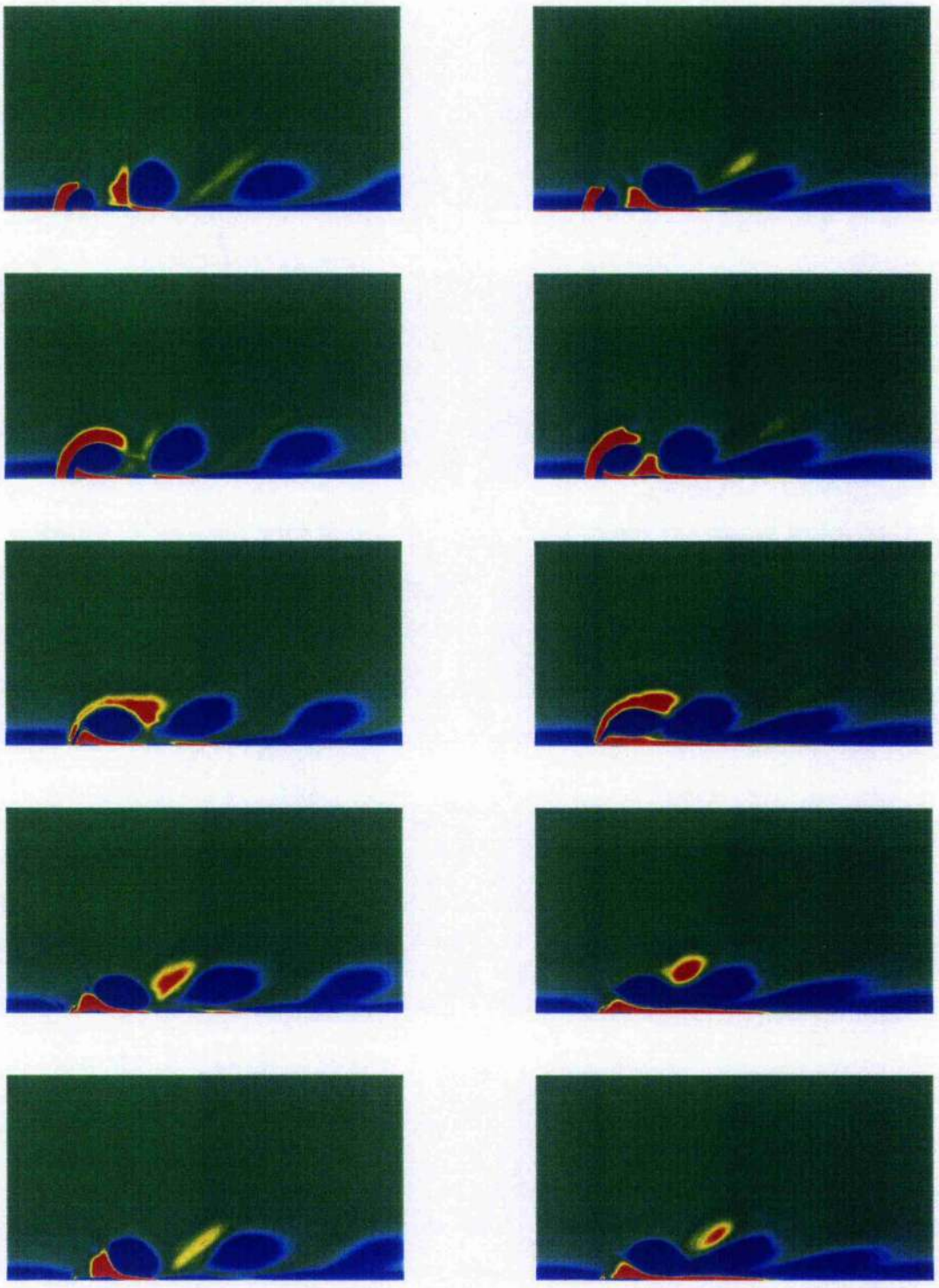

Figure 4.2: **Sequenced Vorticity Plots, left:** $k_h = 0.08\pi$, **right:** $k_h = 0.1\pi$, On the left, structures are being individually convected. On the right, these dissipate within a short distance of the actuator exit.

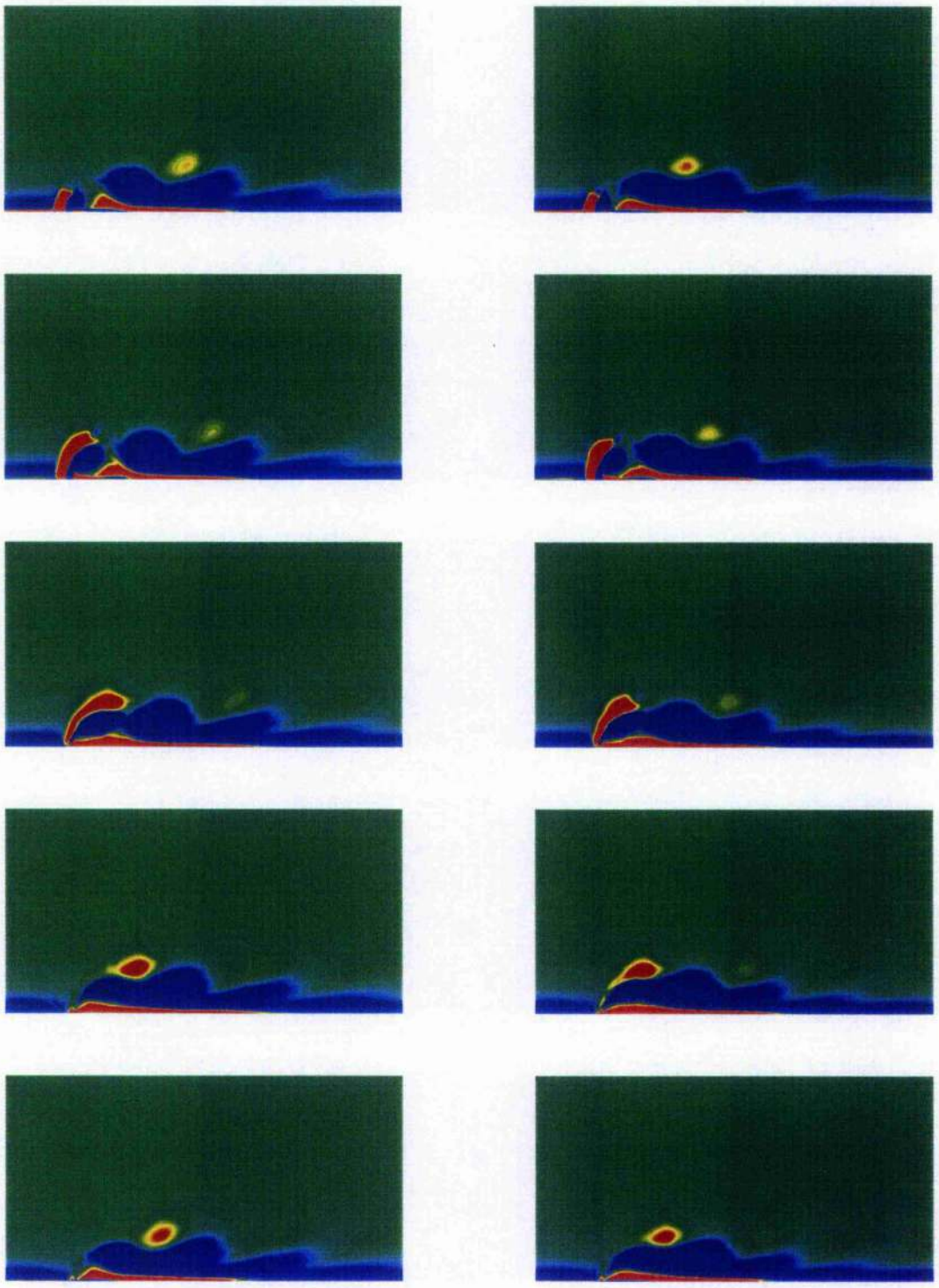

Figure 4.3: **Sequenced Vorticity Plots, left:** $k_h = 0.125\pi$, **right:** $k_h = 0.16\pi$, vorticity distribution is charateristic of permanent recirculating regions seen in the last chapter.

Figures 3.18-3.24 in the previous chapter, imply that permanently established recirculating regions are promoted with increasing reduced frequency. From figures 4.2 and 4.3, it can be seen that amongst the current results, the case where $k_h = 0.125\pi$ represents the lowest frequency causing a permanently established recirculating region. When such a regime is established, streamlines are redirected over the bubble and the effective aerodynamic shape change is not simply a time mean effect.

Knowing which regime is in place for each plot, figure 4.1 suggests that the point at which permanently located recirculation regions are established coincides with the maximum streakline displacement and the minimum net mean pressure force, $\int_X p\,dx$. The latter of these may be considered as a definition of the actuators effectiveness. If maximum effectiveness generally coincides with the lowest frequency occurence of recirculating regions then this association offers a clear and simple control goal. Optimal actuation lies on the boundary between regimes, which can be determined by the systematic variation of parameters. Such a parameter study only has to classify cases on the basis of which regime is in place.

When figure 4.1 is again considered, and now bearing in mind the flow regime associated with each plot, there appears to be a considerable difference when moving between regimes. Cases having $k_h = 0.125\pi$, 0.16π and 0.2π all share the same regime and differ only slightly from each other. These results are quite different from cases having $k_h = 0.025\pi$, 0.05π or 0.08π. The effectiveness appears to rise sharply when permanently located recirculating regions became established ($k_h = 0.08\pi$ to $k_h = 0.125\pi$) but does not decrease so quickly with further reduced frequency increases ($k_h = 0.125\pi$ to $k_h = 0.2\pi$). For control, this provides a temptation to exceed the threshold ($k_{h_{crit}}$)where recirculation regions first become established, since the effectiveness cost of greatly exceeding the threshold is relatively small in comparison with the cost of failing to meet it.

Figure 4.4 shows the surface pressure distribution at 20 instants of the cycle. The seven initial cases are shown in separate frames. It is clear from this figure, that with increasing reduced frequency, the magnitude of downstream pressure variation, i.e. the unsteadiness, increases. The character of each plot has a dependence on the flow regime which is established. Downstream of the permanently established recirculating regions, frames on the right of figure 4.4 show successive traces forming a smooth

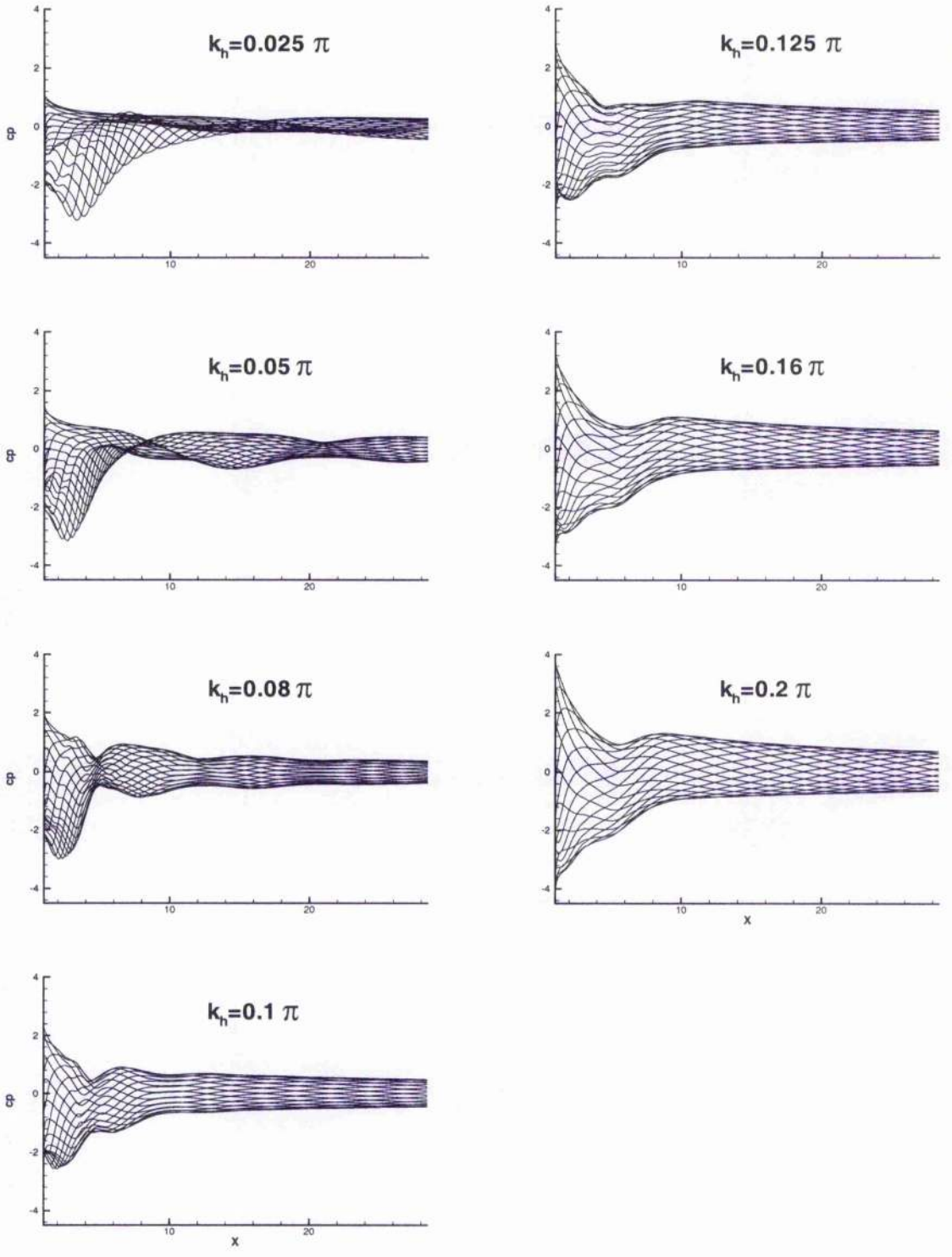

Figure 4.4: **Instantaneous Pressure Distribution Downstream of the Actuator**, variation with reduced frequency. The pressure distribution is shown at 20 instants of the cycle. Permanently located recirculating regions produce a smooth envelope extending downstream. Increased reduced frequency k_h, causes ever greater pressure disturbance.

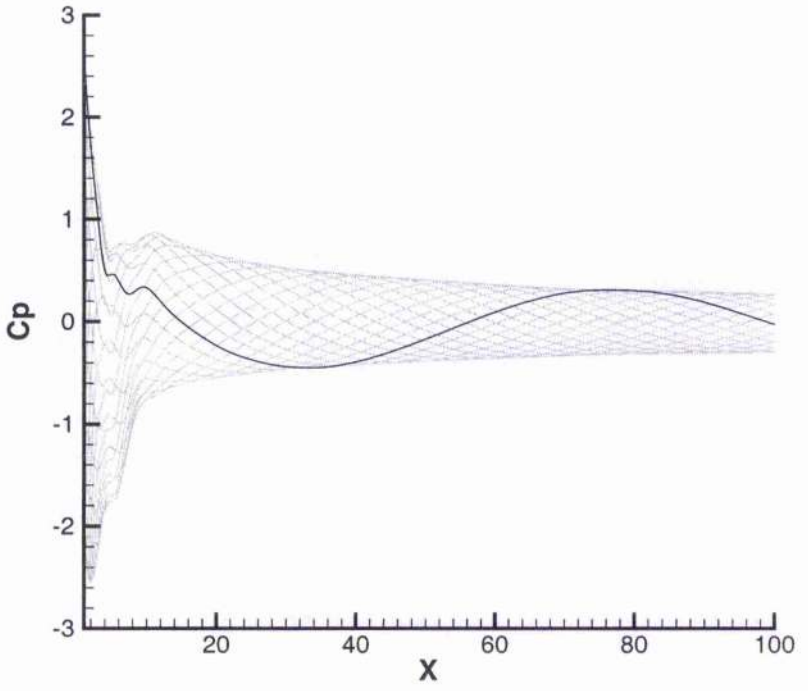

Figure 4.5: **Pressure Distribution Downstream of the Actuator** shown for an extended distance downstream. When a permanent recirculating region is present, downstream pressure oscillations are dominated by the disturbance of the actuator rather than the presence of vortices.

envelope. This indicates that pressure oscillations at these locations are being influenced by a single source. In these cases, pressure oscillations are directly caused by the actuation disturbance. In the top three frames on the left, surface pressures also have a time-varying component due to the location of convected vortices.

The pressure distribution for the $k = 0.125\pi$ case is shown for an extended distance downstream in figure 4.5. This is dominated at all times by a single clear wave. With a Mach number $M = 0.1$, acoustic waves travel a distance of $80h$ per cycle for this case, i.e. the wavelength of the highlighted wave. The acoustic effect can also be estimated from the figure. The amplitude of the time varying pressure coefficient is around $\Delta C_p = 0.5$ at a distance of $x = 20h$ to $30h$. Assuming a moderate standard atmosphere and with an exit width of $h = 0.5mm$, this corresponds to a sound

pressure level (SPL) of around $120dB$, where SPL is defined,

$$SPL = 10\ log_{10}\{I/I_0\} \tag{4.3}$$

The human threshold of pain is $120dB$ to $130dB$. These levels are found very close to the actuator. Sound intensity I, decreases as the inverse square of the distance x, from its source, i.e. $I \propto 1/x^2$. At a distance of $x = 5m$ or so, the actuator produces an SPL of around $70dB$, which is similar to the noise made by street traffic.

The cases described until now in this chapter, have been performed at a Reynolds number of $Re_h = 350$. If similar ΔC_p to that discussed above, is attained at higher Reynolds numbers, then noise levels will be even greater. This raises questions about applications where such noise levels can be tolerated, and about the feasibility of constructing millimetre scale actuators capable of producing such extreme pressure variations. Regarding the latter, it may be borne in mind that it is possible to deliver noise in excess of the human pain threshold using a small stereo headset as can be found in many homes.

A number of parameter combinations were used to confirm that optimal surface pressure distribution coincides with a change of flow regime. Further cases were then classified primarily in terms of the flow behaviour which they exhibited, i.e. the study seeks to find the location of the boundary between regimes. Owing to the extent of the parameter space, the tolerance to which this can be established grows increasingly large as parameter combinations are spread out. A further investigation of the effect of reduced frequency was made with a grid having $x_{le} = 600h$. The results of this are summarised in figure 4.6. These tests suggest that a recirculating region is produced with increasing reduced frequency. However, figure 4.6 shows that the ability to alter the flow behaviour using reduced frequency k_h depends also on the other parameters. Based on the results shown in figure 4.6 it can be stated that increases to the reduced frequency k_h, promote the occurence of recirculating regions. Adjustment to this parameter alone however, may not be sufficient for their production.

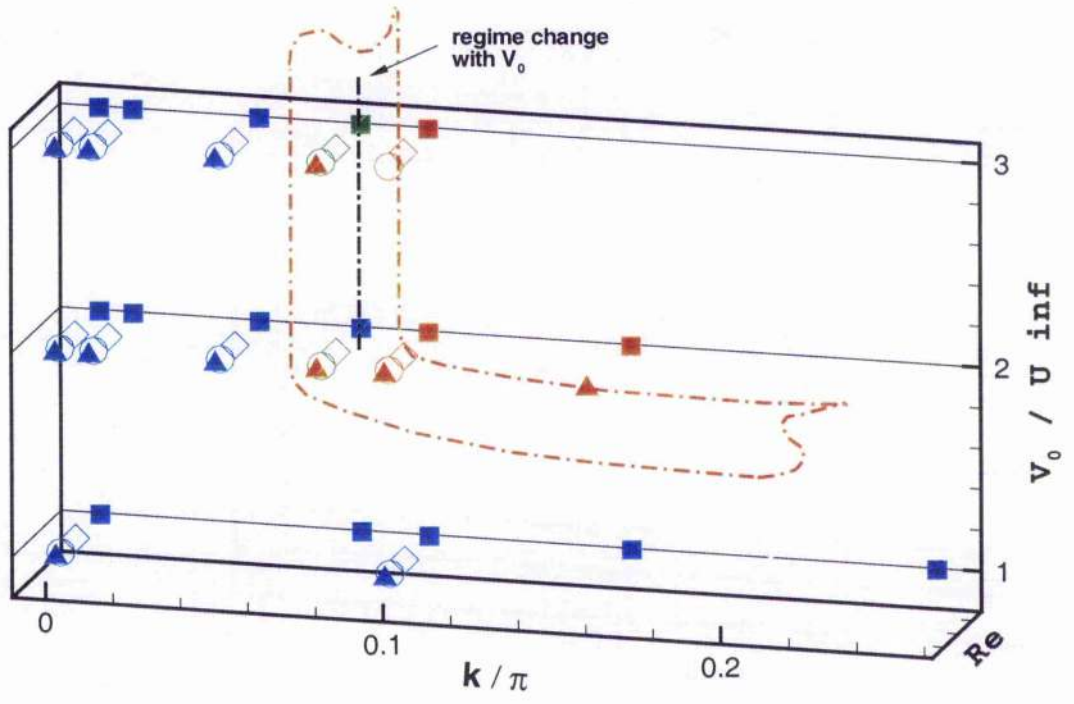

Figure 4.6: **Effect of Peak Velocity**, $x_{le} = 600h$; *blue* indicates individually convected vortices; *green* where convection is slow so that the disturbance remains local; *red* indicates that a permanent recirculating region is established. □.. Reynolds number $Re = 350$; ◇.. $Re = 700$; ○.. $Re = 1750$; △.. $Re = 3500$. The boundary between regimes represents a surface within the parameter space. An approximation of this is illustrated by red (dotted) lines. The vertical black (dotted) line highlights the situation where a regime change is provoked solely by altering the peak velocity V_0.

4.4.2 Effect of Varying Peak Velocity

Considering results when $x_{lc} = 600h$, the blowing velocity is found to be crucial in determining the nature of the flow. Three values of V_0/U_∞ were used, 1.0, 2.0 and 3.0 . For the lowest of these values, across a range of Reynolds and reduced frequency that were otherwise favourable, dissipation of the vortices generated on each blowing event meant that each had disappeared before the start of the next. Thus a recirculation region was only observed for the two higher values and it is established that there is a V_0/U_∞ threshold below which recirculating regions cannot be produced. This threshold is illustrated in figure 4.6, where a hypothetical surface separates regimes. The surface never cuts the $V_0/U_\infty = 1.0$ plane.

4.4.3 Effect of Varying Reynolds Number

The current parameter study considers a large parameter space defined by four variables. Within this, only a relatively small number of discrete parameter combinations can possibly be investigated. The Reynolds number, being associated with the crossflow, influences the speed at which vortices are convected downstream. Although only four values were considered for this study, there is evidence that the flow regime varies with Re. This can be seen in figure 4.7. For most combinations, the behaviour is regardless of Re. However, when $k_h = 0.05\pi$, and $V_0/U_\infty = 2.0$ or $V_0/U_\infty = 3.0$, the nature of the flow changes as Re is altered. It therefore seems reasonable to assume that for some values of reduced frequency, the presence of a recirculation region may crucially depend on the Reynolds number. In figure 4.7 and when $k_h = 0.05h$, the flow behaviour changes from transitory to the establishment of recirculating regions for $V_0/U_\infty = 2.0$, and from individually convected vortices to recirculating regions when $V_0/U_\infty = 3.0$. Based on these cases it is concluded that decreasing the Reynolds number promotes the establishment of a permanent recirculation bubble. This is consistent with expectations, the lower Reynolds number implies a higher ratio of jet momentum to freestream momentum.

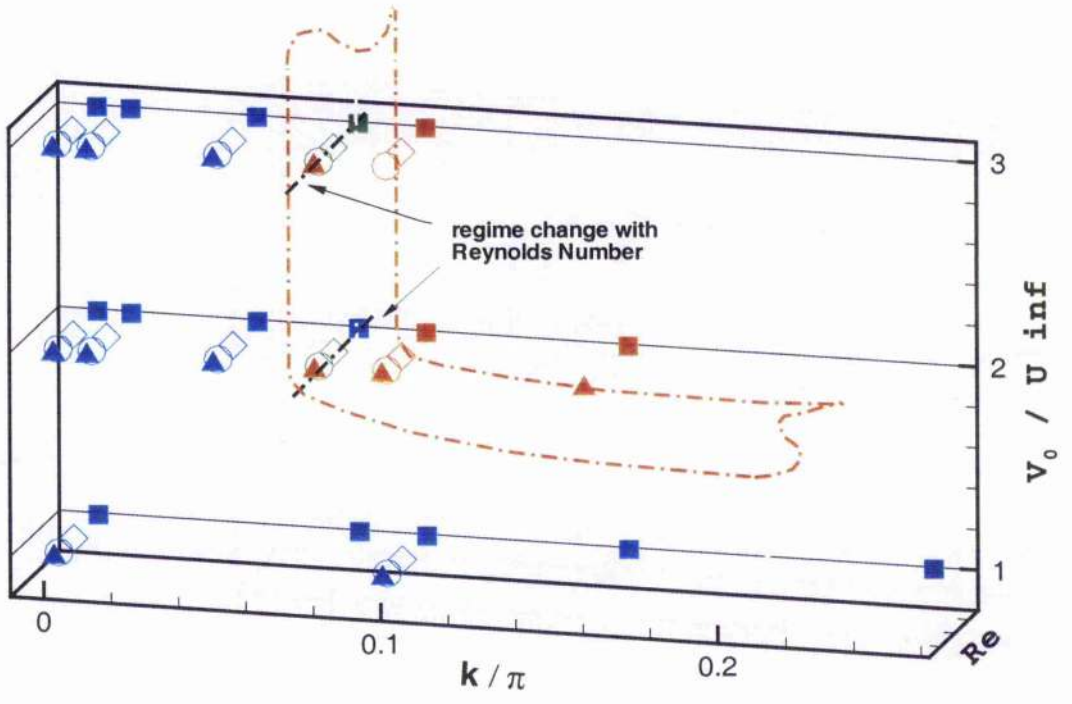

Figure 4.7: **Effect of Reynolds Number** , $x_{le} = 600h$; *blue* indicates individually convected vortices; *green* where convection is slow so that the disturbance remains local; *red* indicates that a permanent recirculating region is established. □.. Reynolds number $Re_h = 350$; ◇.. $Re_h = 700$; ○.. $Re_h = 1750$; △.. $Re_h = 3500$. Black (dotted) lines highlight two situations where a regime change is provoked solely by altering the Reynolds Number Re.

4.4.4 Effect of Varying δ

The parameter study has so far considered the effect of varying V_0/U_∞, Re_h and reduced frequency k_h when the actuator is issuing into a thick boundary layer. This boundary layer was generated using values $x_{le} = 200h$ and $x_{le} = 600h$, to give a constant nominal boundary layer thickness δ. In determining which regime is established, the reduced frequency k_h was found to have the greatest influence. In this section the parameter study is extended to examine the effects of varying x_{le}, hence to investigate the actuator's operation when δ is considerably smaller and therefore more representative of conditions close to the leading edge of a helicopter rotor blade.

It has been noted in section 4.3.3 that changes in regime due to Re_h variation occurred for only a small number of parameter combinations. In mind of this, for initial experiments with varying x_{le} the Reynolds number is given a constant value $Re_h = 350$. It has also been found that over the parameter space considered so far, V_0/U_∞ had little influence on the flow regime, so long as it was sufficient to introduce vortices persisting longer than the actuator period, consequently a single value, $V_0/U_\infty = 3.0$ is used here. The experiments of this section extend the previous work to include the variation of reduced frequency k_h when $x_{le} = 20h$, $40h$, $100h$ and $200h$.

The emphasis of this section is again on the production of recirculating regions. In figure 4.7, when $x_{le} = 600h$, a recirculating region was always permanently established when $k_h = 0.1\pi$. With $Re = 350$ this occurred at $k_h = 0.08\pi$. Experiments with varying x_{le} were conducted, seeking at each value x_{le}, to identify the range of k_h over which a change of regime occurs. Results are plotted in figure 4.8. An obvious trend can be seen in the figure. As x_{le}, and therefore the boundary layer thickness δ decreases, the reduced frequency k_h, required to produce a recirculating region is increased.

4.4.5 Summary

Predetermining the flow behaviour from the freestream and operating parameters is important in that each state, localised recirculating regions or individually convected

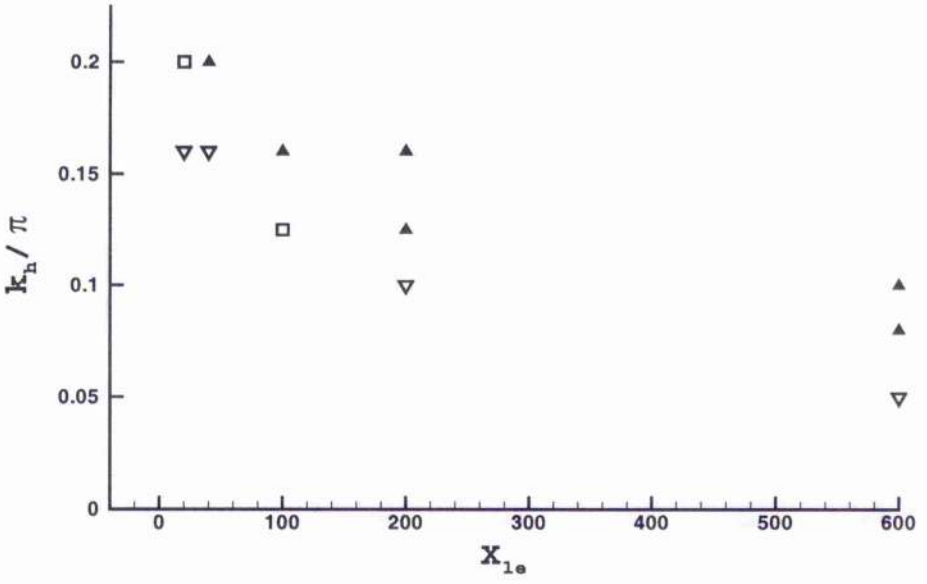

Figure 4.8: **Effect of** x_{le}, ∇ indicates individually convected vortices; $\square$ where convection is slow so that the disturbance remains local; $\triangle$ indicates that a permanent recirculating region is established.

vortices, represents a different control approach.

Either flow regime is capable of improving fluid mixing. Individually convected vortices achieve this over a greater downstream distance and with less peak to peak pressure variation. The permanently established recirculating regions produce a greater mean modification of the flow boundary, i.e. an alteration of the 'effective aerodynamic shape'.

Since the actuation period is greater for individually convected vortices, and the convected distances are greater, the instantaneous position of each vortex may have a heightened importance. This may especially be the case for flow control applications where time scales are small, as in dynamic stall for example. In this chapter the effectiveness has been quantified in terms of mean surface pressure reduction. For the conditions which have been studied, it is especially noticeable when altering the reduced frequency, that minimum cycle averaged surface pressures coincide with the first occurence of permanently established recirculation regions, i.e. the transition boundary between the two regimes marks the conditions where the actuators have most effect.

Given the importance of the difference between regimes and the importance of the boundary which separates them, the parameter study in this chapter has sought to determine the conditions under which each exists. This used an imposed velocity boundary condition model and considered in particular the flow behaviour with varying Reynolds number Re_h, reduced frequency k_h and distance from the leading edge of the flat plate in which the actuator is set, x_{le}. This last parameter scales with the boundary layer thickness δ.

It is emphasized that in this chapter, some parameter combinations lie outside the range which has previously been considered. The use of a velocity boundary condition implies that this approach can produce the same flow behaviour as a deforming cavity. For cases having higher Reynolds numbers however, further validation of this point is desirable.

Three values of the velocity ratio were used, $V_0/U_\infty = 1.0$, 2.0 and 3.0. With $V_0/U_\infty = 1.0$, only individually convected vortices were produced. Across the rest of the parameter field, there was evidence to show that increasing the jet velocity

promoted the occurence of a permanent recirculation region.

A range of reduced operating frequencies between $k_h = 0.0025\pi$ and $k_h = 0.3125\pi$ were considered. With the other parameters held constant, there is a critical value of reduced frequency, below which vortices produced on the downstream side of the actuator (whose scale decreases with increasing k_h) are individually convected downstream. As this value is approached, the motion of these vortices is impeded by the suction part of the cycle. Above the critical value, the vortices instead feed into a recirculating region which forms downstream of the actuator exit. Further increases in reduced frequency cause this bubble to reduce in size and to move upstream towards the actuator exit. The threshold between these regimes was found to greatly depend on the location of the actuator relative to the leading edge, hence on the boundary layer thickness. Moving the actuator progressively towards the leading edge (into a thinner boundary layer), the reduced operating frequency required to produce a recirculation region is found to rise exponentially.

Increasing the distance of the actuator from the leading edge of the flat plate, thereby increasing the boundary layer thickness, was also found to promote permanent recirculation regions. Distances of $x_{le} = 20h$, $40h$, $100h$, $200h$ and $600h$ were considered. The trend established suggests that transition between regimes requires high reduced frequencies if the actuator is close to the leading edge.

Across the range of conditions investigated, i.e. $Re_h = 350$ to 3500, decreases in Reynolds number were found to promote the establishment of a recirculating region. It should be noted that Reynolds numbers are up to an order of magnitude greater than those of the previous chapter. Further validation of the velocity boundary condition actuator against a deforming cavity type actuator at higher Reynolds numbers is therefore desirable. Similar trends were observed for each value of Reynolds number used, providing some confidence.

The acoustic impact of an actuator having an exit width $h = 0.5mm$, and operating in an environment described by a Reynolds number $Re_h = 350$ was discussed. Sound pressure levels were around $70dB$ at a distance of $5m$ from the actuator.

In the next chapter, the synthetic jet will be embedded in the surface of an aerofoil. The work of the current chapter will be used to make initial estimates of actuator

operating conditions. The aerofoil will test the above findings in a context which is more representative of a flow control application.

Chapter 5

Synthetic Jet Enabled Aerofoil

5.1 Overview

The work described until now has been aimed at better understanding the local effects of synthetic jet actuators. The aim however, is to investigate potential benefits of actuation to aerofoil performance. Just as it is necessary to show that all of the main features of cavity generated flow can be simulated by means of imposing a velocity boundary condition, it is also essential to demonstrate that all the features and trends for flow developed over a flat plate can be similarly produced at desired locations on the surface of an aerofoil. The aerofoil introduces the additional factor of surface curvature, and consequently of pressure gradient. In this chapter, a jet enabled aerofoil is considered when the actuator is operated at discrete values of reduced frequency, k, and in freestream conditions where the jet performance on a flat plate is already known. The intention is to determine whether similar structures are produced and similar regimes become established.

It has been emphasised in the synthetic jet literature that the creation of permanently established recirculating regions may offer an alternative flow control mechanism to the simple fluid mixing and re-energising provided by the convection of vortical structures. In the literature, changing the effective aerodynamic shape has been described as an alteration of the bounding streamline. The implication is that the flow is re-routed, and the distribution of streamlines is altered.

By definition, the bounding streamlines run between the stagnation points at the

leading and trailing edges, fitting the geometry exactly. Strictly, the bounding streamlines cannot be altered without a physical deformation of the body itself. In the synthetic jet literature however, an alternative definition is implied by which the bounding streamline encompasses closed recirculating regions produced by the actuator. The duality of definition arises, and has gained acceptance, since a closed recirculation region has both separation and reattachment points which coincide with the bounding streamline. This issue is discussed here to emphasize that the production of recirculation bubbles and streamline displacement are interdependent. Importantly, significant mean streamline displacement cannot be achieved by individually convected structures produced from a synthetic jet as have hitherto been described. For this, the production of permanent recirculation bubbles is necessary.

Remembering that 'zero-mass' actuation is being considered here, any useful virtual thickening of the body in which the actuator is embedded, i.e outward streamline displacement, requires that a recirculation region having constant location be established. Figure 5.1 illustrates that although an uneven mean exit profile may disrupt the streamline distribution in its vicinity, the net mass bounded by streamlines remains the same. Figure 5.2 shows that when a recirculation region is established, a relatively steady streamline displacement may be achieved.

The presence of a recirculation bubble on the pressure surface of the aerofoil and in the vicinity of the leading edge, may be thought of as increasing the 'virtual' camber. A known effect of physical camber on an aerofoil section is that this increases the lift at any pre-stall angle of attack. Stall when it occurs however, may be at lower incidence than for a similar uncambered section as shown in figure 5.3. For the helicopter application, the maximum achievable lift is the most important criteria. The disadvantage of physically cambered aerofoil sections for helicopter rotors is their poor performance whilst the blade is advancing. A virtual camber may therefore provide the advantages of camber without the drawbacks.

For the cases discussed here the angle of attack has been set to a fixed, i.e. static, value. For helicopter rotors, plunge motion and therefore variation in the effective angle of attack due to the aerodynamic loading is opposed only by the centrifugal force on each blade. The centrifugal force resultant acts normal to the rotation axis and is relatively constant for a given rotation speed. The net aerodynamic forces

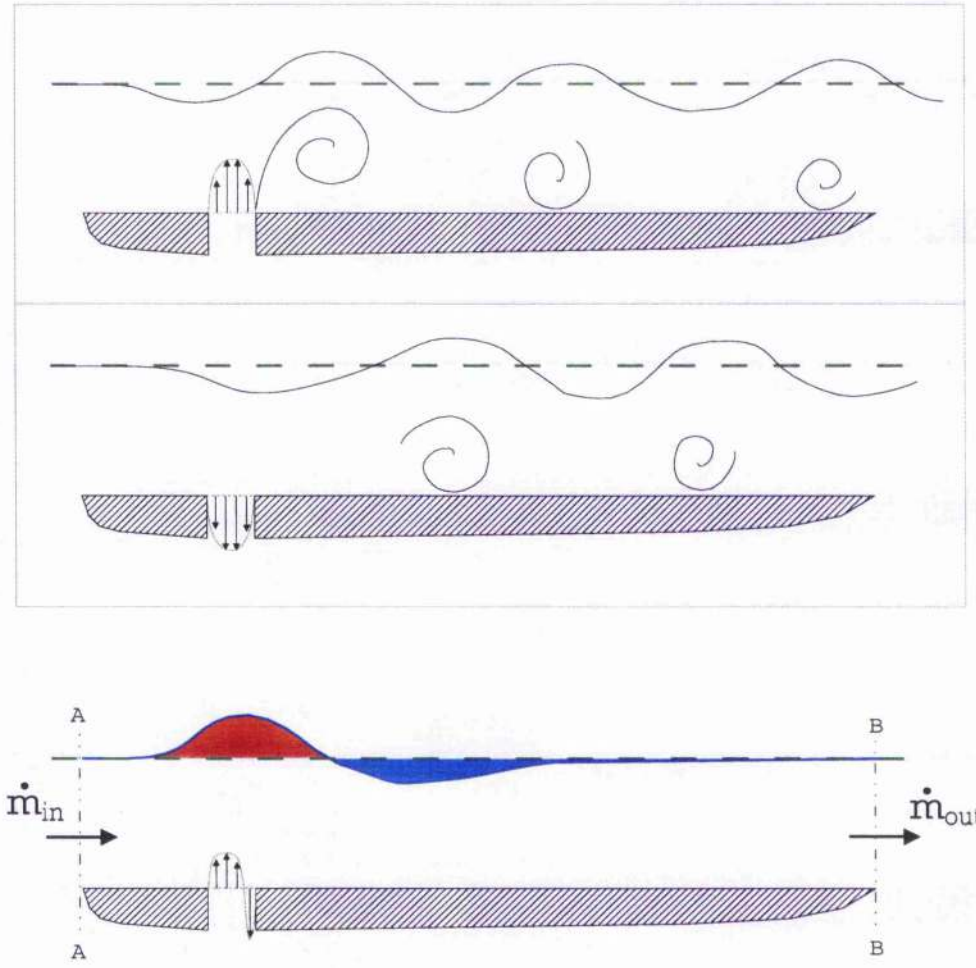

Figure 5.1: **Illustration of Individually Convected Structures**
top and middle: Flow behaviour is illustrated at two instants of the actuator cycle; during blowing and during suction. The actuator produces vortical structures which are subsequently convected across the downstream surface. A nominal streamline is shown in green. Ingestion and ejection of fluid to and from the actuator cause streamlines to be alternately pulled towards then pushed away from the surface. **bottom:** Mean flow behaviour. Streamlines may be disrupted by actuation but since the actuation introduces zero fluid, $\int_T \dot{m}_{in} dt = \int_T \dot{m}_{out} dt$, then the net displacement is small. For an incompressible flow, there is no net displacement, i.e. the red and blue regions in the figure have the same area.

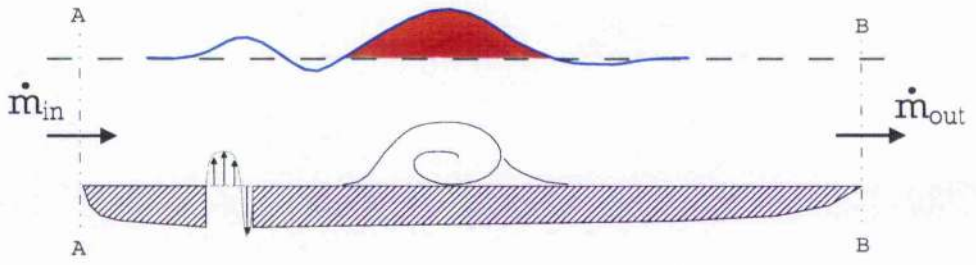

Figure 5.2: **Illustration of a Recirculation Bubble**, Streamlines are displaced depending on the volume of the recirculation bubble.

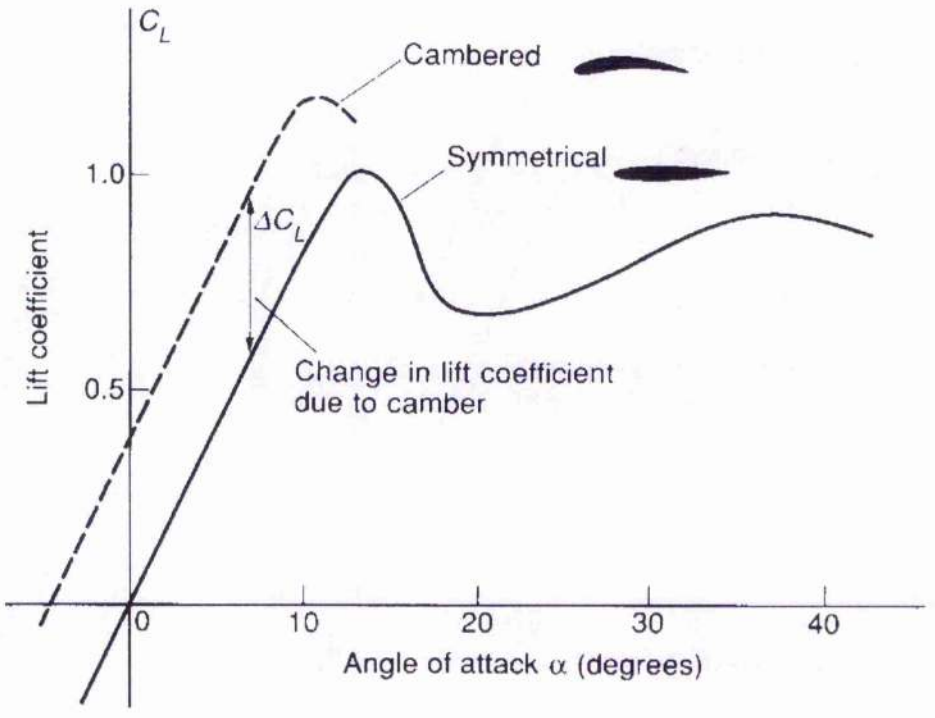

Figure 5.3: **Effect of Aerofoil Camber on Lift Stall**

can be described by lift, drag and pitching moment coefficients, C_l, C_d and C_m. The presence of an actuator whose operation involves suction and/or blowing however, introduces another force. Transfer of momentum from the actuator to the jet fluid incurs a reaction loading opposite to the jet thrust. The magnitude of the thrust (per unit span) is,

$$T_{jet} = \int_h \rho_{exit} v_{exit}^2 \, ds \tag{5.1}$$

With the sense in the direction of the exit velocity. The jet effort T_{jet}, non-dimensionalised by the characteristic length scale and by the freestream dynamic pressure is often referred to as the momentum coefficient, C_μ. In the actuated case, the jet thrust T_{jet} and its effect on the rotor blade can be considered as having components in the directions of lift and drag.

The interest of this work is in improving the pre-stall aerofoil behaviour. This not only encompasses increasing the pre-stall aerodynamic lift, but the net force in the direction of lift (i.e. normal to the freestream velocity). Considering the aerodynamic lift in steady freestream conditions and at fixed angle of attack, any increase ΔL is induced by the operation of the actuator. However, it is possible that the cost of the C_l improvement in terms of momentum transfer, means that the net force is actually reduced. Therefore, the momentum transfer has to be taken into account when seeking to show real improvements.

The next section describes the CFD formulation of a synthetic jet actuator embedded in a NACA-0012 aerofoil. Numerical tests designed to show that the solutions are independent of the grids on which they have been generated are then described. Comparisons are then made with published data. Suitable data for an actuator enabled aerofoil is not available and so only the static stall of an un-actuated section is considered. These sections are followed by results and evaluation of actuator enabled cases. First actuation is considered on the aerofoil set at zero angle of attack. Then in independent sections the aerofoil is considered pitched nose-down so that actuation occurs on the pressure surface and then pitched upwards so that this is on the suction surface. In both situations the aerofoil is at incidence close to stall.

5.2 Numerical Formulation

5.2.1 Grids and Boundary Conditions

For the current numerical experiments, it is required that the grid density around an aerofoil is sufficient to represent the flow from an actuator on its surface. Such a grid is created here essentially by the synthesis of an aerofoil and an actuator-enabled plate as used in the previous chapters. The grid density required to simulate a synthetic jet actuator which is embedded in a flat plate and set in a crossflow has been investigated in chapter 3. A grid density and distribution capable of representing the behaviour of flow around a clean NACA-0012 aerofoil is established in this chapter by performing numerical tests and by comparing with published data. Three aerofoil grids are used specifically for the purpose of clean aerofoil grid dependence tests. These are grid A, which is a C-type grid, and grids B and C which have been produced from grid A by successively removing every second point in each direction. Grid C is shown in figure 5.4. Grids A, B and C are each comprised of three blocks, i.e. two downstream blocks and one which surrounds and defines the aerofoil.

A fourth grid, grid D, has been developed from the finest aerofoil grid (i.e. grid A) and is used for actuator-enabled aerofoil experiments. In the design of grid D, the exact distribution employed in the vicinity of the actuator for the flat plate cases of the previous chapter was taken, and in both the surface-normal and surface parallel directions, applied on the aerofoil. The actuator is modelled at a location $x/c \approx 0.05$, and has an exit width of $h/c = 0.0025$. Experience gained from the experiments of the previous chapters was used to decide on the extent of uniform distribution both fore and aft of the jet exit. Grid D is otherwise similar to grid A. The use of the multiblock approach however, means that grid concentration at the actuator location forces more extensive grid density increases elsewhere. Grid D is illustrated in figure 5.5. This is made up of five blocks, since the block which nominally surrounds the aerofoil has been divided into three to allow definition of the actuator exit. Grids A to D used in this chapter are summarised in table 5.1.

In the absence of published data for an actuator enabled case, validation is sought using aerodynamic coefficient data (C_l, C_d and C_m) which has been published for

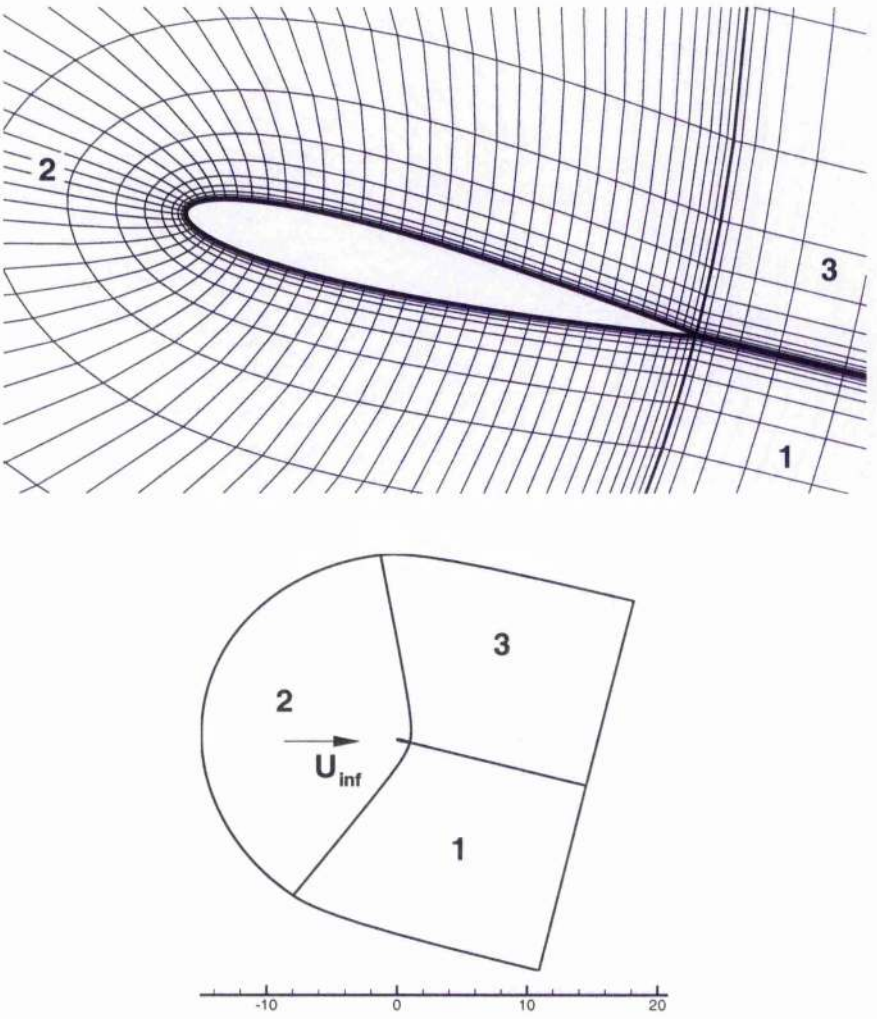

Figure 5.4: **Aerofoil Grid , top:** Grid C represents a (symmetrical) NACA-0012 geometry using a symmetrical grid distribution. The grid comprises three blocks as indicated, a body conforming block (block 2) and two downstream blocks (blocks 1 and 3). The aerofoil is shown pitched to an angle of attack, $\alpha = 14^o$, achieved by rotating the entire mesh. **bottom:** Block boundaries show the extent of the far field. Block numbers and the direction of the freestream are also indicated.

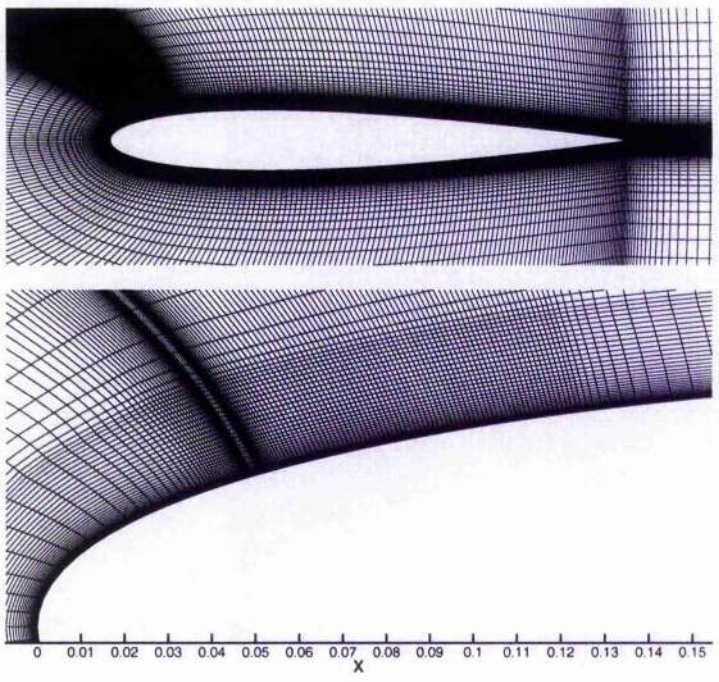

Figure 5.5: **Synthetic Jet Enabled Aerofoil Grid**
top: Aerofoil Grid D, **bottom:** close up of the aerofoil leading edge showing only every third vertice in each direction. The simulated actuator exit is located at $x/c \approx 0.05$ and grid density is maintained some distance downstream of this. The actuator is represented by an independent block, i.e. the block topology is as shown in figure 5.4, but with block 2 divided into three, making five blocks in total.

GRID	AEROFOIL	DOWNSTREAM BLOCKS
grid A	289 x 97	49 x 97
grid B	145 x 49	25 x 49
grid C	73 x 25	13 x 25
grid D	632 x 120	49 x 120

Table 5.1: Summary of Aerofoil Grids

.

a statically stalling NACA-0012. This is available over a range of incidence α. To obtain comparative CFD data, a sinusoidal pitching schedule was used, described by,

$$\alpha(t^*) = \alpha_m + \alpha_0 sin(2k_{foil}\ t^*) \tag{5.2}$$

where α_m is the mean angle of attack, and α_0 is the pitching amplitude. For all of the pitching cases discussed in this chapter, the centre of rotation is at the quarter chord, $x/c = 0.25$.

In equation 5.2, k_{foil} is the reduced frequency of aerofoil pitching. In previous chapters, the reduced frequency of actuation was based on the actuator exit width, h, and denoted k_h. For synthetic jet enabled aerofoil cases, the aerofoil chord, c, provides another length scale and it is convenient in this chapter to scale the actuation according to this. The reduced frequency of actuation is therefore defined as,

$$k_c = \omega c/(2U_\infty) \tag{5.3}$$

Given that $h/c = 1/400$, then the equivalent reduced frequency based on actuator exit width h is $k_h = k_c/400$.

From the computational experiments of previous chapters which consider an actuator set in a flat plate, operating frequencies need be of the order of $f = 10^4 Hz$ to produce permanently established recirculating bubbles. A typical helicopter rotor blade has a rotational frequency of around $f = 10Hz$. The difference between the

time-step required to model a pitching rotor blade and that required to model a synthetic jet actuator makes it impractical to model an actuator-enabled blade section over any useful portion of the pitching cycle. Previously, 200 time steps have been used to model each actuation cycle although it has been shown that 100 may be sufficient. If, for example, an actuator operates at $f = 10^4 Hz$ on a blade rotating at $f = 10Hz$, then there are 1000 actuator cycles per rotation, each requiring 100 time steps. In this chapter, actuation is instead considered on an aerofoil at fixed angles of attack only. The approach taken for high angle of attack jet enabled aerofoil cases, where actuation is employed at conditions close to (static) stall, is to slowly pitch the aerofoil section from an initial angle of attack at which the flow is fully attached. During this process there is no actuation. Results are then obtained at incidence close to stall. These results are then used as initial solutions for subsequent jet-enabled computations, during which the angle of attack is maintained constant.

On the aerofoil surface, except at the actuator exit, normal wall boundary conditions are applied. These include a velocity correction in order to maintain the no-slip condition for moving geometries. The time-varying actuation is again represented by imposing sinusoidally varying velocities. Across the actuator, the velocities are given by,

$$V(\acute{x}, t) = V_0 \sin^2(\pi \acute{x}/h) \sin(\omega t) \quad \text{for} \quad 0 \leq \acute{x} \leq h \tag{5.4}$$

where $\acute{x}$ is the distance along the actuator exit plane and ω is based on the frequency of actuation. If $\tan(\beta)$ is the gradient of the actuator exit plane then,

$$u(\acute{x}, t) = \pm V(\acute{x}, t) \sin(\beta) \quad \text{and} \quad v(\acute{x}, t) = V(\acute{x}, t) \cos(\beta) \tag{5.5}$$

This ensures that regardless of the angle of attack, the jet velocity acts normal to the exit plane.

Freestream conditions are applied on all exterior boundaries except for those facing downstream. On the downstream boundary, the pressure is set to a freestream value whilst the velocities and density are extrapolated linearly from the interior.

In this chapter, synthetic jet flow is simulated on both the pressure and suction surfaces of a pitched aerofoil. To achieve this using the same aerofoil grid for each

case (grid D), the aerofoil is pitched nose-up for suction surface actuation, and nose down for pressure surface actuation. To directly compare the results from each configuration, lift data is taken to be positive downwards for nose-down cases, and the sense of angle of attack and pitching moment is reversed. Pitching downwards with the actuator positioned on the upper surface then has the same result as turning the (symmetrical NACA-0012) aerofoil upside-down, and pitching upwards with the actuator on the underside. In the discussions which follow, figures illustrating the results of nose-down cases actually show a mirror image reflected about an axis aligned in the freestream direction, such that the aerofoil appears to be pitched upwards.

5.3 Numerical Tests

To determine a suitable grid density for actuator enabled aerofoil cases, tests were performed using grids A, B and C. These are successively coarser NACA-0012 grids described in section 5.2 . Driven by the results of this section, a fourth grid, grid D, was developed from grid A. Although grid D is also a symmetrical NACA-0012, the grid point distribution is asymmetrical about it's chord, having a clustered region to resolve small-scale structures arising from a synthetic jet which is modelled on its upper surface in experiments described in following sections. This section however, considers only unactuated performance.

Grids A,B and C were each used to perform a slow pitching aerofoil calculation. A pitching case was chosen for a number of reasons. It allows an investigation of grid resolution requirements over a range of incidence including that used in later jet enabled experiments. NACA-0012 aerodynamic coefficient data was available, and allows that the results of this section can also be used to compare with published data in the next. Considering the coefficients over a range provides a more complete test than using single values of Cl, Cd and Cm obtained at a particular set incidence.

The slow pitching test case was designed so that essentially static stall would occur. From a starting incidence of $\alpha_m = 9^o$ the simulated aerofoil is pitched upwards. With $\alpha_0 = 6^0$, the sinusoidal pitching schedule (equation 5.2) is followed until stall occurs. The pitching cycle has a reduced frequency of $k_{foil} = 0.001$. This was

CASE	GRID	TIME-STEP	PITCH DIRECTION
1	A	0.95	UP
2	B	0.95	UP
3	C	0.95	UP
4	B	0.475	UP
5	B	1.9	UP

Table 5.2: Summary of Calculations for Grid and Time-Step Studies

modelled on all three grids (cases 1, 2 and 3) using a time-step of $\Delta t^* = 0.95$. To investigate the effect of time-step variation, further cases were calculated on grid B using time-steps of $\Delta t^* = 0.475$ (case 4) and $\Delta t^* = 1.9$ (case 5). A Reynolds number of $Re = 1.4 \times 10^6$ and Mach number $M = 0.15$ were used throughout. All cases are summmarised in table 5.2.

Figures 5.6, 5.7 and 5.8, show C_l vs. α, C_d vs. α, and C_m vs. α respectively. For each of the criteria, there is a convergence of results with increasing grid resolution.

The effect of using different time-steps is seen in figures 5.9, 5.10 and 5.11 which again show C_l vs. α, C_d vs. α and C_m vs. α respectively. The computed data are generally in close agreement, meaning that significantly improved solutions cannot be achieved with the use of a yet smaller time-step.

5.4 Comparison with Published Data

The main interest of this chapter is in the potential use of synthetic jet actuators for the improvement of pre-stall lift of a NACA-0012 aerofoil. Currently, there is no experimental data available against which to compare the synthetic jet-enabled numerical experiments. Data is available however, for the clean NACA-0012 in a variety of flow conditions. The objectives of this section are first to use available data to further validate the use of the chosen grids and to demonstrate the suitability of pmb2d for this problem. Also, prior to considering the effects of actuation on a NACA-0012 aerofoil at static angles of attack close to stall, it is desirable to first

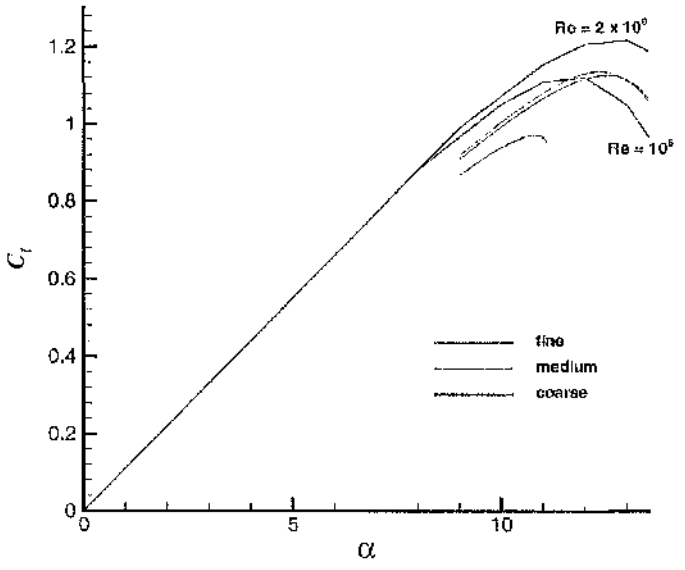

Figure 5.6: **Grid Density and Aerodynamic Lift Coefficient**, Results are shown as calculated on fine (case 1 - grid A), medium (case 2 - grid B) and coarse (case 3 - grid C) grids. Fine and medium grids show similar results. Also plotted are results described as a synthesis of experimental and computational data, published on http://www.maths.adelaide.edu.au/Applied/llazausk/

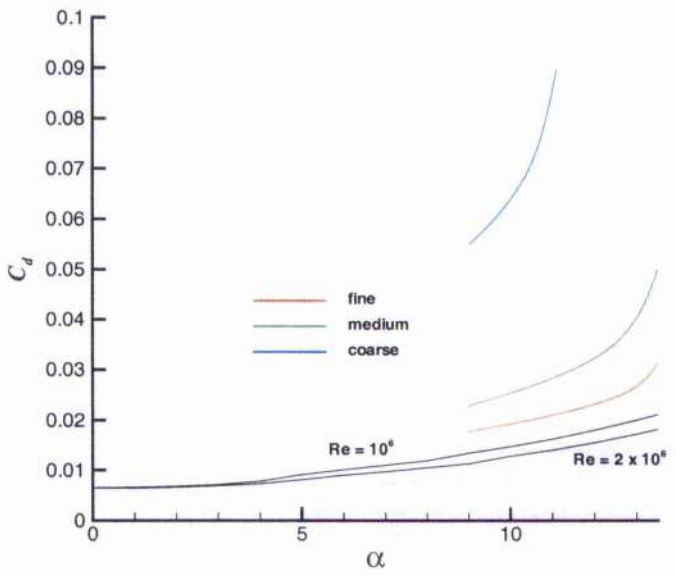

Figure 5.7: **Grid Density and Aerodynamic Drag Coefficient**, Results are shown as calculated on fine (case 1 - grid A), medium (case 2 - grid B) and coarse (case 3 - grid C) grids. Results from fine and medium grids are relatively similar given the C_d axis scale.

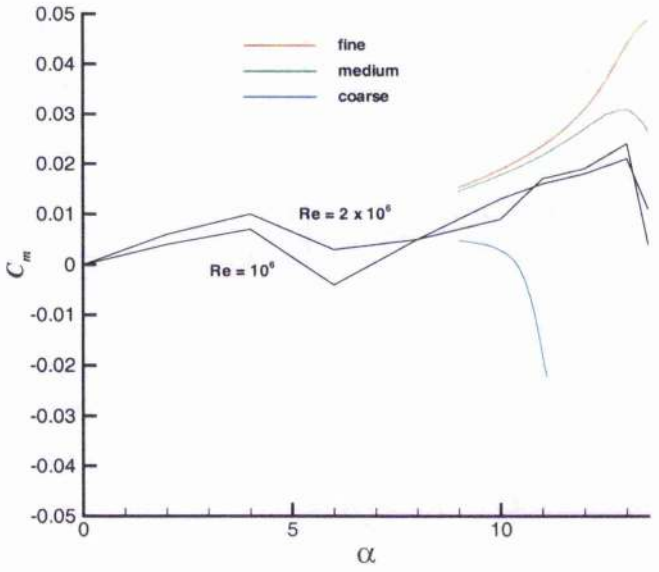

Figure 5.8: **Grid Density and Moment Coefficient**, Results are shown as calculated on fine (case 1 - grid A), medium (case 2 - grid B) and coarse (case 3 - grid C) grids. Results from fine and medium grids are in close agreement until around $\alpha = 12^o$. Coarse grid (grid C) results are quite different.

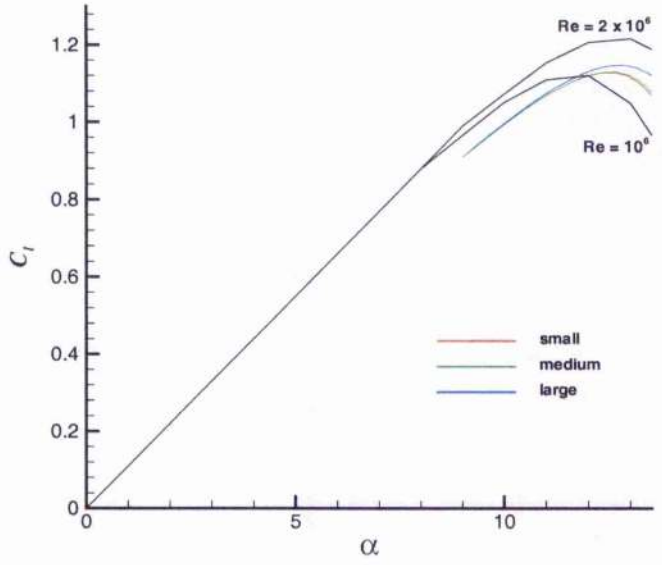

Figure 5.9: **Time Step and Aerodynamic Lift Coefficient**, Results are shown as calculated using small (case 4), medium (case 2) and large (case 5) time steps. These diverge only slightly at stall.

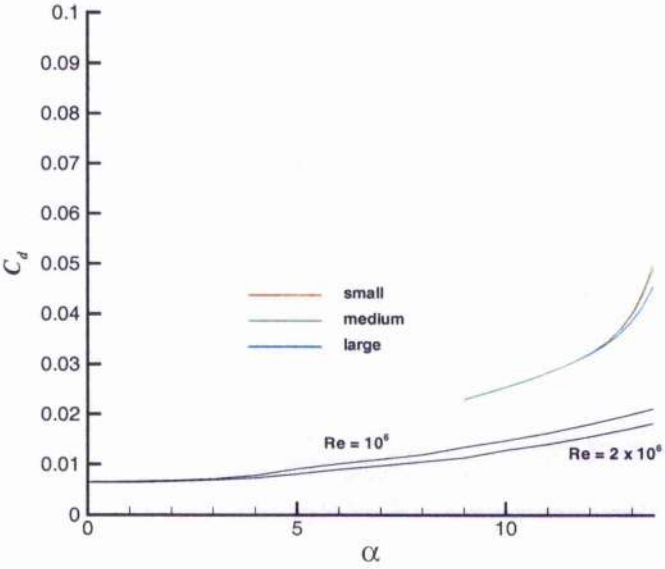

Figure 5.10: **Time Step and Aerodynamic Drag Coefficient**, Results are shown as calculated using small (case 4), medium (case 2) and large (case 5) time steps.

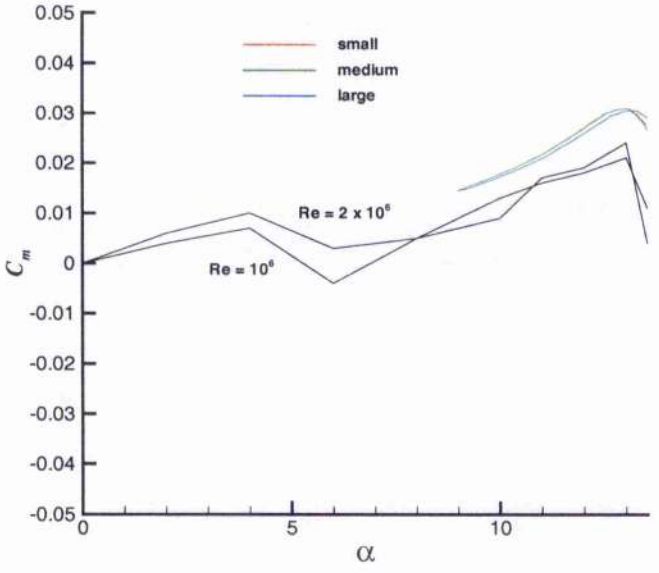

Figure 5.11: **Time Step and Moment Coefficient**, Results are shown as calculated using small (case 4), medium (case 2) and large (case 5) time steps. Once again there is similarity.

determine the (static) stalling angle, in order to define suitable cases.

The aerodynamic coefficients plotted in the previous section were achieved using a sinusoidal pitching schedule having reduced frequency, $k_{foil} = 0.001$. At such a low pitch rate, it is expected that the aerofoil will stall statically. In figures 5.6, 5.7 and 5.8, comparison is made with published data (www.maths.adelaide.edu.au/Applied/llazausk/) which is described as a synthesis of existing (computational and experimental) results. Results are given for a statically stalling NACA-0012 at Reynolds numbers, $Re = 10^6$ and $Re = 2 \times 10^6$. The current calculations have been performed at a Reynolds number of $Re = 1.4 \times 10^6$ and using a Mach number of $M = 0.15$. Over much of the pitching cycle, the lift coefficient, C_l, is generally lower (figure 5.6) than in the published data. Close to stall the results fall between the experimentally biased plots. Given the difference in freestream conditions between the current calculations and the published data, the stalling angle is well predicted on fine grids A and D.

Drag coefficients are higher for the current results. Case 1 (grid A) gives the closest comparison. A rapid increase in drag is observed at the far right of figure 5.7. This also occurs for the published results, but outside the angle of attack range shown in the figure. The moment coefficient is compared in figure 5.8. The chosen C_m axis scale allows a close inspection. Medium grid results give the best comparison.

Drag prediction is highly dependent on turbulence modelling, which is the subject of considerable CFD research effort. Aerodynamic forces on a body may be considered as pressure forces which act normal to the surface at every point, and shear stress which acts tangentially. For a typical aerofoil section at moderate or high Reynolds numbers, the production of lift relies overwhelmingly on creating a net pressure difference between upper and lower surfaces. The contribution of shear stress to the lift is small. The 'streamlined' shape of aerofoils is adopted to reduce pressure increases on aft facing surfaces, i.e. the intention is to reduce pressure drag. The elongated geometry provides greater surface area aligned in the drag direction however, and for drag, unlike lift, the shear stress provides a significant proportion of the overall force. The accuracy to which the shear stress is calculated therefore has a greater impact on the ability to predict drag force.

CASE	k_c	V_0/U_∞
6	$64\ \pi$	3.0
7	$125\ \pi$	4.5

Table 5.3: Summary of Jet-Enabled Cases at $\alpha = 0$

.

Most turbulence models based on the Boussinesque Assumption, including the standard $k - \omega$ model currently being used, employ coefficients which are optimised for particular flow situations. Although the model may provide useful results across a wide range of conditions, this depends on the sensitivity of each result (for example, lift, drag or shear stress) to these coefficients. Turbulence models are generally designed to be most accurate at some distance from the wall surface. However, the variation in boundary layer thickness and the severe gradients which may be experienced across it mean that within small distances, the fidelity of the model varies. This compromises the calculation of shear stress, which relies especially on near wall turbulence.

5.5 Jet Enabled at $\alpha = 0^o$

Before modelling on a pitched aerofoil, synthetic jet actuation was first tested on an aerofoil at zero incidence. Calculations were performed on grid D at reduced frequencies of $k_c = 64\pi$ and $k_c = 125\pi$. Imposed velocities were $V_0/U_\infty = 3.0$ and 4.5. The freestream conditions are defined by a Reynolds number, $Re_c = 1.4$ x 10^6, and Mach number $M = 0.15$. In each case, data from the tenth cycle is examined. The parameter combinations are listed in table 5.3

Figure 5.12 shows vortices being individually convected across the aerofoil surface at the start of the tenth cycle of the $k_c = 64\pi$ case. The spacing between these indicates their acceleration to the local flow velocity which is considerably in excess of the freestream velocity.

After ten cycles, the $k_c = 125\pi$ case was still not settled periodic. The calculation was continued for a further ten cycles after which time a recirculating region was

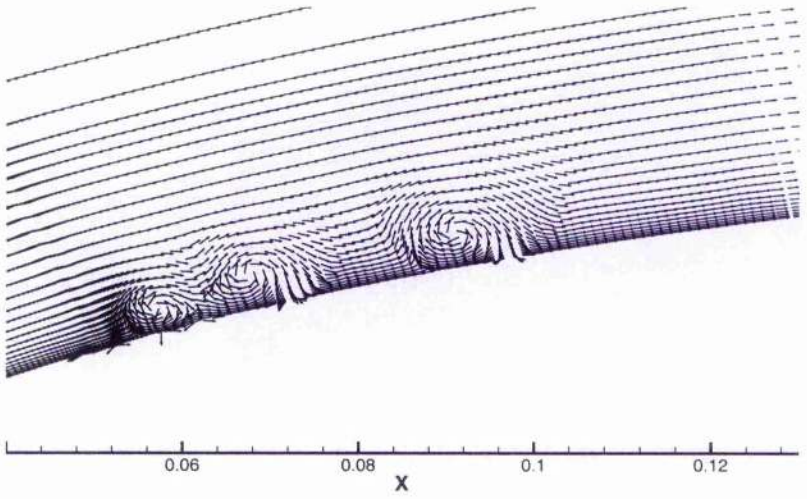

Figure 5.12: **Case 6, Flow Over Aerofoil Upper Surface**, grid D, $V_0/U_\infty = 3.0$ and $k = 64\pi$

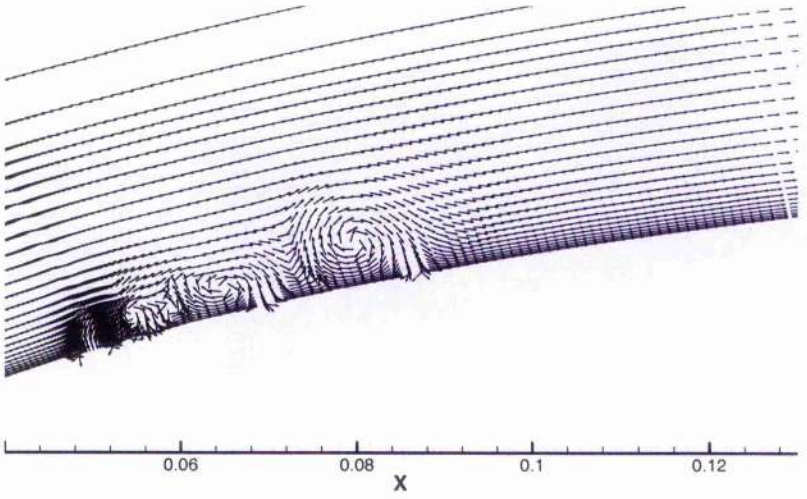

Figure 5.13: **Case 7, Flow Over Aerofoil Upper Surface**, grid D, $V_0/U_\infty = 4.5$ and $k = 125\pi$

observed, fed by the vortices from the actuator exit. This is shown in figure 5.13. The shape of this bubble was more rounded than those previously observed on a flat plate. Its location was not constant but rather it was found to move along the surface and back again in periodic fashion.

5.6 Actuation on Pressure Surface

This section investigates the operation of a synthetic jet actuator placed on the pressure surface of a pitched NACA-0012 aerofoil. Mechanisms by which a synthetic jet may exert a favourable influence, i.e. a suppression of stall or an increase of pre-stall lift, have previously been discussed. The establishment of recirculation bubbles by synthetic jets has been described as virtual shaping or changing the effective aerodynamic shape. It is generally known that separation from the suction surface of an aerofoil has a dependence on the radius of the leading edge and virtual shaping suggests a capability to actively modify the effective leading edge radius. The benefits of camber for pre-stall lift were discussed in the Overview section at the beginning of this chapter. Virtual shaping may make effective camber alteration possible. By a more conventional and familiar mechanism, the oscillatory action of the actuator re-energises the near wall flow by improving fluid mixing. The lift force is also directly affected by the jet thrust, however this is a crude and inefficient way to increase lift, and would not be used as the primary mechanism. The jet thrust is cyclical, and for a zero-mass jet, has a mean close to zero. In the current experiments, peak instantaneous values of thrust are relatively small.

To study the effects of a synthetic jet actuator embedded on the pressure surface of an aerofoil, grid D (figure 5.5) was used. The grid was pitched downwards to an angle of attack, $\alpha = -11.04°$. For this section, the sense of positive angle of attack, lift and moment coefficient are reversed. Discussions can therefore consider the aerofoil as though pitching upwards with actuation on the lower surface. An incidence of 11.04° is slightly below the nominal static stall angle. In this position, the actuator on the aerofoil's underside at $x/c = 0.05$ is also on the pressure surface. At this location, it can be seen from figure 5.14 that local velocities are considerably less than freestream. A freestream Reynolds number of $Re_c = 1.4 \times 10^6$ and Mach

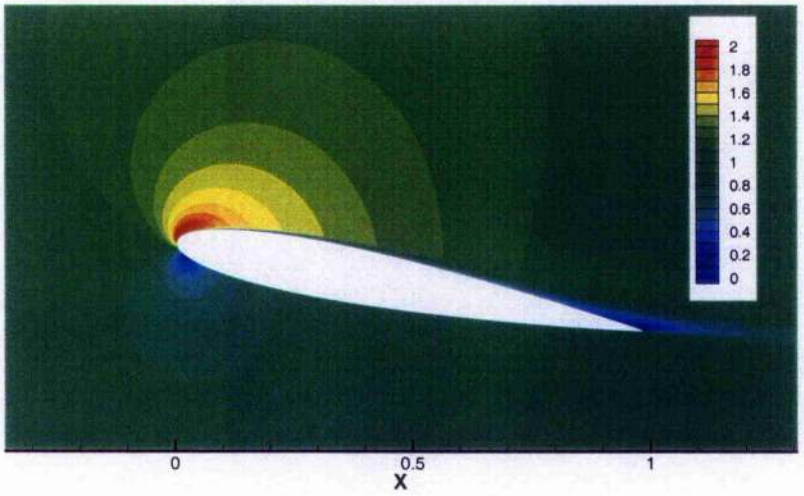

Figure 5.14: **Velocity Field for a Pitched NACA-0012**, Legend is of u/U_∞. At the leading edge, flow velocities are considerably higher than freestream on the suction surface, and lower on the pressure surface.

number $M = 0.15$ were used. The blowing effort used during actuation is quantified by the imposed velocity $V_0/U_\infty = 3.0$. Four cases were run in this configuration each differing only by the reduced frequency of actuation. In each case, 10 actuation cycles were performed. The reduced actuation frequencies were $k_c = 20\pi$, $k_c = 40\pi$, $k_c = 64\pi$ and $k_c = 80\pi$. The cases are summarised in table 5.4

Unit vectors indicate the flow direction in figures 5.15 to 5.18 and flooded contours show velocity magnitude. These are instantaneous snapshots obtained during the tenth cycle in each case. Figure 5.15 shows Case 8, which has actuation at a reduced frequency of $k_c = 20\pi$. The flow behaviour is clearly of the individually convected vortices type. This is confirmed in animated unit vector plots, i.e. where a number of instantaneous plots are viewed in succession to analyse the time-varying behaviour. Figure 5.15 also shows that except for the jet flow from the actuator, local flow velocities in its vicinity are significantly less than freestream. This is not attributable to the actuation, since low velocities are witnessed at this location for the baseline case also (figure 5.14).

In the succeeding unit vector plots (figures 5.16 to 5.18) only a single structure can

CASE	k_c	α
8	$20\,\pi$	-11.04^o
9	$40\,\pi$	-11.04^o
10	$64\,\pi$	-11.04^o
11	$80\,\pi$	-11.04^o

Table 5.4: Summary of Pressure Surface, Jet-Enabled Cases

be observed at any distance from the actuator exit. In the case of actuation at $k_c = 40\pi$, this vortex or recirculation bubble, has a relatively large, almost circular cross section. With increasing actuation frequency and therefore a reduced actuation period, the penetration of the jet into the primary flow is reduced and the structure becomes smaller.

Figures 5.16 to 5.18 can only show the flow behaviour at an instant. Animated unit vector plots which consider the behaviour through the entire (tenth) cycle, show that for each of these cases, the extent of the recirculation regions is relatively unchanging. Through the course of the cycle however, these move back and forth along the aerofoil surface.

The effect of the synthetic jet on the lift coefficient is shown in figure 5.19. In the figure, plots for each case are overlaid and the (horizontal) time axes are normalised to give a clearer comparison of C_l magnitude. The lift coefficient, C_l, in figure 5.19, has been calculated as the net effect of pressure on the exterior surface of the aerofoil. This excludes the jet exit. A lift component due to the jet thrust is also not included. Lift is found to be broadly sinusoidal in all cases. Variation from cycle to cycle is small after even the first actuation period, and significant changes are not anticipated after 10 cycles. Peak to peak fluctuation is smallest for the lowest reduced frequency case, $k_c = 20\pi$. It was demonstrated above (figure 5.15) that this case is of the individually convected vortices type. At some reduced frequency between that of case 8 ($k_c = 20\pi$) and case 9 ($k_c = 40\pi$), transition to the recirculation bubble type must occur. The maximum peak to peak fluctuation is for case 9, i.e. the lowest frequency case to have a permanently established recirculation

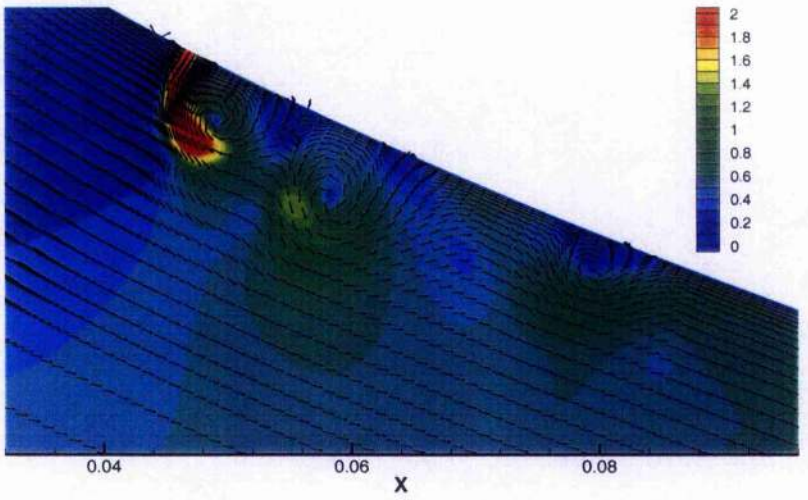

Figure 5.15: **Case 8, Unit Vector Plot**, grid D, $k_c = 20\pi$, Individually convected vortices travel along the pressure surface of the aerofoil. Flooded contours indicate velocity magnitude. Excepting the jet, flow velocities, especially upstream of the actuator are considerably less than freestream

region. The magnitude of variation appears to decrease with further increases in reduced frequency thereafter. This is a similar trend to that observed for streamline displacement in the last chapter, where the greatest displacement was found when a permanent recirculation region is first established.

In each case 8 to 11, C_l is for most of the time lower than even its nominal clean-aerofoil value. Cycle averaged mean values, which are also shown in figure 5.19, are consequently always less than for the unactuated case.

The mean pressure coefficient, C_p is plotted for all four cases in figure 5.20. The nominal (without actuation) C_p distribution is also shown (in green), and it can be seen that the actuator is positioned in a mildly favourable pressure gradient. In each of the actuated cases, the most significant departure from the baseline result is the mean reduction in pressure immediately downstream of the actuator exit (marked B in the bottom right frame of figure 5.20). This feature is associated with the mean reduction in lift seen in figure 5.19. Immediately aft, the mean pressure recovers abrubtly. In all cases the pressure at the aerofoil surface is then higher than the

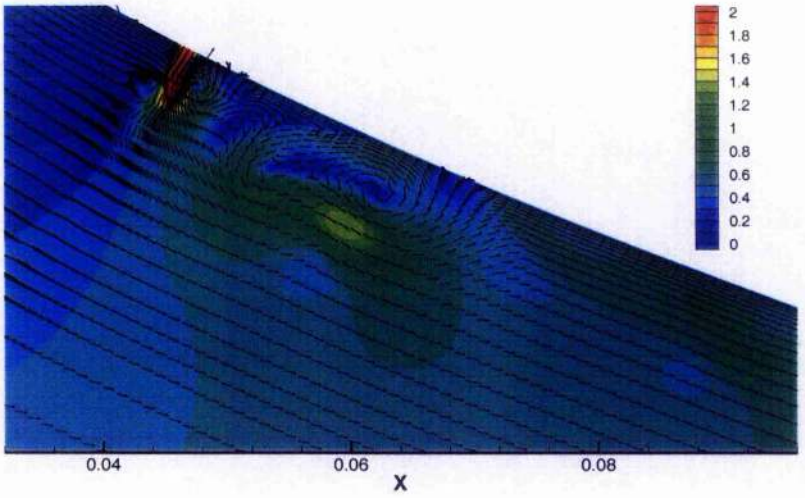

Figure 5.16: **Case 9, Unit Vector Plot**, grid D, $k_c = 40\pi$, Higher reduced frequency k_c, means a reduced actuation period. Comparing with case 8 (figure 5.15), despite the interval between events being reduced, only one major vortex structure is apparent here. This is a permanently established recirculating bubble. The flooded contours above, indicate velocity magnitude.

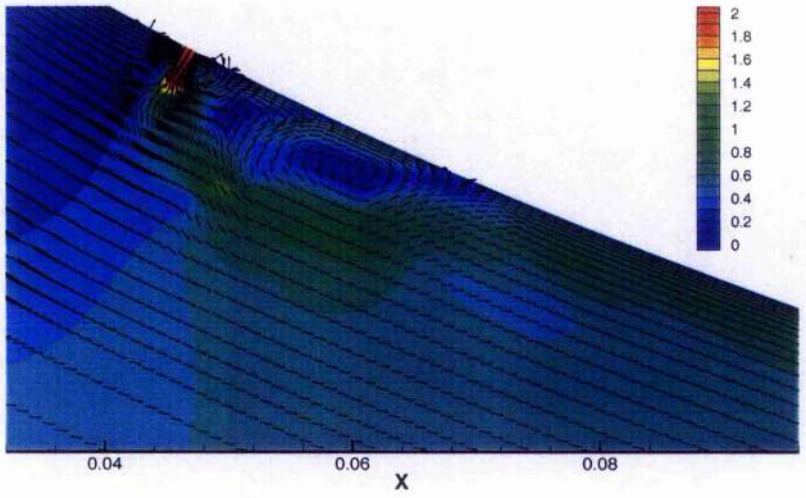

Figure 5.17: **Case 10, Unit Vector Plot**, grid D, $k_c = 64\pi$, The recirculating region has become more stretched out, however, its volume is maintained from case 9 (figure 5.16). Flooded contours indicate velocity magnitude.

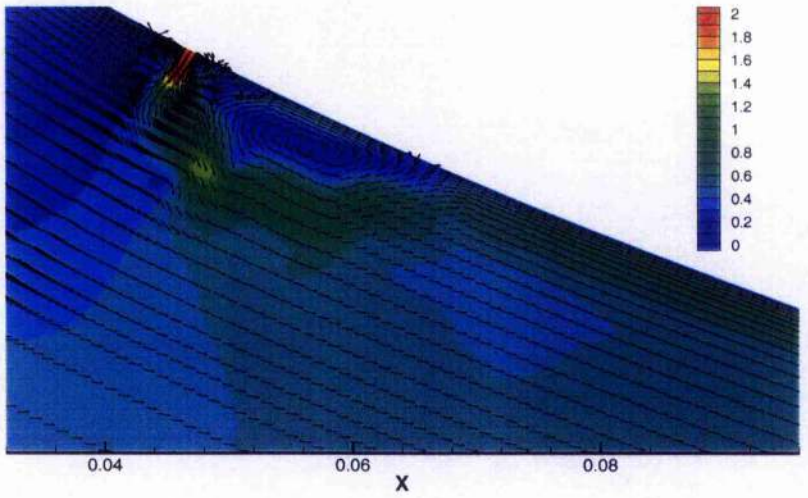

Figure 5.18: **Case 11, Unit Vector Plot**, grid D, $k_c = 80\pi$, The recirculating region is more stretched out and its volume is reduced. Flooded contours indicate velocity magnitude.

baseline for a short distance. This peak, marked C in figure 5.20, is of similar magnitude for all but case 8, the lowest reduced frequency ($k_c = 20\pi$) case, and the only one which displays the convecting vortices behaviour. The pressure recovery of case 8 ends instead with a peak of around half the size.

The mean plots of figure 5.20 indicate the net effect over a cycle, but they mask the scale of the instantaneous pressure variations caused by the actuator. Figure 5.21 shows the Cp distribution at five instants of the cycle for cases 8 and 9. The uppermost frames of figure 5.21, show the pressure distribution prior to peak blowing. Blowing from the actuator impedes the primary flow, causing a local pressure rise on the pressure surface ahead of the actuator. This corresponds to the C_l peaks previously seen in figure 5.19. On the pressure surface, a large fluctuation is apparent at the actuator exit. Pressure waves are produced directly by the actuation, i.e. by the repeated ejection and ingestion of fluid. These continue to be influential all the way to the trailing edge. In figure 5.21, directly generated pressure waves have a longer wavelength for the lowest reduced frequency case 8 ($k_c = 20\pi$), however the magnitude is greater for case 9 ($k_c = 40\pi$). Case 8, which is represented on the

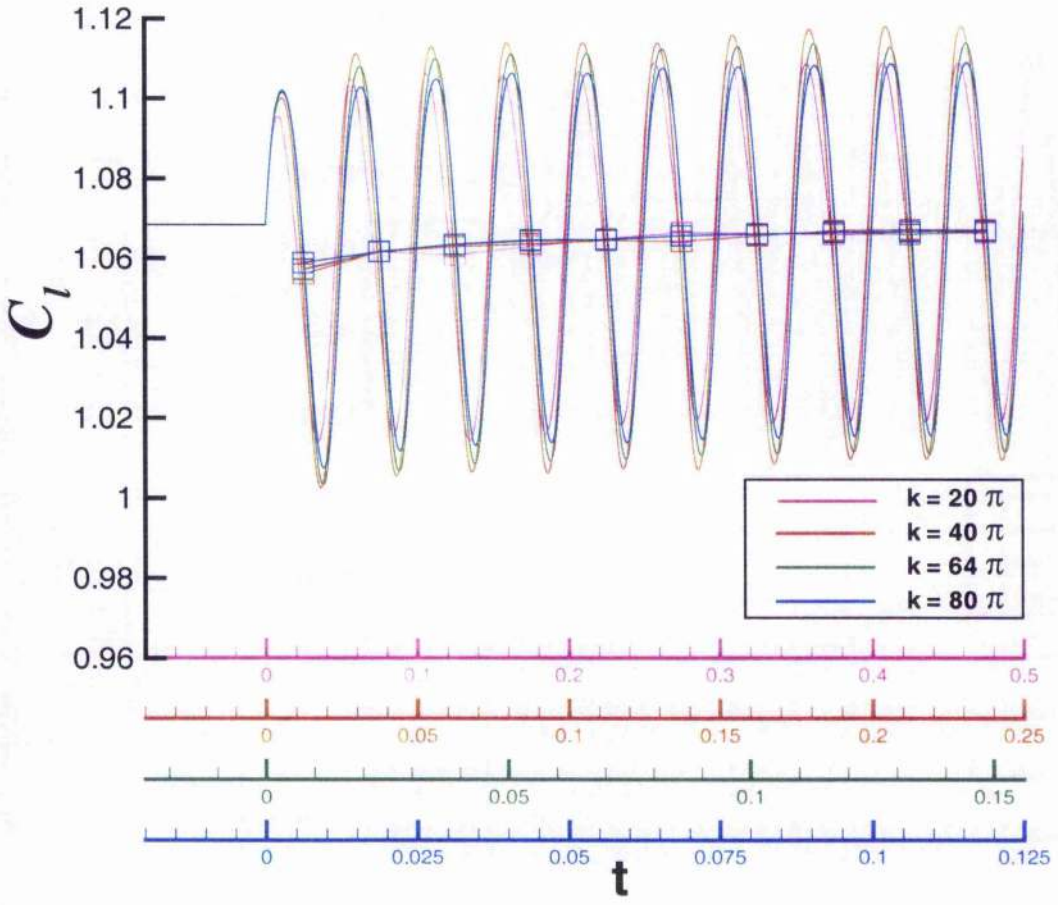

Figure 5.19: **Aerodynamic Lift Coefficient, Pressure Surface Actuation,** $\alpha = -11.04^o$, C_l is plotted for the four actuation schedules used on the pressure surface. Axes are normalised to allow comparison of C_l magnitudes. Mean values, computed over each cycle, are indicated by a '□' at the centre of each actuation period.

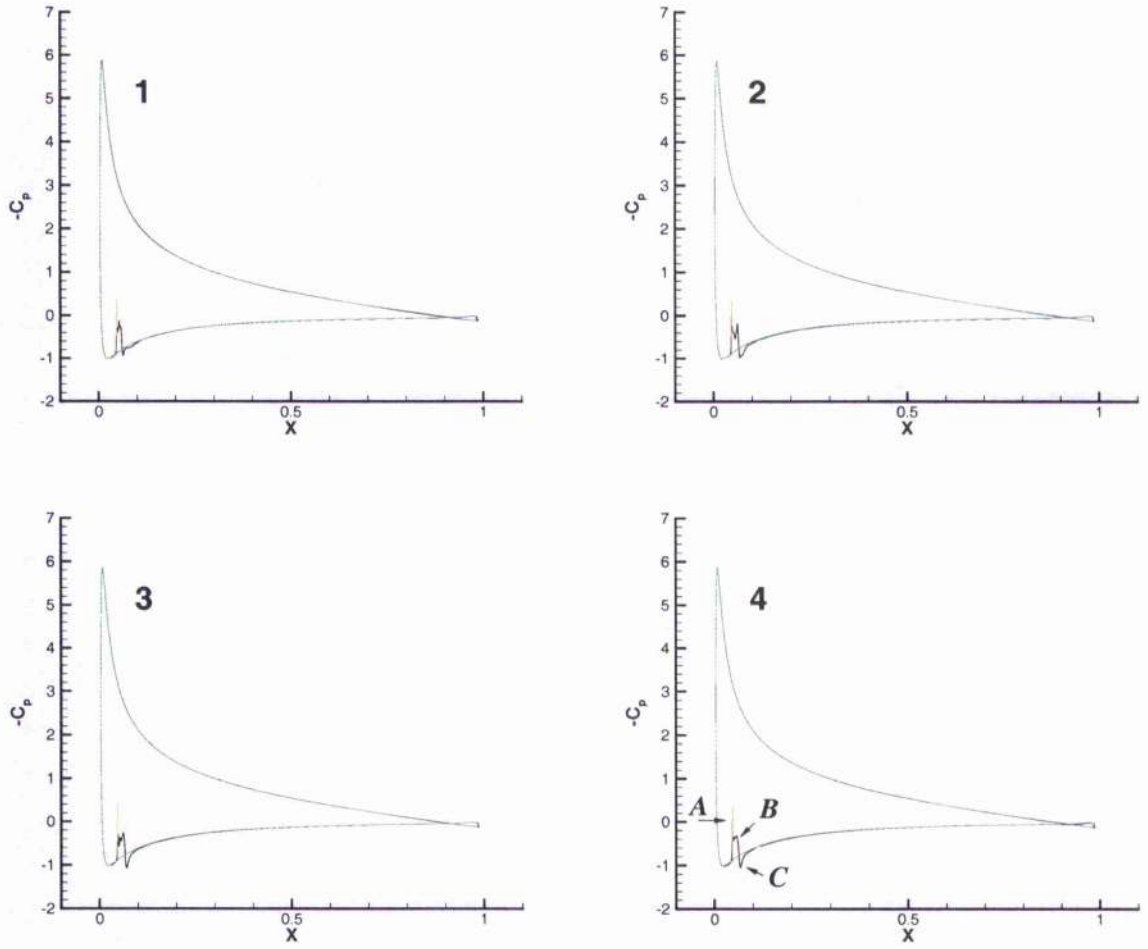

Figure 5.20: **Aerofoil Mean Pressure Distribution, Pressure Surface Actuation**, $\alpha = -11.04^o$, The distribution for actuated cases in shown in black, the nominal distribution in green. **top left:** case 8, **top right:** case 9, **bottom left:** case 10, **bottom right:** case 11. Aerodynamic lift is proportional to the area enclosed by the loop, **A** indicates the contribution to lift of the actuator thrust. This is in red. **B** and **C** are regions of reduced and increased pressure repsectively, which are characteristic of actuation on the pressure surface.

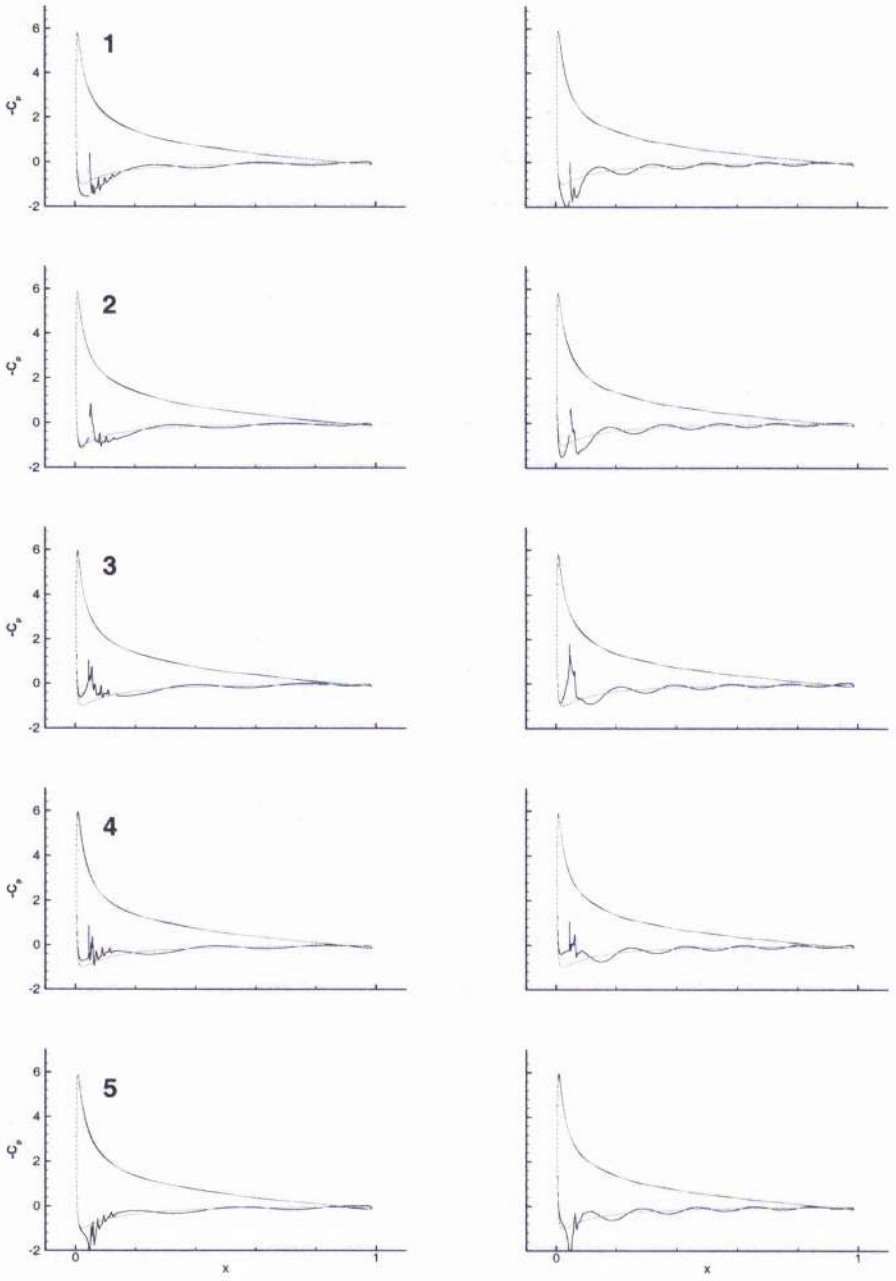

Figure 5.21: **Aerofoil Pressure Distribution at Instants of the Cycle**, The distribution for actuated cases is shown in black, nominal distribution in green. **left** $k_c = 20\pi$, **right** $k_c = 40\pi$, During blowing, there is a pressure rise both fore and aft of the actuator. During suction, the pressure falls. The actuator therefore acts as a pressure wave generator, the effect of which can be seen on the pressure distribution across the whole pressure surface. The five frames shown for each case are at equally spaced intervals of their respective cycles. The difference in reduced frequency, k_c, between cases is responsible for the different periods of the pressure waves.

left of figure 5.21 also has small pressure peaks which appear downstream of the actuator and which are imposed on the directly generated pressure waves. These are caused by convected vortical structures reducing pressures in their immediate vicinity.

The mean effect of the actuator on the pressure surface, is to reduce local pressures, and at this location, this is an adverse effect. On the suction surface, smooth pressure gradients are maintained.

5.7 Actuation on Suction Surface

This section investigates the operation of a synthetic jet actuator placed on the suction surface of a pitched NACA-0012 aerofoil. Grid D (fig 5.5) is again used. The grid was pitched upwards this time. Two angles of attack were considered, $\alpha = 11.04^o$ and $\alpha = 12.022^o$. Actuation at each incidence will be considered in turn.

5.7.1 Jet Enabled, Angle of Attack $\alpha = 11.04^o$

At an angle of attack of $\alpha = 11.04^o$, the aerofoil has the same incidence magnitude as used in the previous section. Since the NACA-0012 has a symmetrical profile, and since in the previous section, the direction of lift was taken to be positive downards, baseline results should be the same. The actuator, at $x/c = 0.05$ has the same location relative to the chord as before, however relative to an axis aligned in the freestream direction, it is slightly further aft. Freestream conditions were again, $Re_c = 1.4 \times 10^6$ and $M = 0.15$. Peak jet velocity was $V_0/U_\infty = 3.0$. Three cases were run with 10 actuation cycles. The reduced frequencies were $k_c = 40\pi$, $k_c = 64\pi$ and $k_c = 125\pi$. Cases are summarised in table 5.5

Figures 5.22 to 5.24 are unit-vector plots of the cases 12 to 14. As before, they are obtained during the tenth cycle just after the point of peak blowing. In each of the plots, individually convected vortices can be seen.

The figures are shown to the same scale as in the previous section (figures 5.15 to 5.18). It is clear that on the suction surface, the structures are considerably smaller than those observed on the pressure surface. Once again, with increasing

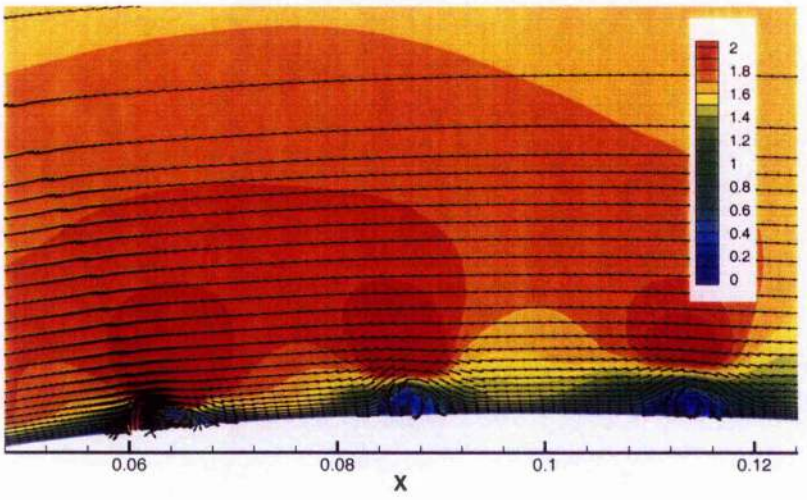

Figure 5.22: **Case 12, Unit Vector Plot**, Individually convected vortices traverse the upper surface of the aerofoil. These are considerably smaller than those seen on the pressure surface during similar blowing schedules. The axis shown, is aligned with the freestream and has a scale relative to the unpitched aerofoil. The location of the actuator relative to this axis is therefore different from earlier pitch-down cases.

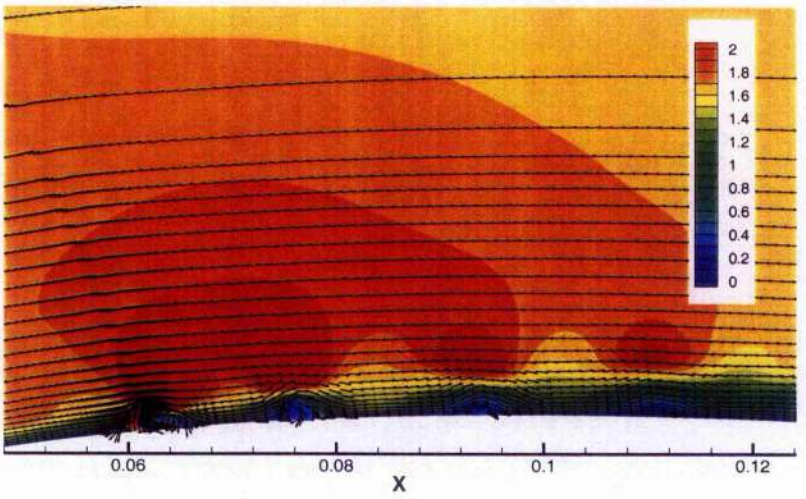

Figure 5.23: **Case 13, Unit Vector Plot**, The increase in reduced frequency k, and consequent reduction in actuation period, mean that the structures produced during actuation are smaller and less spaced. The reduction in scale also causes these to be short lived.

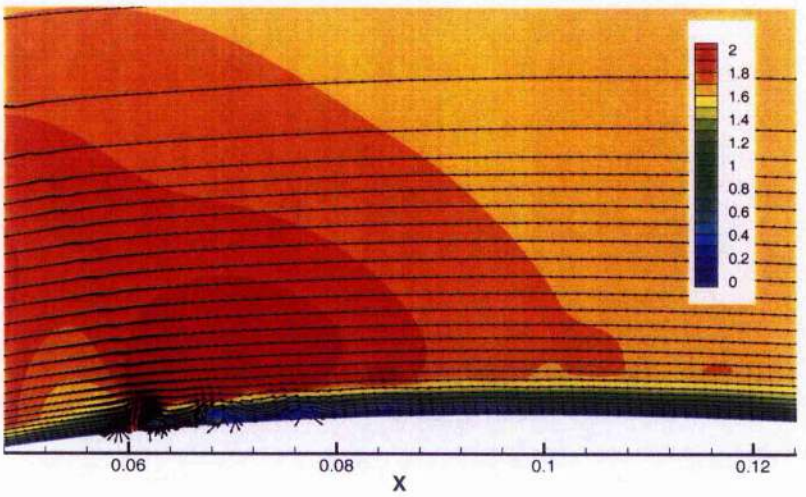

Figure 5.24: **Case 14, Unit Vector Plot**, Small vortical structures persist for only a short distance from the actuator

CASE	k_c	α
12	$40\ \pi$	11.04^o
13	$64\ \pi$	11.04^o
14	$125\ \pi$	11.04^o

Table 5.5: Summary of Suction Surface, Jet-Enabled Cases, $\alpha = 11.04^o$

.

actuation frequency and a reduced actuation period, the jet has less penetration into the primary flow, so that these structures are progressively smaller. On the suction surface, flow velocities are nominally higher than on the pressure side.

Variation of the lift coefficient after actuation commences is shown in figure 5.25. The plots are again overlaid and the (horizontal) time axes normalised. Only lift due to pressure differences between the upper and lower surfaces is included. The variation in aerodynamic lift is sinusoidal in time. Cycle to cycle, C_l magnitudes quickly settle. Peak values are intermittently of the order of nominal $C_{l_{max}}$ without stalling. As observed for actuation on the pressure surface, the mean C_l is similar regardless of the actuator operating frequency. However, when the actuation is from the suction surface, mean lift is increased rather than decreased. The mean pressure reduction induced by the actuator is therefore beneficial. On the suction surface of the aerofoil, actuation as before, is begun with a blowing event. The initial jet flow is therefore in the same direction as the lift and imparts a negative lifting force on the aerofoil.

The mean pressure coefficient, C_p, for the three cases (12, 13 and 14) is shown in figure 5.26, together with the nominal distribution. The actuator is set in a strong adverse pressure gradient. Once again there is a mean reduction in pressure immediately downstream of the actuator exit. On the suction surface, this amounts to a mean lift increase as was observed in figure 5.25. The region of pressure reduction is of similar magnitude, and covers a similar spatial extent for all cases. Aft of this peak, the mean pressure recovers abrubtly to its nominal value. This occurs smoothly for the $k_c = 125\pi$ case, but with a small over correction for the others.

The mean effect of the actuator on the suction surface, is once again to reduce local

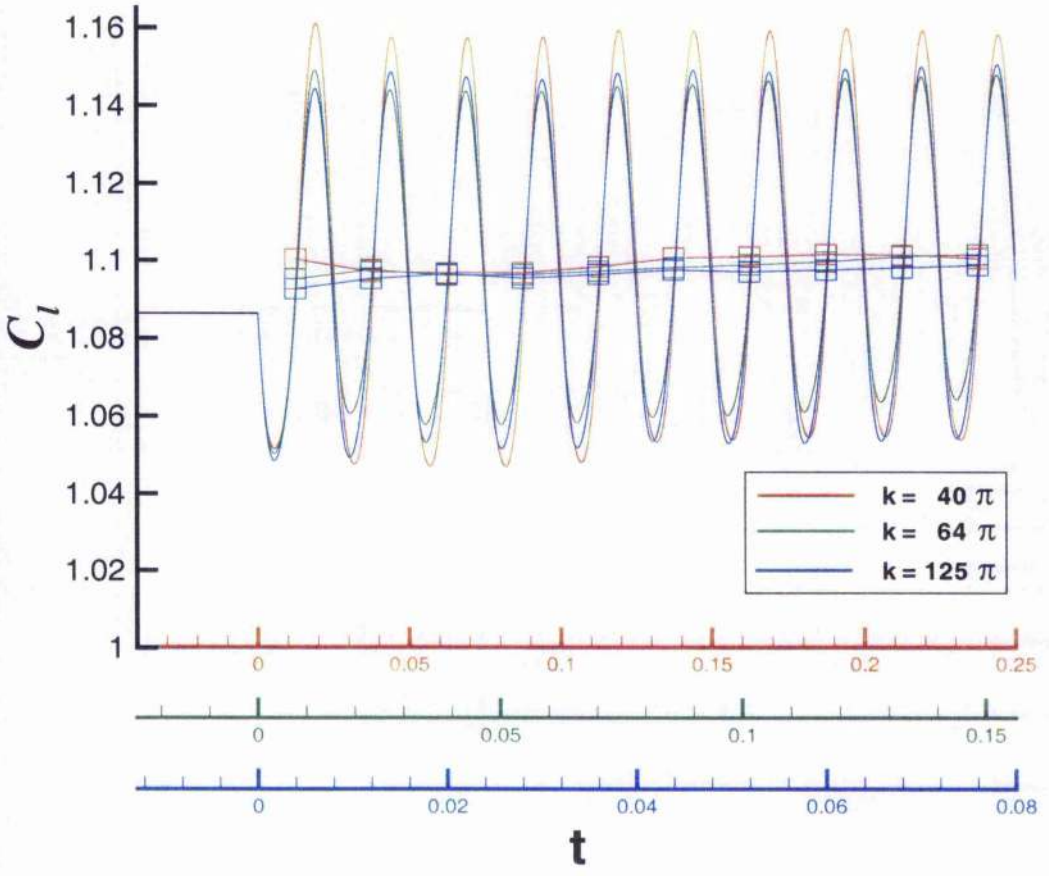

Figure 5.25: **Aerodynamic Lift Coefficient, Suction Surface Actuation**, $\alpha = 11.04^o$, C_l is plotted for the three actuation schedules used on the suction surface. Axes are again normalised to allow comparison of C_l magnitudes. Mean values are indicated by a '□' at the centre of each actuation period.

mean pressures. However, here this is beneficial. The mean C_l increase observed in figure 5.25 is due to the low pressure peak in figure 5.26.

Figure 5.27 shows the Cp distribution at five instants of the cycle for cases 12 and 14. Large fluctuations are now present on the suction surface. Waves having a period and magnitude which is dependent on the reduced frequency are produced on each actuation cycle and extend for some distance over the upper surface. Once again, these have a greater magnitude for the higher reduced frequency case. For the high frequency case on the right of the figure (case 14, $k_c = 125\pi$), the pressure resumes the nominal distribution about mid-chord. 10 cycles at such a high frequency however, represents a time duration of only $t = 0.08$. The distance travelled by any moving feature during this time is $s/c = 0.08 * u/U_\infty$, where u is its velocity. If the pressure waves travel at sonic velocity $u = U_\infty/M_\infty$, then during the actuation they travel,

$$\frac{s}{c} = \frac{0.08}{M_\infty} = 0.5333$$

The apparent disappearance of pressure waves at the mid-chord position is therefore due to the short duration of actuation.

Pressure peaks associated with convected structures, and distinguishable from the pressure waves produced directly by the actuation, were previously observed for case 8 (figure 5.21) and can again be seen here. The distance between these reduces with increasing reduced frequency, and so they are most clearly seen on the suction surface for case 12 ($k_c = 40\pi$).

As observed for actuation on the pressure surface, blowing from the actuator impedes the primary flow, with a corresponding pressure rise upstream. Increased pressure on the suction surface is an adverse effect and due to this C_l troughs seen previously in figure 5.25 are in phase with blowing events.

On the right of figure 5.27, case 14 has the greatest magnitude of pressure coefficient variation ΔC_p, of all the C_p plots featured in this chapter. Close to the actuator, the presence of vortex structures makes it difficult to estimate from the figure, the proportion of variation caused directly by the actuation. Further downstream, at around $x/c = 0.2$, sinusoidal pressure waves vary with a magnitude of around

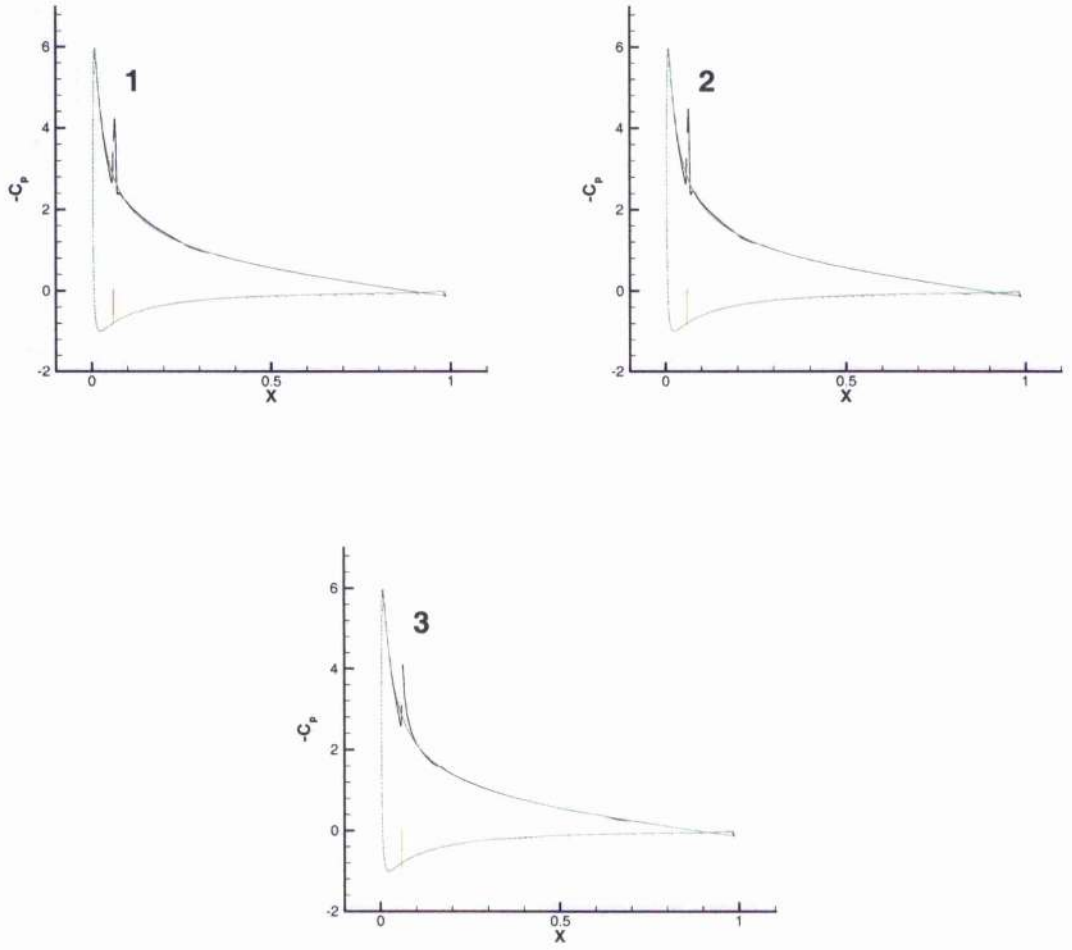

Figure 5.26: **Aerofoil Mean Pressure Distribution, Suction Surface Actuation**, $\alpha = 11.04^o$, The distribution for actuated cases in shown in black, the nominal distribution in green. **top left** case 12, **top right** case 13, **bottom** case 14, Characteristic features are a slight rise in the mean pressure ahead of the actuator and a severe fall aft of it. The actuator is positioned at a location where the nominal pressure gradient is strongly adverse.

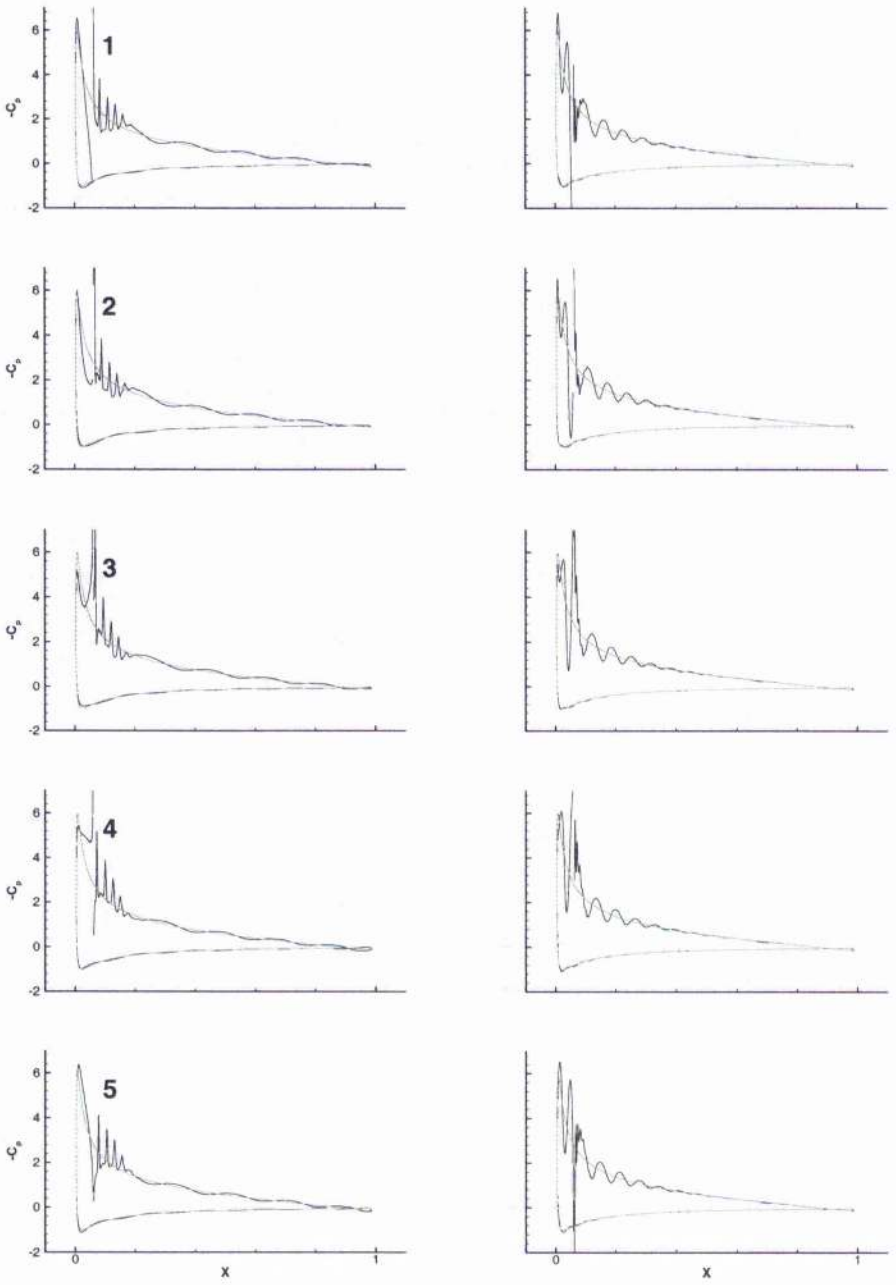

Figure 5.27: **Aerofoil Pressure Distribution at Instants of the Cycle**, The distribution for actuated cases is shown in black, nominal distribution in green. **left** $k_c = 40\pi$, **right** $k_c = 125\pi$, The actuator again produces pressure waves which propagate upstream and downstream over the upper surface, and with a period depending directly on the reduced frequency, k_c. Sharp peaks downstream of the actuator indicate the presence of travelling structures. Some small pressure variation can also be seen on the pressure surface surface.

$\Delta C_p = 0.3$. For actuators of the scale which has been discussed, this corresponds to sound pressure levels of $140dB$ or higher. It is stressed once again that non-dimensional parameters allow a range of physical analogies. It seems clear however, that any reasonable physical interpretation will cause high noise levels. Whether this is a problem depends on the application.

Noise levels have always been a major issue for helicopters. Additional noise from flow control actuators however, need not increase concerns if it is less intense than the sound produced by the helicopter itself. The human ear does not respond linearly to increases in sound intensity. The introduction of additional noise sources does not therefore linearly increase the apparent loudness. Sound pressure level is related to the sound intensity by a logarithmic scale and is used for convenience since it better describes changes in loudness as perceived by humans. As an example, even if an actuator is independently as loud as the helicopter itself, say $100dB$ at $30m$, the apparent increase in loudness when the vehicle is operating with the actuator enabled would only be around $3dB$.

5.7.2 Jet Enabled, Angle of Attack $\alpha = 12.022^o$

Jet-enabled cases at $\alpha = 11.04^o$ demonstrate that on the suction surface, a single synthetic jet is able to improve the mean lift. At $\alpha = 12.022^o$, the aerofoil is almost at the point of static stall. The lift coefficient is close to its maximum, $C_{l_{max}}$. For synthetic jets to be deemed successful for the helicopter application, they must show that they can continue to increase lift at nominal stall. For the numerical experiments in this section, freestream conditions were again, $Re_c = 1.4 \text{ x } 10^6$ and $M = 0.15$. Peak jet velocity was $V_0/U_\infty = 3.0$. Three cases were run of 10 actuation cycles each. Reduced frequencies were $k_c = 40\pi$, $k_c = 64\pi$ and $k_c = 80\pi$. Cases are summarised in table 5.6

Figures 5.28 to 5.30 are unit-vector plots of the cases 15, 16 and 17 obtained during the tenth cycle. The behaviour is consistent with the results obtained at $\alpha = 11.04^o$. Individually convected vortices can be seen in each plot, and the scale of the structures once again decreases with increasing reduced frequency.

Reduced frequencies of $k_c = 40\pi$ and $k_c = 64\pi$ were also used at $\alpha = 11.04^o$,

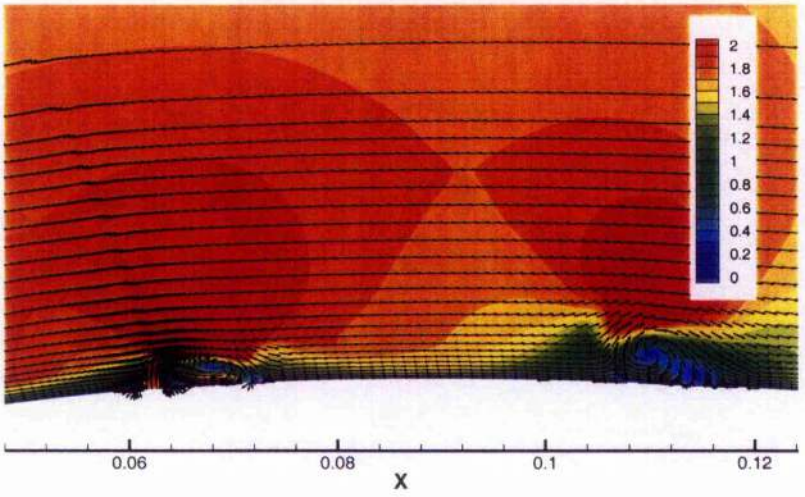

Figure 5.28: **Case 15, Unit Vector Plot**, $k_c = 20\pi$, Vortices convected along the aerofoil upper surface are larger than for any of the other suction surface actuation cases, reflecting the low reduced frequency.

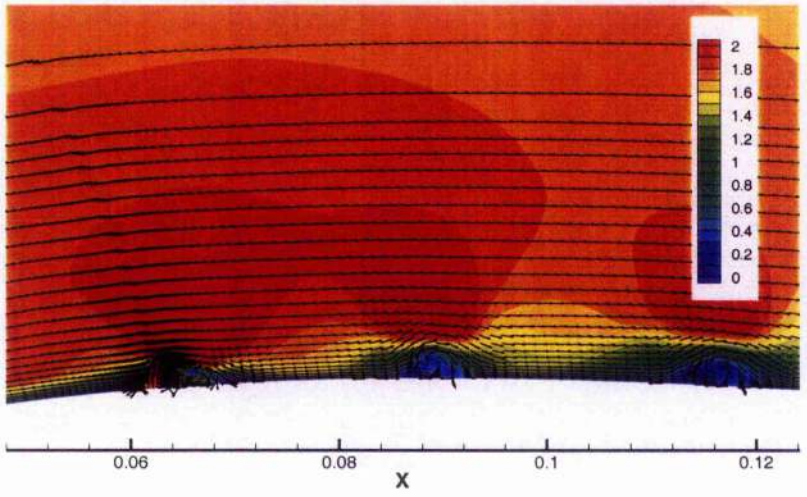

Figure 5.29: **Case 16, Unit Vector Plot**, $k_c = 40\pi$, Consistent with behaviour observed earlier, the increase in reduced frequency k, and consequent reduction in actuation period, mean that the structures produced during actuation are smaller and less spaced. Unit vectors for the corresponding $k_c = 40\pi$ case at $\alpha = 11.04^o$ can be seen in figure 5.22. Most features are similar to those shown here.

CASE	k_c	α
15	20 π	12.022^o
16	40 π	12.022^o
17	64 π	12.022^o

Table 5.6: Summary of Suction Surface, Jet-Enabled Cases

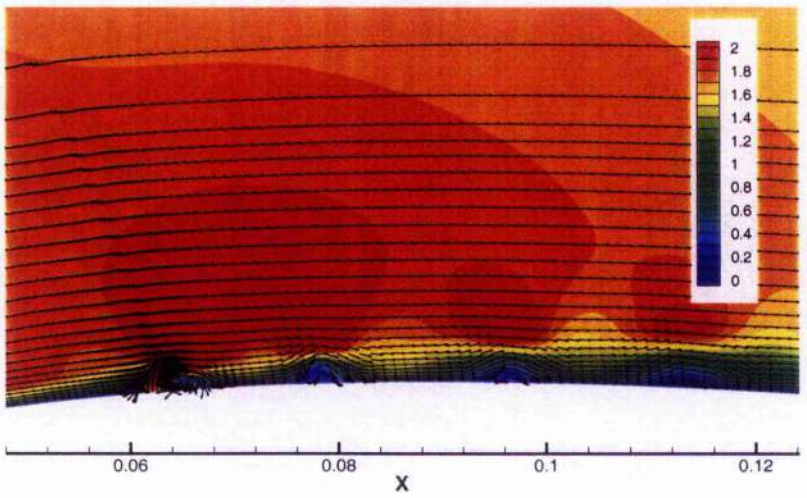

Figure 5.30: **Case 17, Unit Vector Plot**, $k_c = 64\pi$, Behaviour is similar to that in figure 5.23. Case 13 also has a reduced operating frequency of $k_c = 64\pi$

reflecting this, the figures for cases 16 and 17 (figs 5.29 and 5.30) are similar to those for cases 12 and 13 (figs 5.22 and 5.23) repectively. The lower frequency case 15 ($k_c = 20\pi$), follows the same trend as before, with larger structures being convected further along the aerofoil surface.

Lift coefficient variation is shown in figure 5.31. The plots are in the same fashion as before. Baseline lift is higher than at $\alpha = 11.04^o$ due to the modified pressure distribution associated with the increase in incidence. Lift variation is again sinusoidal with greater peak to peak magnitudes than before.

Time averaged pressure coefficient data for cases 15, 16 and 17 is shown in figure

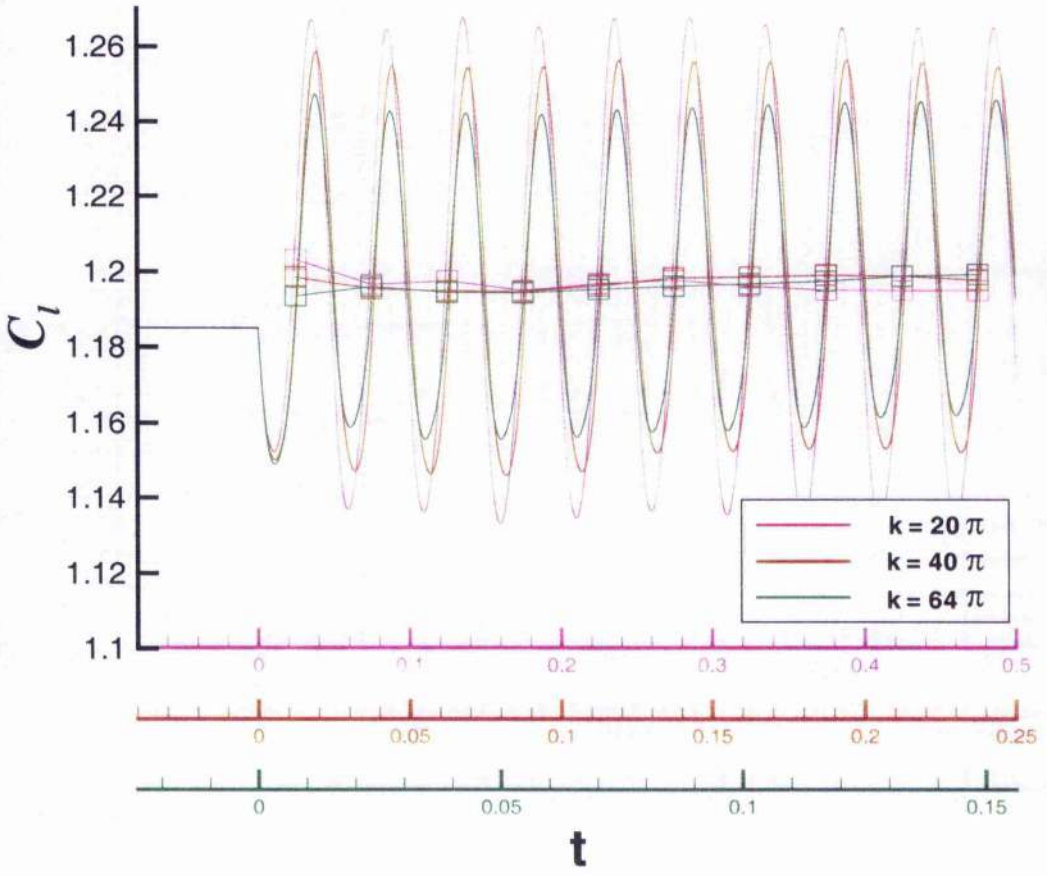

Figure 5.31: **Aerodynamic Lift Coefficient,** $\alpha = 12.022^o$, C_l is plotted for the three actuation schedules used on the suction surface. Axes are again normalised to allow comparison of C_l magnitudes. Mean values are indicated by a '□' at the centre of each actuation period.

5.32. The nominal distribution is only slightly changed from $\alpha = 11.04^o$. Cases 16 and 17 are therefore similar to the corresponding $k_c = 40\pi$ and $k_c = 64\pi$, $\alpha = 11.04^o$ cases. Pressure recovery aft of the actuator is slightly different for Case 16. Mean pressure distortions at this location are due to the acceleration of the convected vortices being affected by the the production of new structures.

The C_p distribution at instants of the cycle is shown in figure 5.33 for cases 15 and 17. As before, the magnitude of pressure waves is greater when the reduced frequency is increased. Case 15 has the lowest reduced frequency of any actuation used on the suction surface, and consequently produced the largest convected structures. The pressure peaks associated with these are therefore more spaced and of greater magnitude.

5.8 Summary

It was stated in Chapter 1 that the aim of this work was to investigate the potential of using synthetic jet actuators for the control of flow over a helicopter rotor blade. A factor impeding the improvement of speed and loading-carrying performance for a helicopter in forward flight is the production of lift at dynamic stall onset. The primary objective of this chapter is to assess the effect of a single synthetic jet actuator on an aerofoil at high angle of attack. The NACA-0012 has been chosen as a typical rotor blade section, and a synthetic jet actuator is simulated close to its leading edge.

Synthetic jet actuation was first tested with the NACA-0012 set at zero angle of attack. When the actuator is enabled, the regimes observed on a flat plate in chapter 3 are once again seen. However, on the aerofoil, transition between individually convected vortices and the establishment of a permanent recirculation region spans a wider range of reduced frequency and occurs at significantly higher values.

Actuation was next used on the pressure surface of a pitched aerofoil. The behaviour of the vortical structures which developed, i.e. their variation with changes in the reduced frequency k_c, was seen to be similar to that previously observed when a synthetic jet was used on a flat plate. Vortices were individually convected for the

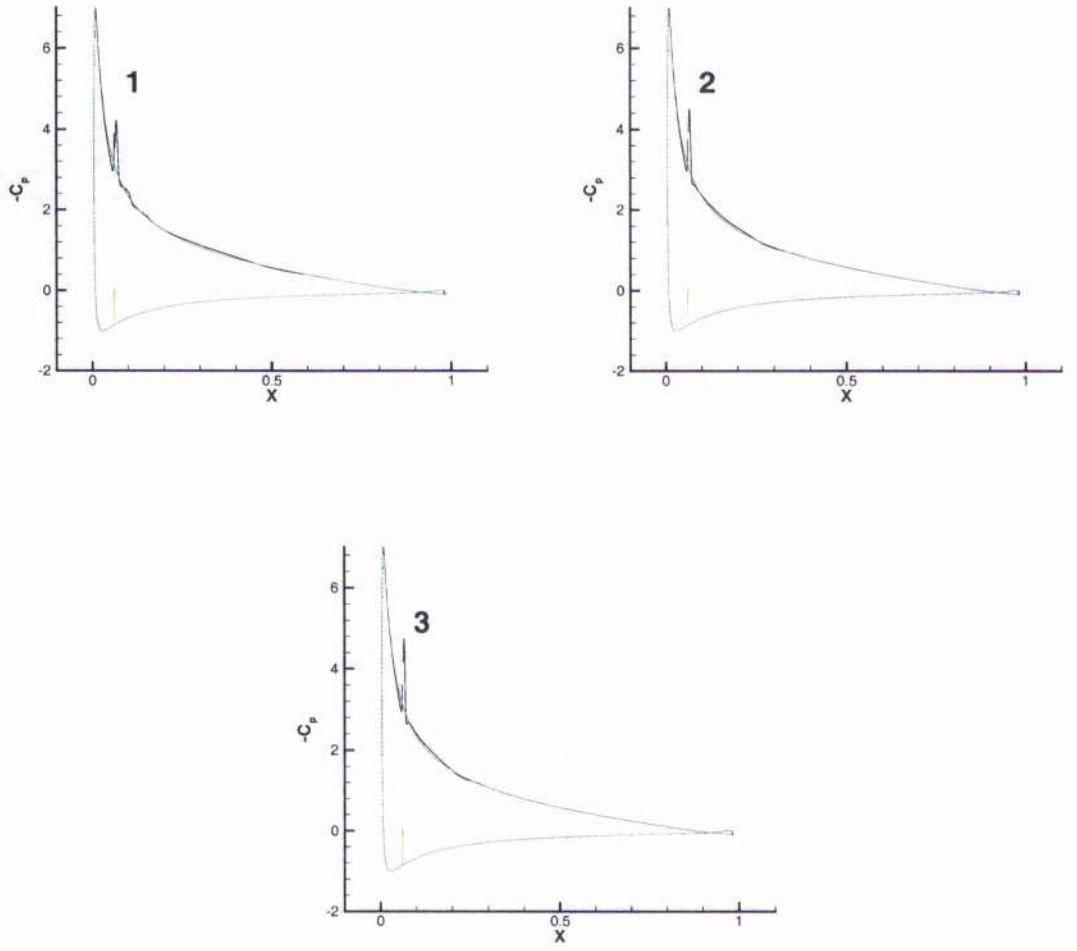

Figure 5.32: **Aerofoil Mean Pressure Distribution,** $\alpha = 12.022^o$, The distribution for actuated cases in shown in black, the nominal distribution in green. **top left:** case 15, **top right:** case 16, **bottom:** case 17.

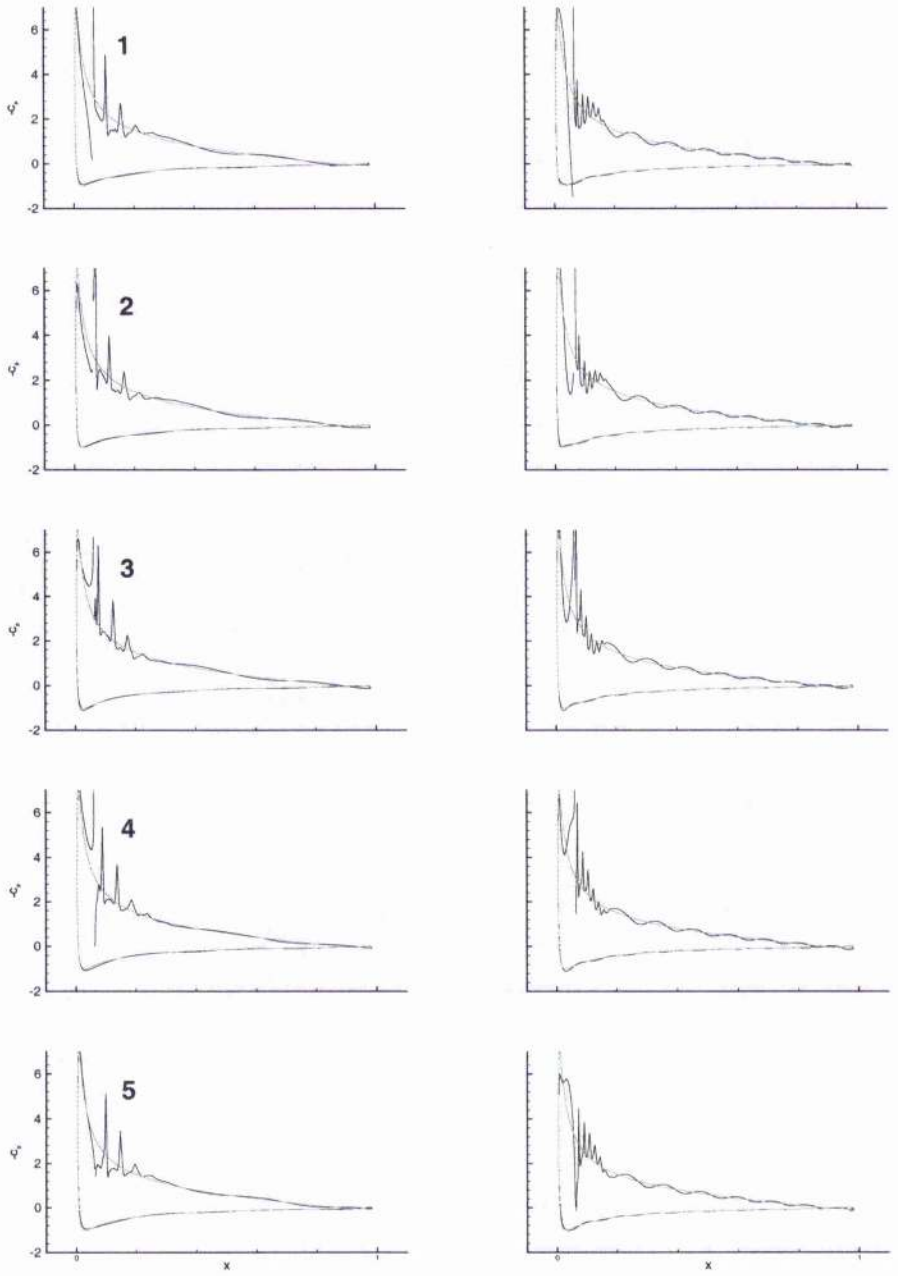

Figure 5.33: **Aerofoil Pressure Distribution at Instants of the Cycle,** $\alpha = 12.022^o$, The distribution for actuated cases is shown in black, nominal distribution in green. **left:** $k_c = 20\pi$, **right:** $k_c = 64\pi$, Top frames again show the instantaneous pressure distribution shortly before peak blowing. Peaks indicating the presence of individually convected vortices are especially clear for case 15, $k_c = 20\pi$.

lowest reduced frequency (case 8, $k_c = 20\pi$), and a recirculation region became established at higher reduced frequencies. For either regime, the structures were relatively large, becoming noticeably smaller and more stretched out at the highest values of k_c. During blowing, the jet from the actuator presents an effective barrier to the primary flow. The retardation of the primary flow causes the pressure at the aerofoil surface to rise. During suction, fluid in the vicinity of the actuator exit is accelerated, with a consequent reduction in pressure. The alternate raising and lowering of pressure causes pressure waves which are apparent across the pressure surface but which barely affect the instantaneous pressure distributions on the suction surface. The effect on the time averaged pressure distribution is slight and is confined to a small region downstream of the jet exit. This result is similar no matter which regime is exhibited.

A permanently established recirculation bubble causes a mean pressure reduction. Individually convected vortices do not immediately attain the velocity of the cross-flow and whilst being generated, these occupy a location immediately aft of the jet exit. This again causes a mean pressure reduction.

Actuation on the suction surface was implemented aft of the suction peak in a region of strong adverse pressure gradient. At this location, although the fluid is quickly decelerating, velocities are generally higher than the freestream and the boundary layer is relatively thin. In these conditions, a permanent recirculation bubble did not become established for any of the reduced frequencies used. The individual vortices produced were smaller than those observed during pressure surface actuation, and dissipated within a short distance of the actuator. Sinusoidal pressure waves were again apparent. Due to the generally high noise level of helicopters, significant actuator noise could theoretically be accomodated with little increase in the perceived loudness. For current cases however, the pressure variation implies noise levels of around $140dB$ or higher, and this is likely to be prohibitive for practical helicopter application.

The mean effect of actuation, whether on the pressure or suction surface, is always to reduce local pressures. Actuation on the pressure surface then, serves to reduce the lift coefficient. On the suction surface however, the blowing effort can provide some induced aerodynamic benefit. This does not rely on the production of persisting

recirculation regions however.

The mean lift increases which can be achieved with actuation on the suction surface are relatively small. To put this in perspective, pitching upwards and downwards, the same grid was used to simulate actuation on both the pressure and suction surfaces of the aerofoil at angle of attack, $\alpha = 11.04^{o}$. There is a slight difference in baseline C_l magnitude between the pitch-up and pitch-down results. This is of the same order as the mean lift increases gained by actuation, i.e. lift increases are of a scale commensurable with the acceptable tolerance for a CFD solution. Such improvements are difficult to measure experimentally. Synthetic jets cannot therefore, be recommended on the strength of the lift increase from a single actuator. However, all the evidence suggests that the actuator rapidly produces induced aerodynamic effects which are potentially in excess of its power requirements. If a number of actuators can each make a similar contribution without adversely affecting each others performance, then significant benefits may be possible.

Chapter 6

Conclusions and Future Work

Synthetic jet flow in a quiescent atmosphere was modelled using a two-dimensional RANS flow solver. The flow was generated from a deforming cavity actuator, simulated using a deforming grid approach. Such synthetic jet flows have been the subject of a number of investigations, and the intention in chapter 2 was to compare with the available literature and thus validate the CFD approach.

The computed synthetic jet flow developed between regions of opposite sense vorticity, in qualitative agreement with the literature. Analysis of velocity profiles demonstrated quantitative agreement close to the actuator exit plane. At this location, flow from the actuator is laminar, at greater distances downstream, the synthetic jet is reported to be turbulent. In the current model the flow remained laminar and consequently the jet spreading was much reduced. This caused comparisons to progressively worsen with downstream distance. To emulate the results of previous experiments and computations, a turbulence model tuned specifically for the synthetic jet problem could be used. This would be required to produce greater turbulent dissipation in jet shear at Reynolds numbers of around $Re = 10^3$.

The phenomenon of a jet flow produced from an oscillating surface in a quiescent atmosphere, holds a fascination for fluid dynamicists. However, it is quite removed from most of the suggested applications of the synthetic jet actuator as a flow control device. The implication of some papers which have considered the phenomenon, is that a synthetic jet produced in this way might be used in the same manner as steady jets have been used for flow control. The experience of this work and the

more extensive synthetic jet literature however, is that a quasi-steady jet flow is not generally produced in a crossflow. Since the quiescent atmosphere case has little in common with the target application, it is recommended for future work that research effort be concentrated on actuator in crossflow configurations.

The simplest actuator-in-crossflow case has the actuator embedded in a flat plate aligned parallel with the freestream. In chapter 3, the deforming cavity actuator developed in chapter 2, was studied in this configuration. A constant deflection of the cavity floor was imposed. Massflow rate across the exit plane varied with the reduced frequency k_h but was independent of the flat plate length upstream of the actuator, x_{le}, and hence of the local boundary layer thickness, δ. The shape of instantaneous exit profiles was found to be reasonably independent of reduced frequency k_h, The shape and phase were independent of x_{le}.

The external flowfield was investigated and over the range of conditions considered, two distinct flow regimes were observed,

1) *individually convected vortices*; vortices produced on the downstream side of the actuator are accelerated in the crossflow direction under its influence.

2) *recirculation regions*; under certain operating conditions, the escaping vortices are impeded in their motion away from the actuator and appear to be consumed by a recirculating system which becomes established a short distance downstream from the exit.

Also in chapter 3, a simpler model was used whereby the fluid to and from the actuator was instead simulated by an oscillatory velocity boundary condition. Equivalent cases were run to compare the two approaches. These were found to be capable of producing similar effects. However, due to the differences in the time varying behaviour at the exit plane, the same behaviour was not always found for equivalent inputs. Any future development of the imposed velocity boundary condition model should use more realistic profile shapes and schedules. The dependence of exit profile shape on input parameters has been discussed above. These results allow the determination of appropriate profile shapes and schedules from only a small number of full deforming cavity type calculations.

For the development of a control strategy it is desirable to understand the effect of

actuation across a wide range of operating conditions. In chapter 4, a dimensional analysis identified the ratio of jet and freestream velocities, V_0/U_∞, the reduced operating frequency $k_h = \pi f h/U_\infty$, a Reynolds number $Re_h = \rho U_\infty h/\mu$ and the ratio x_{le}/h as the significant parameters for a velocity boundary condition model. Initial tests considered the response of surface pressures downstream of the actuator to input combinations of these parameters. It was found that maximum reduction of mean surface pressure coincided with the transition between the flow regimes discussed above. The parameter study was then focussed on identifying the boundary between these regimes (the optimal condition) across an extended range. This can be taken from figures 4.6, 4.7 and 4.8 in chapter 4. Over a wide parameter field, recirculation regions were found to be promoted by increases in V_0/U_∞, increases in reduced frequency k_h, increases in x_{le}/h hence δ, and by decreases in Re_h.

Parameter combinations were used in chapter 4, which were outside the range experienced in chapter 3. Further comparisons between velocity boundary condition and deforming cavity approaches, and a consideration of compressibility effects is desirable for future work.

In chapter 5 actuation was considered on a pitched NACA-0012 aerofoil representing a rotor blade section. The intention was to determine that the actuator could be significant in this context. The imposed velocity boundary condition actuator was tested on pressure and suction surfaces close to the leading edge. The same regimes as had been observed in chapter 3 were produced on the pressure surface. However, the boundary between these regimes appeared to be at different parameter combinations than had been determined from chapter 4. This is explained by the low crossflow velocity at the location of the actuator on the pressure surface of the aerofoil. On the suction surface, the local crossflow velocity was significantly higher than freestream. As a result of this, permanent recirculation regions were not established for any of the parameter combinations attempted. Although not working in the optimal condition, the reduction of local pressures on the suction surface caused lift increases. Therefore, a positive global effect was obtained. A first recomendation for future work, is that experimental data be obtained for those cases which have been discussed here but for which experimental results have not been available.

Acoustic effects were briefly considered in chapter 5. Sound pressure levels (SPL) of over $140dB$ (close to the actuator) are implied by the non-dimensional parameters describing the freestream and operating conditions. Such noise levels are likely to be prohibitive for helicopter application. This must be considered when planning future experiments. A significant degree of noise may be tolerable for the practical actuator however, even to the level produced by the helicopter itself.

Although mean lift gains calculated in chapter 5 are small, it is emphasised that only a single actuator is being used. The local impact of the actuator is in fact relatively large. If similar lift increment can be achieved from each of a number of actuators then the net lift improvement could be of significant benefit. In reality, it is unlikely that the additional lift will be proportional to the number of actuators however. Each actuator is sure to be affected by the operation of any others which surround it, i.e. there will be competition amongst actuators for working fluid. This may lead to entirely different flow scenarios to those which have been discussed. The simultaneous operation of multiple actuators is therefore an important area for further research. This could be pursued using a velocity boundary condition approach, as in chapters 4 and 5. It should be borne in mind that this method imposes the instantaneous exit profiles, and therefore presumes that the chosen oscillatory schedule can be delivered from real actuators. However, producing this for a number of actuators may present a difficult control problem.

The recommendation is that the net effect of an array of actuators instead be evaluated on a flat plate model using deforming cavity type actuation as in chapter 2. Representative velocity boundary conditions can then be used to reproduce the observed flow behaviour on more complex geometries. This follows the methodology of the current work. It is expected to be easier to control the mode and magnitude of cavity floor deflection than to exercise control over time varying velocity exit profiles. Equivalence of numerical and physical experiments should therefore be simplified.

The recommendations for future work which have been made so far, are all extensions to the current work without any radical change of direction. Each suggestion concerns the aerodynamics of a synthetic jet concept. During the course of this study it has become apparent that synthetic jet aerodynamics research is outstripping the development of a practical actuator. Even where physical synthetic jet

experiments have been performed, the actuators have only been a means to produce zero net mass flow actuation rather than a step towards the construction of an actuator which might be used in practical application. It seems that there is no convergence towards a practical actuator or consensus on what physical form this should have. This is cerainly an area for parallel research.

The design of a practical actuator must consider its weight and geometric scale, the materials and methods of construction, its cost and power requirements, as well as ease of maintenance. In addressing these criteria, compromises may have to be made. The actuator geometry and therefore its internal aerodynamics, is the link between the actuator's construction and its ability to effect flow control. A parameter study to establish a preferred geometrical form and mode of operation would be useful. This would provide a target for those involved in actuator construction and a starting point for aerodynamics research. Work can then proceed in each area simultaneously. The difficulty of physically taking measurements inside the actuator cavity, makes CFD essential to the design process. Validation can be sought by consideration of the external flow.

Appendix A

The PMB2D code

A.1 Introduction

This document gives technical background to the two-dimensional parallel multi-block flow solver, Pmb2D developed at the University of Glasgow. It is adapted from the guide of Badcock, Cantariti and Gribben[80]. Nomenclature is defined as it is used and reference is made to the open literature for fuller details of the theory.

A.1.1 Non-dimensional form

The derivation of the Navier-Stokes equations is included in most fluid dynamics texts, for example [82]. In a two-dimensional Cartesian frame they can be written as

$$\frac{\partial \mathbf{W}}{\partial t} + \frac{\partial (\mathbf{F}^i - \mathbf{F}^v)}{\partial x} + \frac{\partial (\mathbf{G}^i - \mathbf{G}^v)}{\partial y} = 0 \tag{A.1}$$

The vector $\mathbf{W}$ is the vector of conserved variables:

$$\mathbf{W} = \begin{pmatrix} \rho \\ \rho u \\ \rho v \\ \rho E \end{pmatrix} \tag{A.2}$$

where ρ is the density, $\mathbf{V} = (u, v)$ is the Cartesian velocity vector and E is the total energy per unit mass. The flux vectors $\mathbf{F}$ and $\mathbf{G}$ consist of inviscid (^{i}) and (^{v})

viscous diffusive parts. These are written in full as :

$$\mathbf{F}^i = \begin{pmatrix} \rho u \\ \rho u^2 + p \\ \rho uv \\ \rho uH \end{pmatrix}$$
$$\mathbf{G}^i = \begin{pmatrix} \rho v \\ \rho uv \\ \rho v^2 + p \\ \rho vH \end{pmatrix} \tag{A.3}$$

$$\mathbf{F}^\nu = \frac{1}{Re} \begin{pmatrix} 0 \\ \tau_{xx} \\ \tau_{xy} \\ u\tau_{xx} + v\tau_{xy} + q_x \end{pmatrix}$$
$$\mathbf{G}^\nu = \frac{1}{Re} \begin{pmatrix} 0 \\ \tau_{xy} \\ \tau_{yy} \\ u\tau_{xy} + v\tau_{yy} + q_y \end{pmatrix} \tag{A.4}$$

The stress tensor and of the heat flux vector components are written as:

$$\begin{aligned} \tau_{xx} &= -\mu \left(2\frac{\partial u}{\partial x} - \frac{2}{3}\left(\frac{\partial u}{\partial x} + \frac{\partial v}{\partial y} \right) \right) \\ \tau_{yy} &= -\mu \left(2\frac{\partial v}{\partial y} - \frac{2}{3}\left(\frac{\partial u}{\partial x} + \frac{\partial v}{\partial y} \right) \right) \\ \tau_{xy} &= -\mu \left(\frac{\partial u}{\partial y} + \frac{\partial v}{\partial x} \right) \\ q_x &= \frac{1}{(\gamma - 1)M_\infty^2} \frac{\mu}{Pr} \frac{\partial T}{\partial x} \\ q_y &= -\frac{1}{(\gamma - 1)M_\infty^2} \frac{\mu}{Pr} \frac{\partial T}{\partial y} \end{aligned} \tag{A.5}$$

Here γ is the specific heat ratio, Pr is the laminar Prandtl number, T is the static temperature and M_∞ and Re are the freestream Mach number and Reynolds number, respectively. The various flow quantities are related to each other by the perfect gas relations:

$$\begin{aligned} H &= E + \frac{p}{\rho} \\ E &= e + \frac{1}{2}\left(u^2 + v^2\right) \\ p &= (\gamma - 1)\,\rho e \\ \frac{p}{\rho} &= \frac{T}{\gamma M_\infty^2} \end{aligned} \tag{A.6}$$

Finally, the laminar viscosity μ is evaluated using Sutherland's law:

$$\frac{\mu}{\mu_0} = \left(\frac{T}{T_0}\right)^{3/2} \frac{T_0 + 110}{T + 110} \tag{A.7}$$

where μ_0 is a reference viscosity at a reference temperature T_0. These can be taken as $\mu_0 = 1.7894\text{x}10^{-5}$ kg/(m.s) with $T_0 = 288.16$ K. The non-dimensionalisation used is as follows:

$$x = \frac{x^*}{L^*}, \qquad y = \frac{y^*}{L^*}, \qquad t = \frac{t^*}{L^*/V_\infty^*},$$

$$u = \frac{u^*}{V_\infty^*}, \qquad v = \frac{v^*}{V_\infty^*}, \qquad \mu = \frac{\mu^*}{\mu_\infty^*},$$

$$\rho = \frac{\rho^*}{\rho_\infty^*}, \qquad p = \frac{p^*}{p_\infty^* V_\infty^{*2}}, \qquad T = \frac{T^*}{T_\infty^*}, \qquad e = \frac{e^*}{V_\infty^{*2}} \tag{A.8}$$

where * denotes dimensional quantities and $_\infty$ denotes free-stream values.

A.1.2 Reynolds-averaged form

The Reynolds-averaged form of the Navier-Stokes equations permits turbulent flow to be considered. The development is not presented here. It is merely noted that

fundamental to this approach is the consideration of the flow variables as consisting of two components, a time averaged component and a turbulent fluctuation component. For example, density and velocity components are decomposed as

$$u = \bar{u} + u', \qquad v = \bar{v} + v', \qquad \rho = \bar{\rho} + \rho'$$

The quantities k (the turbulent kinetic energy), μ_T (the turbulent viscosity) and Pr_T (the turbulent Prandtl number) are introduced via the important Boussinesq assumption in an attempt to model the fluctuating-variable stress terms arising from the Reynolds averaging. For a complete discussion of this subject see [82]. The Reynolds-averaged form of the Navier-Stokes equations are identical to those presented in Section A.1.1, except for the stress tensor and heat flux vector components shown below. The variables should be considered as mean flow quantities (superscripts are dropped for clarity). The turbulent nature of the flow is modelled via μ_T and k and a closure hypothesis or turbulence model, for example the $k-\omega$ model, Section A.2.

$$\begin{aligned}
\tau_{xx} &= -(\mu+\mu_T)\left(2\frac{\partial u}{\partial x} - \frac{2}{3}\left(\frac{\partial u}{\partial x} + \frac{\partial v}{\partial y}\right)\right) + \frac{2}{3}\rho k \\
\tau_{yy} &= -(\mu+\mu_T)\left(2\frac{\partial v}{\partial y} - \frac{2}{3}\left(\frac{\partial u}{\partial x} + \frac{\partial v}{\partial y}\right)\right) + \frac{2}{3}\rho k \\
\tau_{xy} &= -(\mu+\mu_T)\left(\frac{\partial u}{\partial y} + \frac{\partial v}{\partial x}\right)
\end{aligned} \tag{A.9}$$

$$\begin{aligned}
q_x &= -\frac{1}{(\gamma-1)M_\infty^2}\left(\frac{\mu}{Pr} + \frac{\mu_T}{Pr_T}\right)\frac{\partial T}{\partial x} \\
q_y &= -\frac{1}{(\gamma-1)M_\infty^2}\left(\frac{\mu}{Pr} + \frac{\mu_T}{Pr_T}\right)\frac{\partial T}{\partial y}
\end{aligned} \tag{A.10}$$

A.1.3 General Curvilinear form

The equations are written in curvilinear (ξ,η) form to facilitate use on curvilinear grids of arbitrary local orientation and density. A space transformation from the Cartesian coordinate system to the local coordinate system must then be introduced:

$$\begin{aligned}
\xi &= \xi(x,y) \\
\eta &= \eta(x,y) \\
t &= t
\end{aligned}$$

The Jacobian matrix of the transformation is given by

$$J = \frac{\partial(\xi,\eta)}{\partial(x,y)}$$

The equations (A.1) can then be written as

$$\frac{\partial \hat{\mathbf{W}}}{\partial t} + \frac{\partial(\hat{\mathbf{F}}^i - \hat{\mathbf{F}}^v)}{\partial \xi} + \frac{\partial(\hat{\mathbf{G}}^i - \hat{\mathbf{G}}^v)}{\partial \eta} = 0 \tag{A.11}$$

where

$$\begin{aligned}
\hat{\mathbf{W}} &= \frac{\mathbf{W}}{J} \\
\hat{\mathbf{F}}^i &= \frac{1}{J}\left(\xi_x \mathbf{F}^i + \xi_y \mathbf{G}^i\right) \\
\hat{\mathbf{G}}^i &= \frac{1}{J}\left(\eta_x \mathbf{F}^i + \eta_y \mathbf{G}^i\right) \\
\hat{\mathbf{F}}^v &= \frac{1}{J}\left(\xi_x \mathbf{F}^v + \xi_y \mathbf{G}^v\right) \\
\hat{\mathbf{G}}^v &= \frac{1}{J}\left(\eta_x \mathbf{F}^v + \eta_y \mathbf{G}^v\right)
\end{aligned} \tag{A.12}$$

The expressions for the inviscid fluxes can be simplified somewhat by defining

$$\begin{aligned}
U &= \xi_x u + \xi_y v \\
V &= \eta_x u + \eta_y v
\end{aligned} \tag{A.13}$$

The inviscid fluxes can then be written as

$$\begin{aligned}
\hat{\mathbf{F}}^i &= \begin{pmatrix} \rho U \\ \rho u U + \xi_x p \\ \rho v U + \xi_y p \\ \rho U H \end{pmatrix} \\
\hat{\mathbf{G}}^i &= \begin{pmatrix} \rho V \\ \rho u V + \eta_x p \\ \rho v V + \eta_y p \\ \rho V H \end{pmatrix}
\end{aligned} \tag{A.14}$$

The derivative terms found in the viscous fluxes are evaluated using the chain rule, for example

$$\frac{\partial u}{\partial x} = \xi_x \frac{\partial u}{\partial \xi} + \eta_x \frac{\partial u}{\partial \eta}$$

The evaluation of the metrics of the transformation is clearly important, and is described in full in [82].

A.2 Turbulence Model

The turbulence model available in the code is the two-equation $k-\omega$ turbulence model.

A.2.1 Non-dimensional form

The $k-\omega$ turbulence model of Wilcox [83] in non-dimensional form can be written as follows:

Eddy Viscosity

$$\mu_T = \rho k/\omega \tag{A.15}$$

Turbulence Kinetic Energy

$$\rho\frac{\partial k}{\partial t}+\rho\mathbf{V}.\nabla k-\frac{1}{Re}\nabla.\left[\left(\mu+\sigma^*\mu_T\right)\nabla k\right] = \mu_T P-\frac{2}{3}\rho k S-\beta^*\rho k\omega \tag{A.16}$$

Specific Dissipation Rate

$$\rho\frac{\partial \rho\omega}{\partial t}+\rho\mathbf{V}.\nabla\omega-\frac{1}{Re}\nabla.\left[\left(\mu+\sigma\mu_T\right)\nabla\omega\right] = \alpha\frac{\omega}{k}\left[\mu_T P-\frac{2}{3}\rho k S\right]-\beta\rho\omega^2 \tag{A.17}$$

Closure Coefficients

$$\alpha=5/9, \qquad \beta=3/40, \qquad \beta^*=9/100, \qquad \sigma=1/2, \qquad \sigma^*=1/2 \tag{A.18}$$

In the above relations,

$$\begin{aligned} P &= \left[\left(\nabla\mathbf{V}+\nabla\mathbf{V}^T\right):\nabla\mathbf{V}-\frac{2}{3}\left(\nabla.\mathbf{V}\right)^2\right] \\ S &= \nabla.\mathbf{V} \end{aligned}$$

The equations as shown above use the same non-dimensional quantities as in Section A.1.1, with the addition of

$$k = \frac{k^* Re}{V_\infty^{*2}}, \qquad \omega = \frac{\omega^* L^*}{V_\infty^*}, \qquad \mu_T = \frac{\mu_T^*}{\mu_\infty^*}$$

A.2.2 General Curvilinear form

The equations for k and ω can be written in a curvilinear form analogous to that used for the mean flow equations in Section A.1.3 . Written in full, the two-dimensional Cartesian form of equations (A.17) and (A.18) become

$$\frac{\partial \mathbf{q}}{\partial t} + \frac{\partial(\hat{\mathbf{F}}_T^i - \hat{\mathbf{F}}_T^v)}{\partial \xi} + \frac{\partial(\hat{\mathbf{G}}_T^i - \hat{\mathbf{G}}_T^v)}{\partial \eta} = \frac{\hat{\mathbf{S}}_T}{J} \tag{A.19}$$

where the vectors of conserved variables, convective and diffusive fluxes are respectively

$$\mathbf{q} = \frac{1}{J}\begin{pmatrix} \rho k \\ \rho \omega \end{pmatrix} \qquad \hat{\mathbf{F}}_T^i = \frac{1}{J}\begin{pmatrix} \rho k U \\ \rho \omega U \end{pmatrix} \qquad \hat{\mathbf{G}}_T^i = \frac{1}{J}\begin{pmatrix} \rho k V \\ \rho \omega V \end{pmatrix}$$

$$\hat{\mathbf{F}}_T^v = \frac{1}{J}\left(\xi_x \hat{\mathbf{M}} + \xi_y \hat{\mathbf{N}}\right) \qquad \hat{\mathbf{G}}_T^v = \frac{1}{J}\left(\eta_x \hat{\mathbf{M}} + \eta_y \hat{\mathbf{N}}\right)$$

where the tensors M and N are equal to

$$\hat{\mathbf{M}} = \frac{1}{Re}\begin{pmatrix} (\mu + \sigma^* \mu_T)(\xi_x k_\xi + \eta_x k_\eta) \\ (\mu + \sigma \mu_T)(\xi_x \omega_\xi + \eta_x \omega_\eta) \end{pmatrix}$$

$$\hat{\mathbf{N}} = \frac{1}{Re}\begin{pmatrix} (\mu + \sigma^* \mu_T)(\xi_y k_\xi + \eta_y k_\eta) \\ (\mu + \sigma \mu_T)(\xi_y \omega_\xi + \eta_y \omega_\eta) \end{pmatrix}$$

Finally, the source term is written as

$$\hat{\mathbf{S}}_T = \begin{pmatrix} \hat{\mathbf{P}}_k - \hat{\mathbf{D}}_k \\ \hat{\mathbf{P}}_\omega - \hat{\mathbf{D}}_\omega \end{pmatrix}$$

with the components

$$\hat{\mathbf{P}}_k = \mu_T \left\{ \left(\frac{\partial u}{\partial y} + \frac{\partial v}{\partial x} \right)^2 + 2 \left[\left(\frac{\partial u}{\partial x} \right)^2 + \left(\frac{\partial v}{\partial y} \right)^2 \right] - \frac{2}{3} \left(\frac{\partial u}{\partial x} + \frac{\partial v}{\partial y} \right)^2 \right\} - \frac{2}{3} \rho k \left(\frac{\partial u}{\partial x} + \frac{\partial v}{\partial y} \right)$$

$$\hat{\mathbf{D}}_k = \beta^* \rho \omega k$$

$$\hat{\mathbf{P}}_\omega = \alpha \frac{\omega}{k} \hat{\mathbf{P}}_k$$

$$\hat{\mathbf{D}}_\omega = \beta \rho \omega^2$$

Again the velocity derivative terms are evaluated in (ξ,η) space via the chain rule, as mentioned in Section A.1.3, but remain unexpanded in the source term components above for brevity.

A.3 Spatial Discretisation for Mean Flow Equations

The Navier-Stokes equations are discretised using a cell-centred finite volume approach. The computational domain is divided into a finite number of non-overlapping control-volumes, and the governing equations are applied to each cell in turn. Also, the Navier-Stokes equations are re-written in a curvilinear coordinate system which simplifies the formulation of the discretised terms since body-conforming grids are adopted here. The spatial discretisation of equation (A.11) leads to a set of ordinary differential equations in time:

$$\frac{d\mathbf{W}_{i,j}}{dt} = -\mathbf{R}_{i,j} \tag{A.20}$$

where $\mathbf{W}$ and $\mathbf{R}$ are the vectors of cell conserved variables and residuals respectively. The convective terms are discretised in the present work using Osher's upwind scheme [84] for its robustness, accuracy and stability properties. In addition, a MUSCL interpolation [85] is used to provide third-order accuracy and the Anderson [86] or van Albada limiter [87] prevents spurious oscillations from occurring around shock waves. The discretisation of the viscous terms requires the value of the velocity components and their derivatives, as well as the derivatives of the static temperature, at the edges of each cell. Cell-edge values of the velocity components are approximated by the average of the two adjacent cell-centre values, as shown below:

$$u_{i+\frac{1}{2},j} = \frac{1}{2}\left(u_{i,j} + u_{i+1,j}\right) \tag{A.21}$$

Cell-edge values of the derivatives are obtained using Green's formula applied to an auxiliary cell surrounding the considered edge, for example:

$$\begin{aligned} \frac{\partial u}{\partial x} &= \frac{1}{h_{aux}} \oint_{\Omega_{s_{aux}}} u dy \\ \frac{\partial u}{\partial y} &= \frac{-1}{h_{aux}} \oint_{\Omega_{s_{aux}}} u dx \end{aligned} \tag{A.22}$$

where h_{aux} is the area of the auxiliary cell. The values at the four points a, b, c, d are obtained using the neighbouring cell-centre values:

$$\begin{aligned} u_a &= u_{i,j} \\ u_b &= \frac{u_{i,j-1} + u_{i,j} + u_{i+1,j-1} + u_{i+1,j}}{4} \\ u_c &= u_{i+1,j} \\ u_d &= \frac{u_{i,j} + u_{i,j+1} + u_{i+1,j} + u_{i+1,j+1}}{4} \end{aligned} \tag{A.23}$$

The choice of the auxiliary cell is guided by the need to avoid odd-even point decoupling and to minimise the amount of numerical viscosity introduced in the discretised equations.

The boundary conditions are set by using two rows of halo cells. Values are set in the halo according to interior values and boundary values. Once halo values are set then all interior cells are treated in an identical fashion. The extrapolations used are shown in table A.1. The subscript 1 denotes values in the interior cell adjacent to the boundary, 2 the next interior cell, b1 the first halo cell and b2

Boundary Type	First Halo Cell	Second Halo Cell
Far Field	$\rho_{b1} = 1.0$	$\rho_{b2} = \rho_{b1}$
	$u_{b1} = u_\infty$	$u_{b2} = u_{b1}$
	$v_{b1} = v_\infty$	$v_{b2} = v_{b1}$
	$p_{b1} = p_\infty$	$p_{b2} = p_{b1}$
Wall	$\rho_{b1} = \rho_1$	$\rho_{b2} = \rho_{b1}$
(viscous	$u_{b1} = 2u_w - u_1$	$u_{b2} = 2u_w - u_2$
adiabatic)	$v_{b1} = 2v_w - v_1$	$v_{b2} = 2v_w - v_2$
	$p_{b1} = p_1$	$p_{b2} = p_{b1}$
0th extrapolation	$\rho_{b1} = \rho_1$	$\rho_{b2} = \rho_1$
	$u_{b1} = u_1$	$u_{b2} = u_1$
	$v_{b1} = v_1$	$v_{b2} = v_1$
	$p_{b1} = p_1$	$p_{b2} = p_1$
1st extrapolation	$\rho_{b1} = \rho_e$	$\rho_{b2} = 2\rho_{b1} - \rho_1$
	$u_{b1} = u_e$	$u_{b2} = 2u_{b1} - u_1$
	$v_{b1} = v_e$	$v_{b2} = 2v_{b1} - v_1$
	$p_{b1} = p_e$	$p_{b2} = 2p_{b1} - p_1$

Table A.1: Boundary conditions for the mean flow equations

the second halo cell and file denotes values read from a file. ϕ_e denotes the value $\phi_e = 2\phi_1 - \phi_2$, $u_t = n_y(1.5u_1 - u_2) - n_x(1.5v_1 - v_2)$ where n_x and n_y are the boundary normal components, u_w,v_w and t_w are the boundary velocity components and temperature, $val = 1.0 - 0.5(\gamma - 1)u_1^2$ and $s = \gamma M_\infty^2$. Values ϕ_{vc} are calculated using the compressible vortex correction of [88].

A.4 Spatial Discretisation for Turbulent Flow Equations

The semi-discrete form of the $k - \omega$ turbulence model is given by

$$\frac{d\mathbf{q}_{i,j}}{dt} = -\mathbf{Q}_{i,j}. \tag{A.24}$$

Boundary Type	First Halo Cell	Second Halo Cell
Far Field	$k_{b1} = k_\infty$	$k_{b1} = k_\infty$
	$\omega_{b1} = \omega_\infty$	$\omega_{b2} = \omega_{b1}$
Wall	$k_{b1} = -k_1$	$k_{b2} = -k_2$
	$\omega_{b1} = 2\omega_w - \omega_1$	$\omega_{b2} = 2\omega_w - \omega_2$
0th extrapolation	$k_{b1} = k_1$	$k_{b1} = k_{b1}$
	$\omega_{b1} = \omega_1$	$\omega_{b2} = \omega_{b1}$
1st extrapolation	$k_{b1} = k_1$	$k_{b2} = k_{b1} - k_1$
	$\omega_{b1} = \omega_1$	$\omega_{b2} = 2\omega_{b1} - \omega_1$
symmetry	$k_{b1} = k_1$	$k_{b2} = k_2$
	$\omega_{b1} = \omega_1$	$\omega_{b2} = \omega_2$

Table A.2: Boundary conditions for the turbulent flow equations

Here $\mathbf{Q}_{i,j}$ denotes the discretisation of the spatial and source terms. The convective terms are discretised by the Engquist-Osher method [89], considering the k and ω equations as decoupled scalar equations with a prescribed velocity field. The spatial discretisation is either first or third order accurate using MUSCL interpolation and the limiters as described for the mean flow equations. The viscous diffusion terms are discretised in an identical fashion to those in the mean flow equations. The source term is evaluated at the cell centre, using the approach described above for the evaluation of derivatives in equation (A.22).

The turbulent boundary conditions are implemented as for the mean flow values. The halo values are given in table A.2 where

$$\omega_w = \frac{60\mu_{wall}}{\beta_1 * \rho_w * Re * d^2} \tag{A.25}$$

where d is the normal distance from the wall interface centre to the centre of the first interior cell.

A.5 Steady State Solver for Inviscid and Laminar Cases

The integration in time of equation (A.20) to a steady-state solution is performed using an implicit time-marching scheme:

$$\frac{\mathbf{W}^{n+1} - \mathbf{W}^n}{\Delta t} = -\mathbf{R}^{n+1} \tag{A.26}$$

where subscripts (i, j) are neglected for clarity. The above equation represents a system of non-linear algebraic equations and to simplify the solution procedure, the flux residual $\mathbf{R}^{n+1}$ is linearised in time as follows:

$$\begin{aligned} \mathbf{R}^{n+1} &= \mathbf{R}^n + \frac{\partial \mathbf{R}}{\partial t}\Delta t + O(\Delta t^2) \\ &\approx \mathbf{R}^n + \frac{\partial \mathbf{R}}{\partial \mathbf{W}}\frac{\partial \mathbf{W}}{\partial t}\Delta t \\ &\approx \mathbf{R}^n + \frac{\partial \mathbf{R}}{\partial \mathbf{W}}\Delta W \end{aligned} \tag{A.27}$$

where $\Delta \mathbf{W} = \mathbf{W}^{n+1} - \mathbf{W}^n$. Equation (A.26) now becomes the following linear system:

$$\left(\frac{I}{\Delta t} + \frac{\partial \mathbf{R}}{\partial \mathbf{W}}\right)\Delta \mathbf{W} = -\mathbf{R}^n \tag{A.28}$$

The complexity of a direct method to compute a linear system is of the order of $\mathcal{N}^3$, which becomes prohibitive when the total number of equations $\mathcal{N}$ becomes large. On the other hand, iterative techniques such as Conjugate Gradient (CG) methods are capable of solving large systems of equations more efficiently in terms of time and memory. CG methods find an approximation to the solution of a linear system by minimising a suitable residual error function in a finite-dimensional space of potential solution vectors. Several algorithms, such as BiCG, CGSTAB, CGS and GMRES, have been tested in [90] and it was concluded that the choice of method is not as crucial as the preconditioning. The current results use a Generalised Conjugate Gradient method [91].

The preconditioning strategy is based on a Block Incomplete Lower-Upper factorisation [91] since it appears to be the most promising. The sparsity pattern of the Lower and Upper matrices is defined with respect to the sparsity of the unfactored matrix for simplicity.

Implicit schemes require particular treatment during the early stages of the iterative procedure. The usual approach in starting the method is to take a small CFL number and to increase it later on. However, it was found that smoothing out the initial flow doing some explicit iterations, and then switching to the implicit algorithm was equally efficient. In the present method, a specified number of forward Euler iterations are executed before switching to the implicit scheme.

The inviscid fluxes are calculated using an upwind scheme. Hence, the numerical flux across an edge depends on the values of the flow variables on either side of the edge. For example, for the interface between cell (i, j) and cell $(i+1, j)$:

$$\mathbf{F}_{i+\frac{1}{2},j} = \mathbf{F}\left(\mathbf{W}^{+}_{i+\frac{1}{2},j}, \mathbf{W}^{-}_{i+\frac{1}{2},j}\right) \tag{A.29}$$

where the left and right states are extrapolated using a MUSCL interpolation, leading to the following relations:

$$\begin{aligned} \mathbf{W}^{-}_{i+\frac{1}{2},j} &= \mathcal{F}\left(\mathbf{W}_{i-1,j}, \mathbf{W}_{i,j}, \mathbf{W}_{i-1,j}, \mathbf{W}_{i+2,j}\right) \\ \mathbf{W}^{+}_{i+\frac{1}{2},j} &= \mathcal{G}\left(\mathbf{W}_{i-1,j}, \mathbf{W}_{i,j}, \mathbf{W}_{i+1,j}, \mathbf{W}_{i+2,j}\right) \end{aligned} \tag{A.30}$$

As a result, the flux residual for cell (i, j) is a function of nine points:

$$\mathbf{R}_{i,j} = \mathbf{R}\left(\mathbf{W}_{i-2,j}, \mathbf{W}_{i-1,j}, \mathbf{W}_{i,j}, \mathbf{W}_{i+1,j}, \mathbf{W}_{i+2,j}, \mathbf{W}_{i,j-2}, \mathbf{W}_{i,j-1}, \mathbf{W}_{i,j+1}, \mathbf{W}_{i,j+2}\right)$$

The above formulation for $\mathbf{R}_{i,j}$ leads to a Jacobian matrix $\partial\mathbf{R}/\partial\mathbf{W}$ which has nine non-zero entries per row. However, trying to reduce the number of non-zero blocks would have several advantages. Firstly, the memory requirements are lowered. Secondly, the resolution of the linear system by the CG method is faster in terms of CPU-time since all the matrix-vector multiplications involved require less operation counts. Finally, the linear system is easier to solve since the approximate Jacobian matrix is more diagonally dominant. A full discussion of the approximate Jacobian formulation is given in [92].

An approximation to the exact Jacobian arises from neglecting the influence of the MUSCL interpolation:

$$\begin{aligned} \mathbf{W}^{-}_{i+\frac{1}{2},j} &= \mathcal{F}'\left(\mathbf{W}_{i,j}\right) \\ \mathbf{W}^{+}_{i+\frac{1}{2},j} &= \mathcal{G}'\left(\mathbf{W}_{i+1,j}\right) \end{aligned} \tag{A.31}$$

The flux residual now becomes a function of only five points:

$$\mathbf{R}_{i,j} = \mathbf{R}'\left(\mathbf{W}_{i-1,j}, \mathbf{W}_{i,j}, \mathbf{W}_{i+1,j}, \mathbf{W}_{i,j-1}, \mathbf{W}_{i,j+1}\right) \tag{A.32}$$

This approximation, which is applied only for the derivation of the Jacobian terms, reduces memory requirements and matrix-vector multiplication operation counts to 5/9 of the values using the exact Jacobians.

The discretisation of the viscous terms leads to a viscous flux residual which is a function of the following nine points: $\mathbf{W}_{i-1,j-1}$, $\mathbf{W}_{i,j-1}$, $\mathbf{W}_{i+1,j-1}$, $\mathbf{W}_{i-1,j}$, $\mathbf{W}_{i,j}$, $\mathbf{W}_{i+1,j}$, $\mathbf{W}_{i-1,j+1}$, $\mathbf{W}_{i,j+1}$ and $\mathbf{W}_{i+1,j+1}$. An exact derivation of the inviscid and viscous Jacobians together would involve four more terms in addition to the nine above: $\mathbf{W}_{i-2,j}$, $\mathbf{W}_{i+2,j}$, $\mathbf{W}_{i,j-2}$ and $\mathbf{W}_{i,j+2}$.

However, in view of the computational results presented in the previous section, it seems more interesting from a storage and CPU-time point of view to derive an approximate formulation for the viscous Jacobians based on equation (A.32). Indeed, such an approach would give savings of 8/13 for the memory requirements and any matrix-vector multiplication operation counts. A simple approximation results from taking into account only the influence of the two points situated either side of the considered edge during the calculation of the viscous flux across a cell interface. For example, the contributions of $\mathbf{W}_{i,j-1}$, $\mathbf{W}_{i,j+1}$, $\mathbf{W}_{i+1,j-1}$ and $\mathbf{W}_{i+1,j+1}$ are neglected and only the terms arising from $\mathbf{W}_{i,j}$ and $\mathbf{W}_{i+1,j}$ are kept. This amounts to making a thin layer approximation for the derivation of the viscous Jacobians in the direction normal to the edge.

A.6 Steady State Solver for Turbulent Case

The integration in time of equation (A.24) to a steady-state solution is performed using an implicit time-marching scheme:

$$\frac{\mathbf{q}^{n+1} - \mathbf{q}^n}{\Delta t} = -\mathbf{Q}^{n+1}. \tag{A.33}$$

This nonlinear system of equations is formulated and solved in an identical manner to that described above for the mean flow. Equations (A.26) and (A.33) are solved in sequence, i.e. the eddy-viscosity is regarded calculated from the latest values of

k and ω and is used to advance the mean flow solution and then this new solution is used to update the turbulence solution, freezing the mean flow values.

An approximate Jacobian is used for the source term by only taking into account the contribution of the dissipation terms $\hat{\mathbf{D}}_k$ and $\hat{\mathbf{D}}_\omega$ i.e. no account of the production terms is taken on the left hand side of (A.33). This approach has a stability advantage as described in [83].

A.7 Unsteady Flow Solver

The formulation is described for the turbulent case. The laminar and inviscid cases represent a simplification of this.

Following the pseudo-time formulation [93], the updated mean flow solution is calculated by solving the steady state problems

$$\mathbf{R}^*_{i,j} = \frac{3\mathbf{w}^{n+1}_{i,j} - 4\mathbf{w}^{n}_{i,j} + \mathbf{w}^{n-1}_{i,j}}{2\Delta t} + \mathbf{R}_{i,j}(\tilde{\mathbf{w}}^{k_m}_{i,j}, \tilde{\mathbf{q}}^{k_t}_{i,j}) = 0 \tag{A.34}$$

$$\mathbf{Q}^*_{i,j} = \frac{3\mathbf{q}^{n+1}_{i,j} - 4\mathbf{q}^{n}_{i,j} + \mathbf{q}^{n-1}_{i,j}}{2\Delta t} + \mathbf{Q}_{i,j}(\tilde{\mathbf{w}}^{l_m}_{i,j}, \tilde{\mathbf{q}}^{l_t}_{i,j}) = 0. \tag{A.35}$$

Here k_m, k_t, l_m and l_t give the time level of the variables used in the spatial discretisation. Note that for the problems of this paper the grid is moved rigidly but if grid deformation was required then time varying areas would be required [94] in the expression for the real time derivative in equations (A.34) and (A.35). If $k_m = k_t = l_m = l_t = n + 1$ then the mean and turbulent quantities are advanced in real time in a fully coupled manner. However, if $k_m = l_m = l_t = n + 1$ and $k_t = n$ then the equations are advanced in sequence in real time, i.e. the mean flow is updated using frozen turbulence values and then the turbulent values are updated using the latest mean flow solution. This has the advantage that the only modification, when compared with the laminar case, to the discretisation of the mean flow equations is the addition of the eddy viscosity from the previous time step. The turbulence model only influences the mean flow solution through the eddy viscosity and so any two equation model can be used without modifying the mean flow solver. Hence, the implementation is simplified by using a sequenced solution in real time. However, the uncoupling could adversely effect the stability and accuracy of the real

time stepping, with the likely consequence of limiting the size of the real time step that can be used.

Equations (A.34) and (A.35) represent a coupled nonlinear system of equations. These can be solved by introducing an iteration through *pseudo time* τ to the steady state, as given by

$$\frac{\mathbf{w}_{i,j}^{n+1,m+1} - \mathbf{w}_{i,j}^{n+1,m}}{\Delta\tau} + \frac{3\mathbf{w}_{i,j}^{k_m} - 4\mathbf{w}_{i,j}^{n} + \mathbf{w}_{i,j}^{n-1}}{2\Delta t} + \mathbf{R}_{i,j}(\tilde{\mathbf{w}}_{i,j}^{k_m}, \tilde{\mathbf{q}}_{i,j}^{k_t}) = 0 \qquad \text{(A.36)}$$

$$\frac{\mathbf{q}_{i,j}^{n+1,m+1} - \mathbf{q}_{i,j}^{n+1,m}}{\Delta\tau} + \frac{3\mathbf{q}_{i,j}^{l_t} - 4\mathbf{q}_{i,j}^{n} + \mathbf{q}_{i,j}^{n-1}}{2\Delta t} + \mathbf{Q}_{i,j}(\tilde{\mathbf{w}}_{i,j}^{l_m}, \tilde{\mathbf{q}}_{i,j}^{l_t}) = 0. \qquad \text{(A.37)}$$

where the $m-th$ pseudo-time iterate at the $n+1th$ real time step are denoted by $\mathbf{w}^{n+1,m}$ and $\mathbf{q}^{n+1,m}$ respectively. The iteration scheme used only effects the efficiency of the method and hence we can sequence the solution in pseudo time without compromising accuracy. Examples of For example, using explicit time stepping we can calculate $\mathbf{w}^{n+1,m+1}$ using $k_m = n+1, m$ and $k_t = n+1, m$ and $\mathbf{q}^{n+1,m+1}$ using $l_m = n+1, m+1$ and $l_t = n+1, m$. For implicit time stepping in pseudo time we can use $k_m = l_m = l_t = n+1, m+1$ and $k_t = n+1, m$. In both of these cases the solution of the equations is decoupled by freezing values but at convergence the real time stepping procedes with no sequencing error. It is easy to recover a solution which is sequenced in real time from this formulation by setting $k_t = n$ throughout the calculation of the pseudo steady state. This facilitates a comparison of the current pseudo time sequencing with the more common real time sequencing. In the code the pseudo steady-state problems are solved using the implicit steady state solver described above.

A.8 Mesh Treatment

There are two mesh movement methods available in the code. The simplest involves rigid mesh rotation and translation in the y-direction. The second involves a more flexible regeneration method by transfinite interpolation of displacements. The mesh velocities and boundary velocities are calculated from the difference formula

$$\frac{dx}{dt} \approx \frac{3\mathbf{x}_{i,j}^{n+1} - 4\mathbf{x}_{i,j}^{n} + \mathbf{x}_{i,j}^{n-1}}{2\Delta t}. \qquad \text{(A.38)}$$

The cell areas are either calculated algebraically from the vertex locations using a cross product or are obtained from the Global Conservation Law.

When computing the flow on a moving grid, the cell areas vary in time and it is therefore important to discretise the time-dependent metrics carefully in order to maintain the conservative properties of the scheme. If the cell areas are calculated analytically in terms of the grid node positions, numerical errors will be introduced in the calculated solution which increase with time. To avoid such numerical errors, the cell areas must be integrated forward in time by using the same method as used to solve the flow conservation laws [95]. This is achieved by introducing a Geometric Conservation Law (GCL) which can be derived from the continuity conservation law written in integral form by assuming a uniform flow field. This yields,

$$\frac{\partial}{\partial t}\int_{\Omega} dV - \oint_{\partial\Sigma} \mathbf{v}\cdot\mathbf{n}d\Sigma = 0 \tag{A.39}$$

where V is the cell area, $\mathbf{v}$ is the grid speed, $\mathbf{n}$ is the normal area vector and $\partial\Sigma$ is the boundary surface of the control volume Ω. Using the same second-order time discretisation as for the flow equations [94], equation (A.39) becomes

$$\frac{3V_{i,j}^{n+1} - 4V_{i,j}^{n} + V_{i,j}^{n-1}}{2\Delta t} - \oint_{\partial\Sigma} \mathbf{v}\cdot\mathbf{n}d\Sigma = 0 \tag{A.40}$$

This law states that the change in area of each control volume between t^n and t^{n+1} must be equal to the area swept by the cell boundary during $\Delta t = t^{n+1} - t^n$. The volume $V_{i,j}^{n+1}$ at the new time step can then be computed by

$$V_{i,j}^{n+1} = \frac{4V_{i,j}^{n}}{3} - \frac{V_{i,j}^{n-1}}{3} + \frac{2\Delta t}{3}\oint_{\partial\Sigma} \mathbf{v}\cdot\mathbf{n}d\Sigma \tag{A.41}$$

where

$$\oint_{\partial\Sigma} \mathbf{v}\cdot\mathbf{n}d\Sigma = (\xi_t)_{i+1/2,j} - (\xi_t)_{i-1/2,j} + (\eta_t)_{i,j+1/2} - (\eta_t)_{i,j-1/2}$$

and

$$\xi_t = -(\xi_x x_t + \xi_y y_t), \qquad \eta_t = -(\eta_x x_t + \eta_y y_t)$$

Note that this is an explicit equation for $V_{i,j}^{n+1}$ since the terms ξ_t and η_t are prescribed from the node values. Using the GCL to calculate the volumes numerically

rather than analytically yields a self-consistent solution for the effective volume elements. In other words, it ensures that errors arising from the computation of the geometric quantities are consistent with those arising from the integration of the flow equations. The importance of the GCL for flow computations on moving grids has been described in [95] [96] [97] [98] [99]. The GCL needs to be evaluated once at every global time step to calculate the new cell areas.

The mesh regeneration is achieved through the transfinite interpolation (TFI) of displacements within the multiblock method.

We first need to determine the displacements of the four block corners (or block vertices). In order to identify a moving block from a fixed block, we introduce a new parameter MOVE in the grid file which is set to one for each moving block and to zero for all fixed blocks. For each block corner, a search is made over its neighbours, and if at least one of the neighbouring blocks surrounding this corner point (i.e., all blocks having this point as a vertex) is fixed (i.e., block flagged with MOVE=0), then no displacement is allowed for this point. Otherwise, the corner point is moved according to the motion of the solid surface. The displacement of all points lying on a moving surface is assumed to be known. In the present work, we consider only rigid motions for oscillating pitching aerofoils and oscillating flaps, but the application of the method can be easily extended to more complex configurations and more general deformations.

The displacements of the four corner points are then used to interpolate the displacement of all the points along the block boundary. We denote by bfx and $dbfx$ the position vector and displacement vector respectively associated with the grid points of the mesh,

$$bfx = \begin{bmatrix} x(\xi,\eta) \\ y(\xi,\eta) \end{bmatrix}, dbfx = \begin{bmatrix} dx(\xi,\eta) \\ dy(\xi,\eta) \end{bmatrix}$$

Let A and B be the two end-points of a block face with respective displacements denoted by $dbfx_A$and $dbfx_B$ respectively. The displacement $dbfx$ of any point P along this boundary can then be obtained by the weighted formula

$$dbfx = \left(1 - \frac{a}{c}\right) dbfx_A + \left(1 - \frac{b}{c}\right) dbfx_B$$

where $a = ||\vec{AP}||$, $b = ||\vec{BP}||$ and $c = ||\vec{AB}||$. Here, the distances are calculated

from the previous grid point coordinates. If both end-points are fixed (i.e., zero displacement), then the whole block face remains fixed.

Following the original formulation of the TFI algorithm described by Gordon and Hall [100], the general transfinite interpolation method results in a recursive algorithm which is here applied to the grid point displacements :

$$\begin{aligned} dbfx(\xi,\eta) = bff_1(\xi,\eta) &+ \phi_1^0(\eta)\left[dbfx_{b1}(\xi) - bff_1(\xi,0)\right] \\ &+ \phi_2^0(\eta)\left[dbfx_{b3}(\xi) - bff_1(\xi,1)\right] \end{aligned}$$

where

$$bff_1(\xi,\eta) = \psi_1^0(\xi)dbfx_{b4}(\eta) + \psi_2^0(\xi)dbfx_{b2}(\eta)$$

and $dbfx_{b1}$,$dbfx_{b2}$,$dbfx_{b3}$,and $dbfx_{b4}$ are the interpolated displacements along the four block faces. The functions ψ and ϕ are the blending functions in the ξ and η directions respectively. These functions are given by the grid point distributions along each block face as

$$\begin{aligned} \psi_1^0(\xi) &= 1 - s_1(\xi) \\ \psi_2^0(\xi) &= s_3(\xi) \\ \phi_1^0(\eta) &= 1 - s_4(\eta) \\ \phi_2^0(\eta) &= s_2(\eta) \end{aligned}$$

where $s_1(\xi)$ is the stretching function on the block face $\eta = 0$, $s_2(\eta)$ on the block face $\xi = 1$, $s_3(\xi)$ on the block face $\eta = 1$, $s_4(\eta)$ on the block face $\xi = 0$.

The coordinates of the new grid points are then simply obtained by

$$bfx(\xi,\eta) = bfx_0(\xi,\eta) + dbfx(\xi,\eta)$$

where $dbfx$ is the interpolated displacement and bfx_0 is the vector position for the initial undisturbed grid.

Bibliography

[1] J. Seddon. *Basic Helicopter Aerodynamics*. BSP Professional Books, 1990.

[2] W.J. McCroskey. Unsteady Airfoils. *Annual Review of Fluid Mechanics*, 14:285–311, 1982.

[3] Jaan Liiva. Unsteady Aerodynamic and Stall Effects on Helicopter Rotor Blade Airfoil Sections. *Journal of Aircraft*, 6(1), 1969.

[4] Norman D. Ham and Melvin S. Garelick. Dynamic Stall Considerations in Helicopter Rotors. *Journal of the American Helicopter Society*, 13(2), 1968.

[5] J.G. Leishman. Dynamic Stall Experiments on the NACA 23012 Aerofoil. *Experiments in Fluids*, 9:49–58, 1990.

[6] G. Alvin Pierce, Donald L. Lunz, and John B. Malone. The Effect of Varying Freestream Velocity on Airfoil Dynamic Stall Characteristics. *Journal of The American Helicopter Society*, 23(2):27–33, April 1978.

[7] M. Raffel, J. Kompenhans, and P. Wernert. Investigation of the Unsteady Flow Velocity Field above an Airfoil Pitching under Deep Dynamic Stall Conditions. *Experiments in Fluids*, 19:103–111, 1995.

[8] L.W. Carr and M.S. Chandrasekhara. An Assessment of the Impact of Compressibility on Dynamic Stall. *AIAA paper 95-0779*, 1995.

[9] R.D. Van Dyken, J.A Ekaterinaris, M.S. Chandrasekhara, and M.F. Platzer. Analysis of Compressible Light Dynamic Stall Flow at Transitional Reynolds Numbers. *AIAA Journal*, 34(7), July 1996.

[10] William G. Bousman. A Qualitative Examination of Dynamic Stall from Flight Test Data. *Journal of The American Helicopter Society*, October 1998.

[11] W.J. McCroskey. Recent Developments in Rotor Blade Stall. *Symposium on Unsteady Aerodynamics Tucson,*, Tucson, Arizona, March 1975.

[12] Wayne Johnson. The Effect of Dynamic Stall on the Response and Airloading of Helicopter Rotor Blades. *Journal of The American Helicopter Society*, 14, April 1969.

[13] Norman D. Ham. Aerodynamic Loading on a Two-Dimensional Airfoil during Dynamic Stall. *AIAA Journal*, 6(10), October 1968.

[14] Santu T. Gangwani. Prediction of Dynamic Stall and Unsteady Airloads for Rotor Blades. *Journal of The American Helicopter Society*, October 1982.

[15] J.G. Leishman and T.S. Beddoes. A Semi-Empirical Model for Dynamic Stall. *Journal of The American Helicopter Society*, pages 3–17, July 1989.

[16] J.G. Leishman. Modelling Sweep Effects on Dynamic Stall. *Journal of The American Helicopter Society*, July 1989.

[17] T.S. Beddoes. Prediction(s) Methods for Unsteady Flows. *AGARD report No. 679, Special Course on Unsteady Aerodynamics*, March 1980.

[18] Ismail H. Tuncer, James C. Wu, and C.M. Wang. Theoretical and Numerical Studies of Oscillating Airfoils. *AIAA Journal*, 28(9), September 1990.

[19] J.C. Balleur and P. Girodroux-Lavigne. Calculation of Dynamic Stall by Viscous-Inviscid Interaction over Airfoils and Helicopter-Blade Sections. *51st Annual Forum of the American Helicopter Society*, May 1995.

[20] K.N. Ghia, J. Yang, U. Ghia, and G.A. Osswald. Analysis and Control of Dynamic Stall Phenomenon using Navier-Stokes Formulation involving Vorticity, Stream Function and Circulation. *Sādhanā*, 18(parts 3and 4), August 1993.

[21] J.A. Ekaterinaris, N.N. Sorensen, and F. Rasmussen. Numerical Investigation of Airfoil Dynamic Stall in Simultaneous Harmonic Oscillatory and Translatory Motion. *Journal of Solar Energy Engineering*, 120, February 1998.

[22] E. Guilmineau, J. Piquet, and P. Queutey. Unsteady Two-Dimensional Turbulent Viscous Flow Past Aerofoils. *International Journal for Numerical Methods in Fluids*, 25, 1997.

[23] Norman D. Ham. An Experimental Investigation of Stall Flutter. *29th Annual Meeting of the I.A.S.*, January 1961.

[24] Norman D. Ham. Stall Flutter of Helicopter Rotor Blades: A Special Case of the Dynamic Stall Phenomenon. *23rd Annual Forum of the American Helicopter Society, Wahington, D.C.*, May 1967.

[25] Franklin O. Carta. An Analysis of the Stall Flutter Instability of Helicopter Rotor Blades. *Journal of the American Helicopter Society*, 12(4), 1967.

[26] F.J. Tarzanin Jr. Prediction of Control Loads due to Blade Stall. *Journal of the American Helicopter Society*, 17(2), 1972.

[27] P.G. Wilby. Shockwaves in the Rotor World - A Personal Perspective of 30 years of Rotor Aerodynamic Developments in the UK. *The Aeronautical Journal*, March 1998.

[28] Khanh Nguyen and Inderjit Chopra. Application of Higher Harmonic Control to Rotors Operating at High Speed and Thrust. *Journal of the American Helicopter Society*, July 1990.

[29] Khanh Nguyen. Active Control of Helicopter Blade Stall. *Journal of Aircraft*, 35(1), January–February 1998.

[30] Yung H. Yu, Bernd Gmelin, Wolf Splettstoesser, Jean Philippe, Jean Prieur, and Thomas F.Brooks. Reduction of Helicopter Blade-Vortex Interaction Noise by Active Rotor Control Technology. *Progress in Aerospace Science*, 33, 1997.

[31] M.S. Chandrasekhara, M.C. Wilder, and L.W. Carr. Unsteady Stall Control using Dynamically Deforming Airfoils. *AIAA Journal*, 36(10):1792 1800, 1998.

[32] M.S. Chandrasekhara, M.C. Wilder, and L.W. Carr. Compressible Dynamic Stall Control: Comparison of Two Approaches. *Journal of Aircraft*, 38(3), May–June 2001.

[33] Yung H. Yu, Soogab Lee, Kenneth W. McAlister, Chee Tung, and Clin M. Wang. Dynamic Stall Control for Advanced Rotorcraft Application. *AIAA Journal*, 33(2), February 1995.

[34] I. A. Cheeseman and A.R. Seed. The Application of Circulation Control by Blowing to Helicopter Rotors. *Journal of The Royal Aeronautical Society*, July 1967.

[35] I.M. Davidson. The jet flap. *Journal of the Royal Aeronautical Society*, 60, 1956.

[36] N.J. Wood and Jack N. Nielsen. Circulation Control Airfoils as Applied to Rotary-Wing Aircraft. *Journal of Aircraft*, December 1986.

[37] V. Raghavan, Inderjit Chopra, and Shih-I Pai. Circulation Control Airfoils in an Unsteady Flow. *Journal of the American Helicopter Society*, October 1988.

[38] Terence A. Ghee and J.Gordon Leishman. Effects of Unsteady Blowing on the Lift of a Circulation Controlled Cylinder. *Journal of the American Helicopter Society*, pages 90–93, July 1990.

[39] Peter F. Lorber, Franklin O. Carta, and Raymond G. Carlson. The Aerodynamics of an Oscillating Jet Flap. *Journal of the American Helicopter Society*, pages 24–32, April 1989.

[40] A. Seifert, T. Bachar, D.Koss, M. Shepshelovich, and I. Wygnanski. Oscillatory Blowing: A Tool to Delay Boundary Layer Separation. *AIAA Journal*, 31(11), November 1993.

[41] B. Nishri and I. Wygnanski. Effects of Periodic Excitation on Turbulent Flow Separation from a Flap. *AIAA Journal*, 36(4), April 1998.

[42] A. Seifert and L.G. Pack. Oscillatory Control of Separation at High Reynolds Numbers. *AIAA Journal*, 37(9), September 1999.

[43] D. Greenblatt and I. Wygnanski. Dynamic Stall Control by Periodic Excitation, Part 1: NACA 0015 Parametric Study. *Journal of Aircraft*, 38(3), May–June 2001.

[44] D. Greenblatt, B. Nishri, A. Darabi, and I. Wygnanski. Dynamic Stall Control by Periodic Excitation, Part 2: Mechanisms. *Journal of Aircraft*, 38(3), May–June 2001.

[45] R.C. Chang, F.-B. Hsiao, and R.-N. Shyu. Forcing level effects of internal acoustic excitation on the improvement of airfoil performance. *Journal of Aircraft*, 29(5):823–829, September–October 1992.

[46] Ming Xiao, Dai Changhui, and Shi Shengxi. A new phenomenon of acoustic streaming. *Acta Mechanica Sinica*, 7(3):193–198, August 1991.

[47] Stuart A. Jacobson and William C. Reynolds. Active Control of Streamwise Vortices and Streaks in Boundary Layers. *Journal of Fluid Mechanics*, 360, 1998.

[48] Ruben Rathnasingham and Kenneth S. Breuer. System Identification and Active Control of a Turbulent Boundary Layer. *AIAA paper 97-1793*, 1997.

[49] Ruben Rathnasingham and Kenneth S. Breuer. Coupled Fluid Structural Characteristics of Actuators for Flow Control. *AIAA Journal*, 35(5), May 1997.

[50] Jason T. Lachowicz, Chung-Sheng Yao, and Richard W. Wlezien. Scaling of an oscillatory flow control actuator. *AIAA Paper 98-0330*, 1998.

[51] Ahmed A. Hassan. Numerical Simulations and Potential Applications of Zero-Mass Jets for Enhanced Rotorcraft Performance. *AIAA Paper 98-0211*, 1998.

[52] John F. Donovan, Linda D. Kral, and Andrew W. Cary. Active Flow Control Applied to an Airfoil. *AIAA Paper 98-0210*, 1998.

[53] Jie-Zhi Wu, Xi-Yun Lu, Andrew G. Denny, Meng Fan, and Jain-Ming Wu. Post-stall flow control on an airfoil by local unsteady forcing. *Journal of Fluid Mechanics*, 371:21–58, 1998.

[54] S.S. Ravindran. Active control of flow separation over an airfoil. *NASA Technical Report, TM-1999-209838*, 1999.

[55] Frederick W. Roos. Synthetic jet microblowing for forebody flow-asymmetry management. *AIAA Paper 98-0212*, 1998.

[56] Michael Amitay, Andrew Honohan, Mark Trautman, and Ari Glezer. Modification of the Aerodynamic Characteristics of Bluff Bodies Using Fluidic Actuators. *AIAA Paper 97-2004*, 1997.

[57] Michael Amitay, Barton L. Smith, and Ari Glezer. Aerodynamic Flow Control Using Synthetic Jet Technology. *AIAA Paper 98-0208*, 1998.

[58] M. Amitay, V.Kibens, D. Parekh, and A. Glezer. The Dynamics of Flow Reattachment over a Thick Airfoil Controlled by Synthetic Jet Actuators. *AIAA Paper 99-1001*, 1999.

[59] O.K. Rediniotis, J. Ko, and X. Yue. Synthetic Jets, their Reduced Order Modelling and Applications to Flow Control. *AIAA Paper 99-1000*, 1999.

[60] A. Crook, A.M. Sadri, and N.J. Wood. The Development and Implementation of Synthetic Jets for the Control of Separated Flow. *AIAA Paper 99-3176*, 1999.

[61] N.J. Wood, A.M. Sadri, and A. Crook. Control of Turbulent Flow Separation by Synthetic Jets. *AIAA Paper 2000-4331*, 2000.

[62] Catalin Nae. Numerical Investigation of the Synthetic Jet Actuator for Flow Control on the Circular Cylinder. *IMACS 2000 World Congress*, 2000.

[63] Barton L. Smith and Ari Glezer. Vectoring and Small-Scale Motions Effected in Free Shear Flows using Synthetic Jet Actuators. *AIAA Paper 97-0213*, January 1997.

[64] Barton L. Smith and Ari Glezer. The Formation and Evolution of Synthetic Jets. *Physics of Fluids*, 10(9), September 1998.

[65] L.D. Kral, J.F. Donovan, A.B. Cain, and A.W. Cary. Numerical Simulation of Synthetic Jet Actuators. *AIAA Paper 97-1824*, 1997.

[66] Donald P. Rizzetta, Miguel R. Visbal, and Michael J. Stanek. Numerical Investigation of Synthetic Jet Flowfields. *AIAA Paper 98-2910*, 1998.

[67] S.G. Mallinson, G. Hong, and J.A. Reizes. Some Characteristics of Synthetic Jets. *AIAA Paper 99-3651*, 1999.

[68] R. Mittal, P. Rampunggoon, and H.S. Udaykumar. Interaction of a Synthetic Jet with a Flat Plate Boundary Layer. *AIAA Paper 2001-2773*, 2001.

[69] Barton L. Smith and Gregory W. Swift. Synthetic jets at large reynolds numbers and comparison to continuous jets. *AIAA Paper 2001-3030*, 2001.

[70] Jose L. Gilarranz, Xue Yue, and Othon K. Rediniotis. PIV Measurements and Modelling of Synthetic Jet Actuators for Flow Control. *Proceedings of FEDSM'98*, ASME Fluids Engineering Summer Meeting (June 21-25), 1998.

[71] David J. Coe, Mark G. Allen, Barton L. Smith, and Ari Glezer. Addressable micromachined jet arrays. *8th International Conference on Solid-State Sensors and Actuators*, Stockholm, Sweden, June 1995.

[72] B.L. Smith, M.A. Trautman, and A. Glezer. Controlled Interactions of Adjacent Synthetic Jets. *AIAA Paper 99-0669*, 1999.

[73] Linda D. Kral and Dahai Guo. Characterization of Jet Actuators for Active Flow Control. *AIAA Paper 99-3573*, 1999.

[74] Steven C. Sauerwein and Ahmad D. Vakili. An Experimental Study of Zero-Mass Jets in Crossflow. *AIAA Paper 99-0668*, 1999.

[75] Michael Amitay, Douglas R. Smith, Valdis Kibens, David E. Parekh, and Ari Glezer. Aerodynamic Flow Control over an Unconventional Airfoil using Synthetic Jet Actuators. *AIAA Journal*, 39(3):361–370, March 2001.

[76] Michael Amitay and Ari Glezer. Role of actuation frequency in controlled flow reattachment over a stalled airfoil. *AIAA Journal*, 40(2):209–216, February 2002.

[77] Douglas R. Smith, Michael Amitay, Valdis Kibens, David Parekh, and Ari Glezer. Modification of Lifting Body Aerodynamics using Synthetic Jets. *AIAA Paper 98-0209*, 1998.

[78] Ahmed A. Hassan. Applications of zero-net-mass jets for enhanced rotorcraft aerodynamic performance. *Journal of Aircraft*, 38(3):478–485, May–June 2001.

[79] K.J. Badcock, B.E. Richards, and M.A Woodgate. Elements of CFD on Block Structured Grids Using Implicit Solvers. *Progress in Aerospace Science*, 36:351–392, 2000.

[80] K.J.Badcock, F.Cantariti, and B.Gribben. Theory guide to pmb2d, version 3.0_1. Technical report, Aerospace Engineering Department, Glasgow University, Glasgow, UK, 1998.

[81] Theodore H. Okiishi Bruce R. Munson, Donald F. Young. *Fundamentals of Fluid Mechanics*. John Wiley and Sons, Inc., 1990.

[82] D.A. Anderson, J.C. Tannehill, and R.H. Pletcher. *Computational Fluid Mechanics and Heat Transfer*. Series in Computational Methods in Mechanics and Thermal Sciences, Hemisphere, New York, 1984, 1984.

[83] D.C.Wilcox. *Turbulence Modelling for CFD*. DCW Industries, Inc., La Cañada, California, 1993.

[84] S.Osher and S.R.Chakravarthy. Upwind schemes and boundary conditions with applications to Euler equations in general coordinates. *Journal Computational Physics*, 50:447–481, 1983.

[85] B.Van Leer. Towards the ultimate conservative difference scheme. V:a second–order sequel to Godunov's method. *J. Comput. Phys.*, 32:101–136, 1979.

[86] W.K. Anderson, J.L. Thomas, and B. Van leer. Comparison of finite volume flux vector splittings for the Euler equations. *AIAA Journal*, 24:1453–1460, 1986.

[87] G.D.Van Albada, B.Van Leer, and W.W. Roberts. A comparative study of computational methods in cosmic gas dynamics. *Astronomy and Astrophysics*, 108, 1982.

[88] J.L.Thomas and M.D.Salas. Far-field boundary conditions for transonic lifting solutions to the Euler equations. *AIAA Journal*, 24:1074–1080, 1986.

[89] B.Enquist and S.Osher. One–sided difference approximations for nonlinear conservation laws. *Math. Comp.*, 36(154):321–351, 1981.

[90] K.J.Badcock, X.Xu, L.Dubuc, and B.E.Richards. Preconditioners for high speed flows in aerospace engineering. In *Numerical Methods for Fluid Dynamics V*, pages 287–294. Institute for Computational Fluid Dynamics, Oxford, 1996.

[91] O.Axelsson. *Iterative Solution Methods.* Cambridge University Press, 1994.

[92] F.Cantariti, L.Dubuc, B.Gribben, M.Woodgate, K.J.Badcock, and B.E.Richards. Approximate Jacobians for the solution of the Euler and Navier-Stokes equations. Aerospace Engineering Report, 5, Glasgow University, Glasgow, UK, 1997.

[93] A.Jameson. Time dependent calculations using multigrid, with applications to unsteady flows past airfoils and wings. Technical report, AIAA 91-1596, 1991.

[94] L.Dubuc, F.Cantariti, M.Woodgate, B.Gribben, K.J.Badcock, and B.E.Richards. Solution of the Euler unsteady equations using deforming grids. to appear in AIAA J, Aerospace Engineering Report 4, Glasgow University, Glasgow, UK, 1997.

[95] P.D.Thomas and C.K.Lombard. Geometric conservation law and its application to flow computations on moving grids. *AIAA J*, 17:1030–1037, 1979.

[96] C.B.Allen. Central-difference and upwind-biased schemes for steady and unsteady Euler acrofoil computations. *Aeronautical Journal*, pages 52–62, 1995.

[97] A.L.Gaitonde. A dual-time method for the solution of the unsteady Euler equations. *Aeronautical Journal*, 10:283–291, 1994.

[98] M.Lesoinne and C.Farhat. Geometric conservation laws for aeroelastic computations using unstructured dynamic meshes. In *12th AIAA CFD conference, San Diego*. AIAA, 1995.

[99] V.Venkatakrishnan and D.J.Mavriplis. Implicit method for the computation of unsteady flows on unstructured grids. In *12th AIAA Computational Fluid Dynamics Conference*. AIAA, 1995.

[100] W.J.Gordon and C.A.Hall. Construction of curvilinear coordinate systems and applications of mesh generation. *Int J Num Meth in Engineering*, 7:461–477, 1973.